TÉCNICO LISBOA

Light Propelled Nanovehicles for Drug Delivery

Ana Marta Amaro Cabral

Thesis to obtain the Master of Science Degree in

Materials Engineering

Supervisor: Prof. Dr. José Paulo Sequeira Farinha

Examination Committee

Chairperson: Prof. Dr. Alberto Eduardo Morão Cabral Ferro

Supervisor: Prof. Dr. José Paulo Sequeira Farinha

Members of Committee: Dr. Pedro Miguel Neves Ribeiro Paulo

November 2022

Declaration

I declare that this document is an original work of my own authorship and that it fulfills all the requirements of the Code of Conduct and Good Practices of the Universidade de Lisboa.

Declaração

Declaro que o presente documento é um trabalho original da minha autoria e que cumpre todos os requisitos do Código de Conduta e Boas Práticas da Universidade de Lisboa.

Acknowledgements

I would like to sincerely thank my supervisor Prof. Dr. José Paulo Sequeira Farinha, for all the dedication in guiding and teaching me along the past months, for all the patience and time placed in me. To Prof. Dr. Carlos Miguel Calisto Baleizão, for having accompanied this work from day one and helping me develop as researcher.

To all my laboratory colleagues, in particular to Pedro Rosa, for helping me with my work and for encouraging me to keep going when things were not going as planned.

To Prof. Ana Clara Marques and Mário Vale for allowing me to use their equipment and helping me in their laboratory.

To my colleagues, Baleia, Catarina and Rita, for these amazing five years. Any of this would have been possible without you. For all the help, patience and kindness, I thank you and I am so proud to call you my friends.

To my best friends, Diogo, Luana, Filipa, Catarina and Bárbara. We have known each other for years, and even though we do not spend as much time together as we did a few years ago, you have always been there for me. For all the wisest advices you gave me, for all the patience, for not letting me give up on anything, for all the fun moments we spend together, thank you.

To all my family. To my grandparents, for believing in me and being as enthusiastic about my work as I am. To my parents, for placing their hope in me and supporting me in every decision I made, even the craziest decisions. You have helped me keeping my focus and my head up, I only reached this far because of you, so thank you.

Abstract

In the recent years, the interest in nanocarriers for controlled and intelligent cargo delivery systems has increased due to the in versatility and tunability, offering extremely promising opportunities within this field. These can already address very well-defined morphology, large cargo capacities, targeting of the destination, and on-demand controlled delivery.

The goal of this project was to add self-propulsion capabilities to these nanovehicles, transforming them in versatile nanorobotic tools. Our proof-of-concept nanovehicles are Janus nanoparticles (JNPs) composed by a silica nanoparticle core and a gold nanostructure in half of their surface. Upon irradiation, the vehicle is propelled in the opposite direction of the gold nanoshell by a photothermal effect.

The project was divided into three parts. First, Janus Nanoparticles are produced by a high yield process based on microparticle templating, specifically via a Pickering emulsion route. The second part consists in studying the optical properties of the Janus nanoparticles, being the most important the plasmon resonance, which can be tuned by varying the gold nanoshell thickness. In the third part we study the motion of the nanovehicle to determine the diffusion regimes upon irradiation.

Our proof-of-concept system exhibited a strong plasmon optical resonance. Upon irradiation with a 632.8 nm laser, it showed the occurrence of two diffusion regimes: translational and rotational. The average directional velocity reached by this system was 3.95 μm/s.

Keywords

Janus nanoparticles, gold nanoparticles, silica nanoparticles, Pickering emulsion, plasmon resonance, self-propulsion.

Resumo

Nos últimos anos, o interesse em nanotransportadores para sistemas de administração de medicamentos controlados e inteligentes aumentou devido à possibilidade de regular a sua morfologia e propriedades. Os nanoveículos oferecem oportunidades extremamente promissoras dentro deste campo. Estes já apresentam uma morfologia bem definida, grandes capacidades de carga, orientação do destino, e entrega controlada.

O objetivo deste projeto é acrescentar capacidades de autopropulsão a estes nanoveículos, transformando-os em ferramentas nanorobóticas versáteis. Os nossos nanoveículos são nanopartículas Janus (JNPs) compostos por um núcleo de nanopartícula de sílica e uma nanoestrutura de ouro em metade da sua superfície. Após irradiação, propulsionam-se em direção oposta à da nanocapa de ouro devido a um efeito fototérmico.

O projeto está dividido em três partes. Primeiro, as nanopartículas Janus são produzidas por um processo de alto rendimento baseado em modelos de micropartículas, especificamente através de uma emulsão de Pickering. A segunda parte consiste no estudo das propriedades óticas das nanopartículas Janus, sendo a mais importante a ressonância plasmónica, que pode ser regulada através da variação da espessura da nanocapa de ouro. Na terceira parte, estudamos o movimento do nanoveículo para determinar os regimes de difusão após irradiação.

O nosso sistema exibiu uma forte ressonância ótica de plasmão. Após irradiação com um laser de 632.8 nm, mostrou a ocorrência de dois regimes de difusão: translacional e rotacional. A velocidade direcional média atingida por este sistema foi de 3.95 μm/s.

Palavras Chave

Nanopartículas Janus, nanopartículas de ouro, nanopartículas de sílica, emulsão de Pickering, ressonância plasmónica, autopropulsão.

Table of Contents

List of Figures

List of Tables

List of Abbreviations

APTES	3-aminopropyl triethoxysilane
AuNPs	Gold nanoparticles
CTAB	Cetyltrimethylammonium bromide
DLS	Dynamic Light Scattering
jSNP	Janus silica nanoparticles
jSNP_f	APTES-modified Janus silica nanoparticles
LSPR	Localized surface plasmon resonance
NIR	Near-infrared
SNPs	Silica nanoparticles
SNP_f	APTES-modified silica nanoparticles
SPR	Surface plasmon resonance
TEM	Transmission Electron Microscopy
UV	Ultraviolet

List of Symbols

E	Desorption energy
θ	Contact angle
R	Particle radius
$\gamma(po)$	Interfacial tension between particle-oil
$\gamma(pw)$	Interfacial tension between particle-water
$\gamma(ow)$	Interfacial tension between oil-water
D	Average droplet diameter
m_p	Mass of solid particles
V_d	Volume of the dispersed face
c_f	Surface coverage
$\Delta\lambda$	Plasmon resonance shift
λ_0	Plasmon resonance wavelength of a solid sphere
t	Gold shell thickness
$g^{(1)}$	Autocorrelation function
τ	Decay time
q	Scattering vector
D_{eff}	Effective diffusion coefficient
τ_R	Rotation relaxation time
ΔL^2	Mean square displacement
v	Average speed

D_0	Stokes-Einstein diffusion coefficient
γ_R	Coefficient for rotational diffusion
D_H	Hydrodynamic diameter
k	Boltzmann's constant
T	Temperature
η	Viscosity

1 Introduction

Nanotechnology is an emerging area that involves the study, synthesis and application of functional materials at the nanoscale.[1] In the last years, a lot of interest arose towards nanotechnology, mainly due to its wide range of applications, from energy storage, water treatment and remediation, to food processing and storage, health monitoring, disease diagnosis and screening, and drug delivery systems.[1]

In 1989, the concept of Janus particles was first introduced by Casagrande et al.[2] However, this concept only gained its importance among the scientific community when, in 1991, Pierre-Gilles de Gennes proposed Janus particles as anisotropic materials during his Nobel Prize Lecture entitled Soft Matter.[3] These particles are named after Janus, an ancient Roman god of gates, who has two faces looking in opposite directions. Hence, Janus particles have two halves exhibiting distinct physical and/or chemical characteristics.[4]

1.1 Janus Particles

The asymmetry of Janus particles at the micro/nanoscale allows the emergence of properties inconceivable for symmetric or homogeneous particles.[5] The Janus structure combining two different nanomaterials make such nanoparticles attractive for target-specific imaging and drug delivery applications.[6] Overall, the anisotropic structure of Janus particles translates into multifunctional properties with versatile modification depending on the chemical composition.[7]

Janus particles with various morphologies (figure 1) have been prepared, ranging from spherical particles to different shapes such as dumbbell-shape, snowman-shape, disk-shape, rod-shape, half-raspberry-shape and mushroom-shape.[5,7] They can further be classified into three main categories: polymeric, inorganic and hybrid polymeric-inorganic Janus particles.[8]

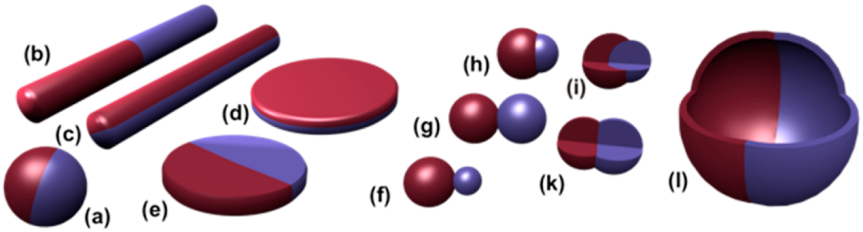

Figure 1. Morphologies of Janus particles: spherical (a), cylindrical (b, c), disc-shaped (d, e), dumbbell-shape with asymmetric or snowman character (f-k), symmetric appearance (g, k), attached nodes (h), eccentric encapsulation (i), and Janus vesicles or capsules (l). Adapted from [5]

Due to the in anisotropic structure, distinct morphologies and compositions, Janus particles can be used in diverse applications, including solid surfactant agents, micro/nanomotors with controlled movement and biomedical applications such as drug delivery, biosensing, bioimaging, cancer therapy and theranostics.[8]

Janus particles can be utilized as solid surfactants to stabilize the oil-water interface of emulsions, due to their amphiphilic properties and to the particle's Pickering effect. Han et al. prepared SiO_2 nanoparticles functionalized with amino and acrylate groups on different sides to be applied in human tooth dentin bonding. First, the amino-modified SiO_2 nanoparticles were used to stabilize a paraffin-in-water Pickering emulsion by arranging at the interface. Then, the exposed amino groups are etched off and the SiO_2 is modified with acrylate groups, forming the final Janus nanoparticles.[9]

Micromotors are generally Janus particles capable of converting energy into movement. For example, Zhou et al. fabricated calcium carbonate particle micromotors with partial gold nanoshell coating. Upon near-infrared irradiation, a heat gradient is generated on the gold side and the micromotors exert directional thermophoretic motion.[10]

Janus particles are appropriate for multidrug loading or modification with functional molecules to allow separate drug release.[11] Xuan et al. prepared mesoporous silica nanoparticles half-coated with gold by vacuum sputtering. Mesoporous silica nanoparticles are known for their high cargo-loading capacity. Due to the photothermal effect of the gold nanoshell and consequent generation of gradients on that side, the particles exhibit a near-infrared-driven swimming behavior in water and a switchable feature of on/off cargo delivery.[12]

Despite their diverse applicability, there is still a limited number of application possibilities. This is probably because of challenges associated with the preparation of Janus particles, especially for diameters below 100 nanometers. Most published studies report lengthy and complex methods to fabricate Janus particles which consisted of two building blocks, owing complexity to the final structure and making its size fall into the submicrometer range. However, recent studies have shown that size and morphology of the individual domains can be controlled by adjusting the synthetic parameters, making it viable to produce Janus particles at the nanoscale.[7]

1.2 Preparation of Janus Particles

Janus particles can be prepared by a variety of methods, depending on the category they belong to. For instance, self-assembly, phase separation, seed-mediated polymerization and microfluidic preparation strategies can be employed to fabricate polymeric Janus particles.[13–16] Moreover, to prepare inorganic Janus particles, the nucleation and growth method, or masking methods are used.[17,18] To fabricate hybrid inorganic-organic Janus particles, combined masking methods and microfluidic synthesis can be employed.[19,20] This work will focus on the techniques used to prepare inorganic Janus particles.

1.2.1 Nucleation and Growth Method

The nucleation and growth method relies on the lattice mismatch of different components, in which only when the mismatch is large enough, a Janus structure can be produced.[8] Small lattice mismatches limit the materials that can be combined together to produce a Janus particle. While larger mismatches allow a wider combination of materials. It allows a precise control over the fabrication of the particles and the capability of fabricating particles at the nanoscale. However, this technique requires elevated activation temperatures. Hence, it is not suitable for a scale-up of production.[8] Heteroepitaxial growth-based Janus particles have been achieved via methods as thermal-decomposition methods, solvothermal method, hydrolysis of precursors and ion exchange methods.[8]

Gu et al. prepared Fe_3O_4-Ag nanoparticles by a liquid-liquid interface method. Fe_3O_4 nanoparticles were dissolved in an organic solvent and added to an aqueous solution of silver nitrate. Ultrasonication was applied to supply the necessary energy to form microemulsions stabilized by the Fe_3O_4 nanoparticles at the liquid-liquid interface. Reduction of Ag^+ on the exposed side of the Fe_3O_4 nanoparticles occurred, and further nucleation of silver took place (figure 2).[21]

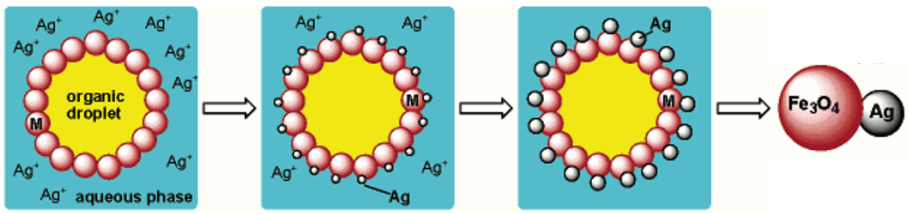

Figure 2: Synthesis of Fe_3O_4-Ag Janus nanoparticles. Adapted from [21]

Dumbbell-shape Au-Fe_3O_4 Janus nanoparticles were synthesized by Yu et al. via nucleation growth of Fe_3O_4 onto AuNPs by thermal decomposition of iron pentacarbonyl.[22] Au-Fe_3O_4 Janus nanoparticles show an 18 nm red-shift in comparison to the absorbance spectra of Au nanoparticles. The magnetization behavior of dumbbell particles remained superparamagnetic at room temperature. Another approach was used by Zhang et al., who developed silver-based Janus nanoparticles by a galvanic displacement method. Iron nanoparticles with a layer of iron oxide (Fe@Fe_3O_4) were prepared via pyrolysis of iron pentacarbonyl in 1-octadecene and oleylamine. When exposed in the air, the outer

Fe oxidized and a layer of iron oxide was formed. Later, oleophilic silver oleate (AgOA) was used to attach Ag to $Fe@Fe_3O_4$ nanoparticles. When AgOA enters in contact with $Fe@Fe_3O_4$, the recovered Ag attaches to the $Fe@Fe_3O_4$, resulting in $Ag\text{-}Fe@Fe_3O_4$ structures.[23] Hong et al. prepared $Au\text{-}Cu_2O$ Janus nanoparticles via a precise site-selective nucleation growth, in which Cu_2O was grown on hexoctahedral (HOH) gold nanocrystals. HOH gold nanocrystals have 48 triangular high-index {321} facets and Cu_2O is a semiconductor with a direct band gap of approximately 2 eV. In the presence of stabilizing agents, such as poly(vinylpyrrolidone) (PVP), a cetyltrimethylammonium bromide (CTAB)/sodium dodecyl sulfate (SDS) mixture, and SDS, the growth mode of Cu_2O on HOH gold nanocrystals can be manipulated. For example, in the presence of PVP, Cu_2O grows exclusively on the 8 vertices of the HOH gold nanocrystals pointing toward the <111> direction.[24]

1.2.2 Masking Methods

Masking methods are based on partially protecting the surface of the particle and modifying the exposed surface. In comparison to the nucleation growth method, the masking strategy is easy to scale up.

Masking is accomplished by either trapping the particles at the interface between two phases or by depositing or adsorbing them on a solid substrate. The exposed surface of the particle can then be modified with different functional groups. The functionalization of particles deposited on flat solid substrates (figure 3) provides numerous functionalization options, however it faces scalability limitations. Contrastingly, the entrapment of nanoparticles at the interface between two phases (figure 5) can overtake the scalability issues, but can limit the functionalization step which is dependent on the solvent used and the temperature at which it is made.[25]

Ma et al. have reported the deposition of a thin layer of Pt onto half of the surface of mesoporous silica nanoparticles by electron-beam evaporation.[26] Another example of the application of a masking method was reported by Pourrahimi et al., who have prepared ZnO-Pt Janus particles. ZnO microparticles were drop-cast onto a substrate, and asymmetrically coated with Pt by physical vapor deposition (PVD) (figure 3).[27]

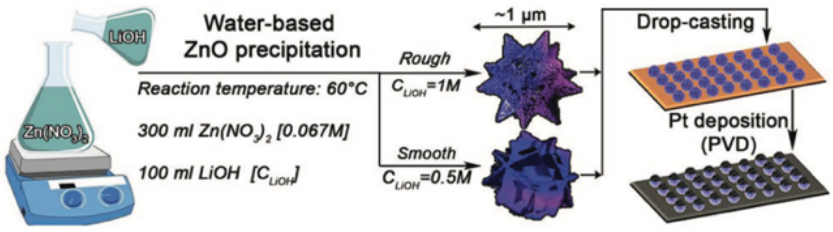

Figure 3: Synthetic procedure of ZnO-Pt Janus microparticles.[27]

The preparation of Janus particles by entrapment between different phases can be done in emulsions. Emulsions provide very large contact area between the two phases. By stabilizing the emulsion droplets with particles, the so-called Pickering emulsions, the particles become available for functionalization.

An emulsion is a system that consists of two immiscible liquids. The liquid droplets (or dispersed phase) are dispersed in the liquid medium (or continuous phase). To disperse the two immiscible liquids, an emulsifier or an emulsion stabilizer is required to stabilize the emulsion. There are two main types of emulsions:[28]

- Oil-in-water (o/w) emulsion, in which hydrophobic droplets are dispersed in water continuous phase;
- Water-in-oil (w/o) emulsion, in which water droplets are dispersed in an oil continuous phase.

An emulsion is only considered stable if it resists to physical changes over a period of time. Therefore, emulsion stability is a concern during storage and use. Emulsions are characterized by high interfacial tension, and consequently to decrease the surface energy, the dispersed droplets in an emulsion can undergo one of the following breakdown mechanisms: flocculation, creaming or sedimentation, Ostwald ripening, coalescence and phase separation (figure 4).[29]

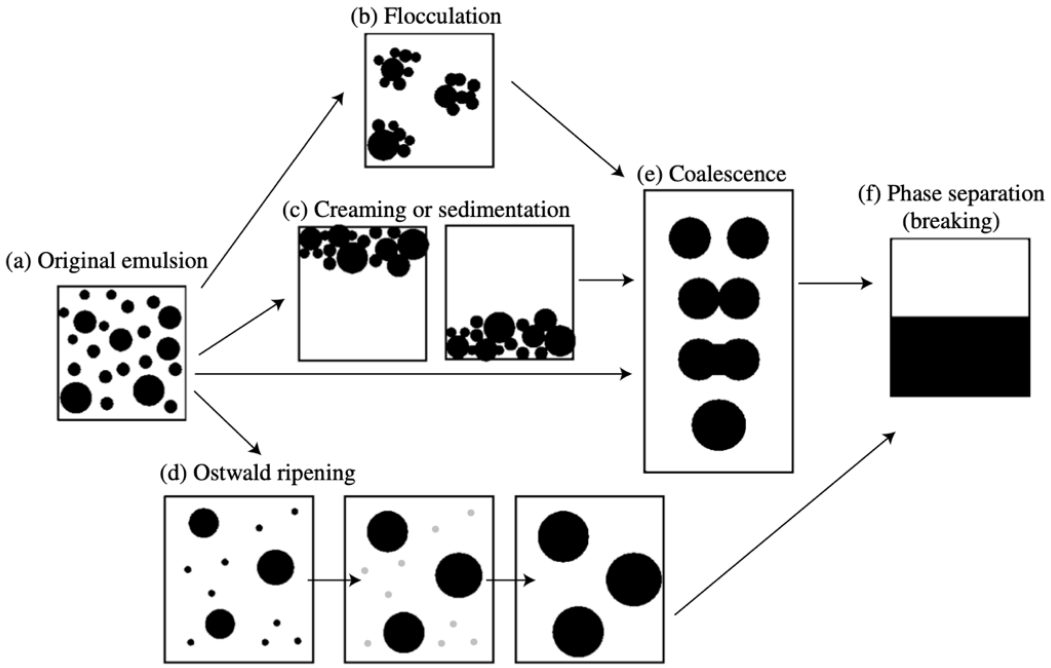

Figure 4: Processes involved in the breakdown of an emulsion. During flocculation, the droplets form aggregates and do not lose their original size. Creaming or sedimentation occurs due to density differences of the two immiscible liquids. Ostwald ripening occurs when the dispersed phase has a solubility limit in the continuous phase. Coalescence consists in the emergence of droplets to form larger droplets.[29]

The choice of the emulsifier or emulsion stabilizer is a crucial factor involving emulsion formation and its long-term stability, since it lowers the interfacial tension and prevents or retards the droplet flocculation and coalescence. There are three classes of materials that can act as emulsifiers and/or stabilizers: colloidal solids, polymers and surfactants.[28,30]

Pickering emulsions are emulsions stabilized by solid particles instead of surfactants.[28,31] Pickering emulsions have several advantages over traditional surfactant-stabilized emulsions, including low cost, low toxicity to the human body and strong stabilization, and lower susceptibility to factors such as pH, temperature and oil phase composition.[31] The effectiveness of Pickering emulsions is determined by several factors, being the most important the degree of wettability of the solid particles, since the particle adsorption at the oil-water interface is influenced by its hydrophobicity. The wettability of the solid particles determines the Pickering emulsion type and can be tailored by surface functionalization (physical adsorption or chemical anchoring).[32] The particle surface can be functionalized with hydrophobic or hydrophilic groups. For example, hydrophilic particles can be made partially hydrophobic by adsorbing a tensioactive in order to tune the penetration depth of the particles in the hydrophobic phase, such as in wax droplets.[33]

Solid particles adsorb at liquid-liquid interfaces, with an energy of adsorption depending on the contact angle (θ) of the particles at the oil-water interface. The liquid that is mainly wetting the particles is the continuous phase, while the other liquid is the dispersed phase. Therefore, hydrophobic particles (higher θ) wetted by the oil phase stabilize w/o emulsions; on the other hand, hydrophilic particles (lower θ) are immersed in the aqueous phase and stabilize o/w emulsions.[32,34] The desorption energy (E) of a particle from the liquid-liquid interface is given by equation 1, where R is the particle radius, $\gamma(po)$, $\gamma(pw)$ and $\gamma(ow)$ are the interfacial tensions between particle-oil, particle-water and oil-water, respectively.[5]

$$E = \pi R^2 \gamma(ow)(1 - |cos\theta|)^2 \quad (1)$$

$$cos\theta = \frac{|\gamma(po) - \gamma(pw)|}{\gamma(ow)} \quad (2)$$

The contact angle (θ) depends on the interfacial tensions between particle-oil ($\gamma(po)$), particle-water ($\gamma(pw)$) and oil-water ($\gamma(ow)$). When θ is 90°, the energy of adsorption is maximum and the particle is equally wetted by both liquid phases. From equation 1, it is clear that the formation of Pickering emulsions is favored by the increase of the particle size, hence achieving Pickering emulsions with particles below 100 nm is still a challenge.[5]

The final average droplet diameter (D) depends on the mass of solid particles (m_p), volume of the dispersed face (V_d) and surface coverage (c_f), which corresponds to the amount of droplet surface area covered per unit mass of solid particles. The surface coverage depends on the energy applied to the emulsification process to obtain the Pickering emulsion.[35]

$$\frac{1}{D} = \frac{c_f m_p}{6V_d} \quad (3)$$

The Pickering emulsion strategy has been widely used in the production of Janus nanoparticles.[7] In a typical example (figure 5), silica nanoparticles, water and paraffin are emulsified at a temperature above the melting point of the paraffin. Then, the emulsions are cooled down to 5°C to solidify the paraffin, and the stabilized droplets are dispersed in methanol and 3-aminopropyl triethoxysilane (APTES) at room temperature. The final step consists in dissolving the paraffin, obtaining silica nanoparticles with half surface functionalized with APTES.[36] A similar approach was reported by Perro et al., who used paraffin-in-water emulsions stabilized by silica particles, which were dispersed in an ethanol/aqueous ammonia mixture and APTES at room temperature. The paraffin was dissolved and Janus particles were obtained.[33]

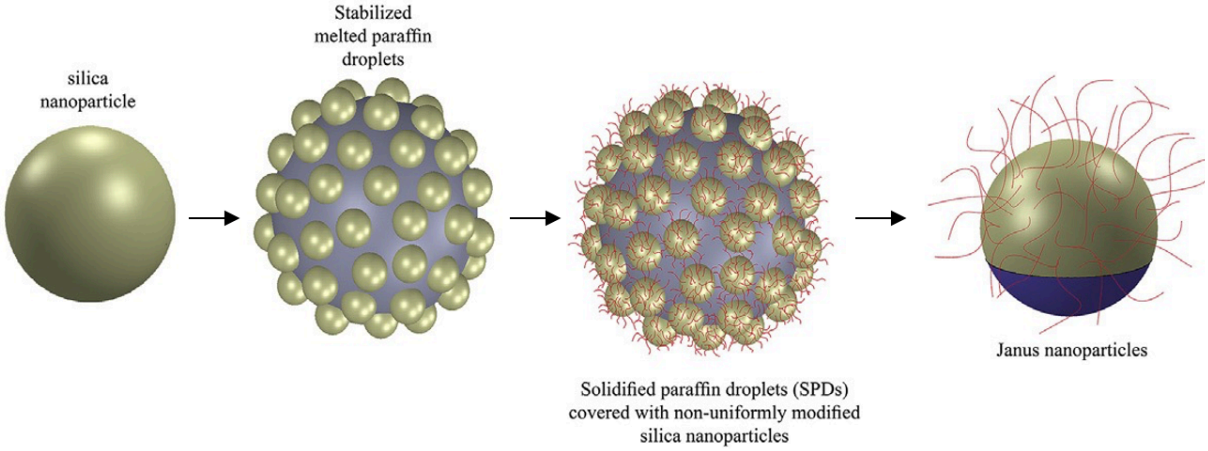

Figure 5: Scheme of Pickering emulsion strategy to produce Janus nanoparticles. Adapted from [36]

1.3 Self-propelled Janus Nanoparticles

Micro/nanomotors are devices at the micro/nanoscale capable of converting different sources of energy, such as chemical fuels, magnetic fields, electromagnetic radiation and ultrasound, into kinetic energy.[37] Due to their motion, turbulent flows are generated, allowing the transport of matter and the mixing and pumping of fluids without external agitation.[38]

Micro/nanomotors are inspired by some living organisms in nature, which perform tactic behaviors and are able to detect environmental changes in their immediate environment and move in response toward or away from specific locations (phenomena known as taxis). This has led to the development of motors capable of achieving self-propulsion and self-targeting.[39] Self-propulsion is achieved when micro/nanomotors are able to transform energy into movement. While self-targeting is achieved when in the presence of vector fields, these tactic motors can regulate their swimming direction toward or away from target locations, endowing such motors with targeted delivery functions.

Most of the micro/nanomotors present an asymmetric or tubular structure (like Janus nanoparticles), which allows them to reorient their direction toward specific gradients via an indirect aligning torque. By introducing a symmetry breaking structure, spontaneous directional motion is achievable.

1.3.1 Chemical Driven Motors

Chemical-driven motors are typically composed of two parts: an active part (usually catalytic) and an inactive part. Their motion depends on the catalytic decomposition of a fuel (H_2O_2, urea, etc) or the consumption of reactants to generate bubbles for propulsion. The chemical propulsion is due to a gradient of fuel decomposition products that accumulates in the active side of the motor. The chemical gradients are produced by the motors or can be supplied to the media.[37,40]

The catalysts used can be either inorganic or enzymatic. When partially coated with a catalyst, Janus motors asymmetrically produce bubbles (O_2, H_2, NH_3, etc) that induce a propelling force and velocity opposite to the catalytic part of the motor.

Chemical driven-motors can use inorganic metals or metal oxides (Pt, MnO_2, etc)[41] for the catalytic decomposition of fuels, or can be composed by inorganic materials (Mg, Zn, $CaCO_3$, etc)[42,43] that consume themselves. The use of a hydrogen peroxide as a fuel may cause biotoxicity, whereas motors capable of consuming themselves provide a more biocompatibility solution if no toxic by-products are produced.

Guix et al. proposed biodegradable and non-toxic $CaCO_3$/Co Janus motors. In the presence of citric acid, they move toward HeLa cells due to pH gradients, reaching velocities of 1.8 μm/s.[42] Liu et al. reported micromotors containing Mg, which reacts with water to produce hydrogen bubbles, providing propulsion. The Mg-motor had a short-life, however it was capable of reaching an average velocity of (57 ± 19) μm/s.[43] Another example of a chemical driven-motor was reported by Zhang et al., who prepared SiO_2/Pt Janus micromotors functionalized with spiropyran on the surface of the SiO_2 hemisphere. These micromotors exhibit self-propulsion in the presence of hydrogen peroxide upon UV irradiation, reaching a maximum velocity of 15 μm/s for a 15 wt% concentration of hydrogen peroxide.[41]

1.3.2 Acoustic-Driven Motors

Ultrasound energy derives from a high frequency sound wave (above 20 000 Hz) generated by an ultrasonic transducer. Ultrasound shows biocompatibility with relatively minor harm to the human body. Janus micro/nanoparticles, when exposed to an ultrasound field, experience acoustic pressure, which results in suspension, swarming, attraction or rotation.[44] Acoustic-driven motors present long-term motion compared to chemical energy-driven motors.[37,40] Ultrasound-induced swarming (defined as a collective behavior exhibited by micro/nanomotors) has a response time of only a few seconds regardless the dimension or morphology of the particles and can be tuned by altering the applied voltage and frequency.[45]

Wang et al. proposed a self-acoustophoresis-driven AuRu motor (1-3 μm long and 300 nm in diameter). The self-acoustophoresis force was generated between the concave Au end and the convex Ru end,

causing an asymmetric distribution of the acoustic pressure from the scattering of the incident acoustic waves at the metal surface. The scattering of acoustic waves from concave shapes accumulates energy near the curvature, while convex shapes scatter radially reducing the energy density near the curvature. As a result, the acoustic pressure is greater at the concave end (Au), propelling the rods with the Ru end forward.[46]

A challenge within acoustic-driven motors is the direction control. Incorporation of magnetic segments to the motor allows the direction control via external magnetic field actuation.[47] In these specific cases, ultrasound is used for propulsion of the motor, while magnetic fields for guidance purposes.

1.3.3 Magnetic-Driven Motors

Materials, such as Ni, Fe_3O_2, Fe_3O_4, Co, FePt, CoPt and $CoFe_2O_4$, have been used in magnetic-driven motors.[37] Magnetic fields are safe, practical and a versatile way to propel particles. Magnetic-driven motors are also more versatile than other external field-driven motors, since the field strength and direction can be easily tuned.

Ge et al. reported Janus micromotors containing Fe_2O_3 nanoparticles, ethoxylated trimethylolpropane triacrylate and 2-(perfluorooctyl) ethyl methacrylate. By using an external magnetic field, these motors can be directed to perform cooperative motions, such as alignment, rotation and directed transfer. The motors are stable and swim in a linear direction, reaching a maximum average speed of 128 μm/s.[48]

In general, the energy conversion process is independent of the surrounding of the particles, consequently magnetic-driven motors are less influenced by the ionic and biological media in comparison to chemical-driven motors.

1.3.4 Light-Driven Motors

Light is a renewable and inexpensive energy source, and depending on the light wavelength and intensity, it shows biocompatibility to the human body. Light-driven motors are easily controlled by light intensity and present a fast response to light irradiation as well as long-term motion. Ultraviolet (UV), visible or near-infrared (NIR) light have been used to propel micro/nanomotors.[49] UV, visible and NIR interacts with dipoles of single molecules, causing atoms to vibrate. The light-driven motors can be classified according to the type of mechanism responsible for propulsion: self-electrophoretic, self-diffusiophoretic, thermophoretic or bubble-induced propulsion.[37,49]

As a result, light is absorbed by a wide range of materials, increasing their temperature. Therefore, NIR is used in thermophoretic effect propulsion due to the heat generated. It can be simultaneously used to induce cell death by the photothermal effect.

The motion of light-driven motors is tuned by the intensity of light, the on/off status, the incident light direction and the wavelength of light.

1.3.4.1 Self-electrophoretic Effect

The self-electrophoretic effect consists in the production of an asymmetric distribution of ion loads to create an electric field that induces local flows, allowing the particle to move away or toward the light source.[37] When semiconductor materials, such as TiO_2, ZnO or Cu_2O, are irradiated with light, an electron can be promoted from the valence band (VB) to the conduction band (CB), forming electron-hole pairs. The photocatalytic generated holes (h^+) can react with water or hydrogen peroxide, producing H^+, O_2 and electrons can reduce H^+ to H_2.

Wang et al. prepared photocatalytic TiO_2-based micromotors that under UV light irradiation are able to move in water and hydrogen peroxide. These motors can self-propel with a velocity of 14.72 μm/s in water and 65.52 μm/s in hydrogen peroxide, under UV irradiation.[50]

Motors with self-propulsion by the electrophoresis effect exhibit a linear dependency between their velocity and light intensity (figure 6).[51,52]

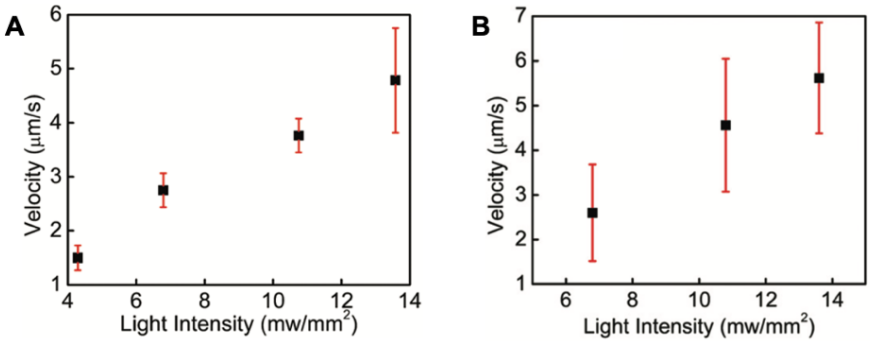

Figure 6: Linear dependence of velocity upon light intensity for Si/Au (A) and Cu2O/Au (B) micromotors. The mechanism of propulsion is self-electrophoresis for both micromotors.[51,52]

1.3.4.2 Self-diffusiophoretic Effect

The self-diffusiophoretic effect consists in the production of a gradient of solutes across the particle. Materials, such as AgCl, WO_3, Cu_2O, ZnO and Ag_3PO_4, can be chemically decomposed after being irradiated to UV light, creating ionic electrolyte concentration gradients around the particles. Consequently, an osmotic flow from low-to-high solute concentrations is generated, contributing to the self-diffusiophoretic motion. For example, UV light irradiation activates photochemical reactions around WO_3/Au micromotors, producing H^+, O_2^+ and ·OH, and as consequence a concentration gradient that contributes to the propulsion of the motor.[53]

1.3.4.3 Bubble-induced Propulsion

Bubble propulsion can be obtained by the catalytic decomposition of a chemical fuel (by transition metals, such as Pt, Mn, Ni or Ag) into individual oxygen bubbles.[54] For example, Li et al. reported amorphous TiO_2-Au Janus micromotors that generate oxygen bubbles by the photocatalytic decomposition of H_2O_2, achieving a 28% of quantum efficiency and 1.28 x 10^{-9} of power conversion

efficiency, which is about 10 times higher than that of catalytic bubble propelled motors based on H_2O_2 decomposition on Pt. This micromotor reached a maximum speed of 135 μm/s under UV light irradiation.[55]

1.3.4.4 Thermophoretic Effect

Some nanomaterials, such as Au, Ag, TiO_2, MoS_2 and Cu, absorb light and convert it into local heat. In the case of metallic nanomaterials, the electromagnetic energy is converted into heat through the surface plasmon resonance process, i.e., the heat is produced by a joule dissipation of oscillating electrons.[56] There are free electrons in metallic nanomaterials, which results in different surface plasmon due to the interaction of those electrons with the electromagnetic wave. The localized surface plasmon resonance occurs due to the excitation of the resonance of those confined electrons as shown in figure 7.[57]

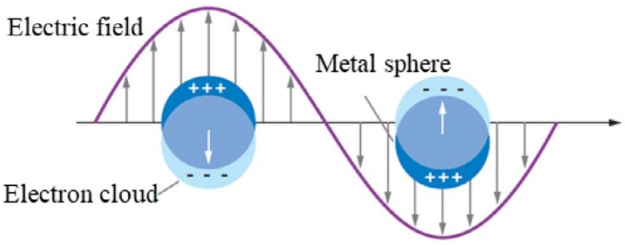

Figure 7: Absorption of electromagnetic radiation mechanism by metallic nanomaterials.[57]

Xuan et al. prepared mesoporous silica nanoparticles half-coated with a gold layer, that was deposited by chemical vapor deposition. Figure 8A shows the mean square displacement for three nanomotors with different diameters as function of time with and without NIR irradiation. The average velocities for 50, 80, and 120 nm nanomotors were 17.8, 11.8, and 8.1 μm/s, respectively. Evidently, smaller nanomotors swam faster than larger particles which face more resistance in the fluid. Additionally, larger nanomotors produce more heat due to a larger surface area of gold, however the resultant temperature gradient is weaker than that across smaller nanomotors because of the finite size effect. As the surface-to-volume ratio of the nanomotors increases (smaller nanomotors), phenomena such as the generation of temperature gradients across the particles become prominent. Figure 8B displays the nonlinear dependency between the speed of these nanomotors and the NIR intensity, which may be partially caused by the shift of the absorption peak because of melting and deformation of the gold half-shell due to the increasing in local temperature.[12]

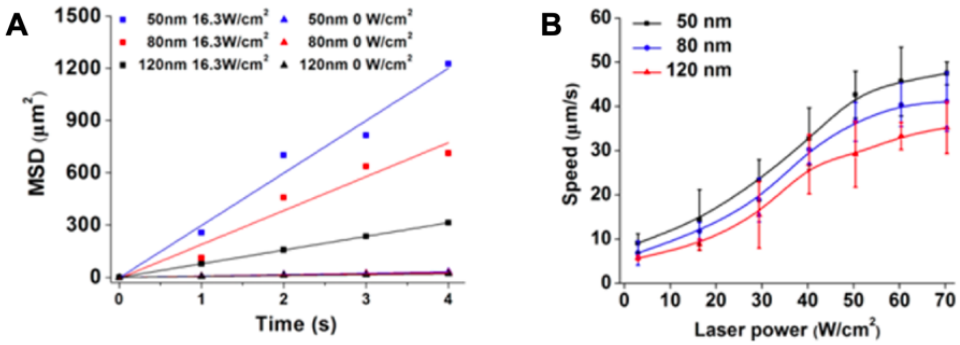

Figure 8: (A) Mean square displacement of Janus mesoporous silica nanoparticles half-coated with Au at NIR power of 16.3 W/cm^2 in 4 s. (B) Speed distribution under exposure to variable NIR powers.[12]

1.4 Light-propelled Silica-Gold Janus Nanoparticles

Silica-gold Janus nanoparticles are very promising structures due to their properties and versatility for changing the geometry and shell morphology.

Silica nanoparticles (SNPs) can be prepared by sol-gel methods and can posteriorly have their surface easily modified with amine, thiol and some other functional groups to strongly increase their interaction with gold nanoparticles. Gold nanoparticles (AuNPs) have a localized surface plasmon resonance that can be used for the photothermal effect. The growth of a gold nanoshell on a silica core can be achieved by a seeding method, where the shell is grown on a modified silica core with deposited gold nanoparticles. By controlling the nanoshell thickness, the optical properties of this system can be tuned for specific applications.[58]

1.4.1 Silica Nanoparticles

Silica is an inorganic material adequate for biomedical applications since it is biocompatible, endogenous (present mainly in bones), and recognized as safe by the U. S. Food and Drug Administration (FDA).[59] Consequently, silica nanoparticles have been widely used as supports or carriers in drug delivery, catalysis, imaging, and other applications.[60] The advantages of silica nanoparticles include facility to control their diameter and low size dispersion, biocompatibility and good colloidal stability. Also, silica nanoparticles are amiable to rich conjugation chemistry, allowing the incorporation of different groups into the silica network, such as fluorescent dyes. And the surface of silica nanoparticles can be functionalized postsynthesis with organic alkoxysilane compounds, for example to allow the synthesis of an inorganic shell.[60,61]

The sol-gel process has been extensively used to produce silica nanoparticles. The sol-gel process consists in the arrangement of a colloidal suspension (sol) which leads to the development of networks, and further gelation to form a system in the liquid phase (gel).[62] In 1968, Stöber et al. reported a method to produce monodispersed silica particles, ranging from 50 nm to 2 μm.[63] This method involves

hydrolysis and polymerization through a condensation mechanism of metal alkoxide precursors, like tetramethylorthosilicate (TMOS) or tetraethylorthosilicate (TEOS). According to the reaction conditions and the molar ratio of Si/H_2O, the alkoxide group is hydrolyzed. In basic media, the rate of hydrolysis is faster when compared to acidic conditions. Condensation follows hydrolysis, and an effective condensation depends on the hydrolysis stage.

Hydrolysis:

$$\mathrm{Si(OR)_4 + H_2O \rightleftarrows Si-(OR)_3OH + ROH} \quad (4)$$

Condensation:

$$\mathrm{(OR)_3-Si-OH + HO-Si-(OR)_3 \rightarrow [(OR)_3Si-O-Si(OR)_3] + H-O-H} \quad (5)$$

$$\mathrm{(OR)_3-Si-OH + OR-Si-(OR)_3 \rightarrow [(OR)_3Si-O-Si(OR)_3] + R-O-H} \quad (6)$$

In the presence of water, ammonia and ethanol, the hydrolysis of the silica source takes place. The hydrolysis (equation 4) involves a nucleophilic substitution of the ethoxy group (Si-OR) by silanol groups (-Si-OH), which increases the positive charge of silicon atoms and reduces steric hinderance. The use of ammonia as a catalyst accelerates the rate of hydrolysis and condensation, since the OH^- ions present in ammonia solution are more effective nucleophiles when compared to H_2O molecules.[64]

The complete hydrolysis to form $Si(OH)_4$ is difficult to achieve, thus condensation either occurs between two -OH or Si-OH and an alkoxyl group, forming bridging oxygen and a water or alcohol molecule (equations 5 and 6). Once a significant number of Si-O-Si bonds are formed, the oligomers condensate to form colloidal particles or sol. These particles bind over time, forming a three-dimensional network.[62]

The kinetics of the reactions influence the size, shape and morphological features of the silica nanoparticles. Parameters, such as temperature, concentration of the silica precursor, solvent in which the reaction occurs and pH at which the reaction takes place, play an important role.[64]

In the presence of ammonia as a catalyst, as its concentration increases, larger silica particles with a decreased polydispersity are formed. While in the absence of ammonia, silica flocculates in irregular shaped particles. With respect to the TEOS concentration, its increment leads to larger silica nanoparticles. An increase in the water concentration increases the rate of hydrolysis, thus coalescence of particles occurs due to stronger H-bonding, which means that larger particles are formed. Alcohols with long alkyl chains lead to larger silica particles.[63,64]

The temperature influences the rate of hydrolysis. As it increases, the hydrolysis rate also increases, enabling particle nucleation and leading to smaller and monodispersed particles.[64]

The pH of the media influences the surface charge of silica, and consequently it influences the hydrolysis and condensation rates. At pH 2, silica has the isoelectric point. At pH below 2, silica is positively

charged. While at pH above 2, silica is negatively charged. The reaction is usually carried at a basic pH to ensure the surface of the particle is negatively charged and to avoid aggregation.[64]

1.4.2 Gold Nanoshell Deposition

A gold nanoshell consists of a thin layer of gold, which can be grown by a seeding method.[65] This method consists in the deposition of gold nanoparticles, and further growth and coalescence of the particles to create a shell. Depending on the nanoshell thickness, the localized surface plasmon resonance can be tuned from the visible to the NIR. Due to this feature, when irradiated, silica-gold Janus nanoparticles create a temperature gradient on the gold halfshell side, resulting in self-propulsion.

1.4.2.1 Gold Nanoparticles

The interest devoted to gold nanoparticles arises from their attributes, such as size and shape related optoelectronic properties, large surface-to-volume ratio, excellent biocompatibility, and low toxicity.[66] The optical, electronic and thermal properties of gold nanoparticles (AuNPs), as well as their applications, depend on their size and shape. The size and shape can be controlled during the synthesis.[67]

Several techniques have been developed to obtain gold nanoparticles. In general, the methods involving a liquid to synthesize the particles are based on the chemical reduction of chloroauric acid, which consist of two significant factors:[68]

- The reducing agent (for example, citric acid, citrate, borohydrides, polyols and sulfites) that provides electrons, allowing the reduction of Au^{3+} and Au^{+} to metallic gold;
- The stabilizing agent, which is crucial to control the growth of the gold nanoparticles (size and shape) and to avoid aggregation.

Techniques such as the Turkevich method and the Brust-Schiffrin method can be used to produce gold nanoparticles, depending on the desired size and application.[68]

The Turkevich synthesis was introduced by Turkevich et al. in 1951[69], and it involves trisodium citrate as both stabilizing and reducing agent. A $HAuCl_4$ solution is boiled, and the trisodium citrate is quickly added under stirring. After a few minutes, a wine-red colloidal dispersion is obtained, indicating that gold nanoparticles with a size of about 20 nm are formed.[70] The mechanism has three main steps. Firstly, metal ions are quickly reduced and form metallic clusters of 1 to 2 nm in size. Secondly, while the reduction takes place, particles undergo coalescence, leading to a decrease in the number of particles. When they reach a diameter of 2.5 nm, the number of particles remains unchanged, however they grow in size due to the incorporation of gold atoms reduced in the solution. Thirdly, once their diameter is about 8 to 10 nm, the growth rate significantly increases.[68] The size and stability of the nanoparticles is influenced by the molar ratio of $HAuCl_4$/citrate, pH and temperature at which the synthesis is performed.[68] In 1973, Frens et al. refined the Turkevich method, and showed that by controlling the molar ratio of $HAuCl_4$/citrate, it is possible to obtain gold nanoparticles ranging from 15 to 150 nm, but particles larger than 20 nm were polydispersed.[71] Also, studies by Kimling et al. indicated that high

concentration of citrate stabilizes gold nanoparticles of smaller sizes, while low concentration of citrate originates larger particles and leads to their aggregation.[72] Another important factor influencing the synthesis of gold nanoparticles is the pH of the system, i.e., the presence of citrate changes the pH and influences the size and size distribution of gold nanoparticles. By varying the pH, nearly monodispersed particles with sizes from 20 to 40 nm were synthesized.[70]

Later, the Turkevich method was modified in order to allow the production of gold nanoparticles in the absence of heating, with the addition of sodium borohydride ($NaBH_4$).[68] Natan et al. produced gold nanoparticles with a size of only 6 nm, using citrate as a stabilizing agent and $NaBH_4$ as a reducing agent at room temperature.[73]

The Brust-Schiffrin method was introduced in 1994 by Brust et al.[74] and involves the preparation of thiolate-stabilized gold nanoparticles in organic solvents. A solution of $HAuCl_4$ is mixed with a toluene solution of tetraoctylammonium bromide (TOAB or TOABr), under vigorous stirring to induce the transfer of tetrachloroaurate into the organic phase. Later, dodecanethiol and sodium borohydride are added to the mixture. TOAB has the role of a phase transfer catalyst, while dodecanethiol and $NaBH_4$ act as a stabilizing and reducing agent respectively. Once the two phases are separated, the organic phase is evaporated and the excess of thiol is removed, in order to allow the precipitation of the gold nanoparticles. It is important to note that a fast addition of $NaBH_4$ and cooled solutions allow to produce smaller and more monodispersed gold nanoparticles.[68,70]

As mentioned before, the choice of reducing agent is an important step in the synthesis of gold nanoparticles. $NaBH_4$ is the reducing agent used in the Burst-Schiffrin synthesis, and its strength is much larger than that of citrate that is used as reducing agent in the Turkevich synthesis. Also, the reaction rate using $NaBH_4$ is much larger than that of using citrate. This has a direct influence on the size of the gold nanoparticles. Particles synthesized by the Burst-Schiffrin method are smaller than those synthesized by the Turkevich method.[70]

Physical properties of gold nanoparticles include localized surface plasmon resonance (LSPR), radioactivity and high X-ray absorption coefficient. With respect to the LSPR, in the case of gold nanoparticles, it can lead to surface-enhanced Raman spectroscopy (SERS), surface enhanced fluorescence (SEF), photothermal conversion, photochemical conversion and colorimetric responses.[75]

The plasmon resonance occurs when incident photon frequency (incident light) is resonant with the oscillation of the conduction electrons. Since the disturbance of the incident electromagnetic wave decreases with the depth of the metal, the resonance often occurs on the surface, thus being named as surface plasmon resonance (SPR). Nanoparticles are comparable in size to the wavelength of the incident light, leading to the occurrence of LSPR.[75] The LSPR is characterized by a plasmon resonance in the visible or near-infrared spectral ranges for gold nanoparticles that display light scattering, by a 10 nm shift for a molecular interaction, and the LSPR is affected by the surrounding of the nanoparticle surface. The LSPR can be modified by changing reagents and solvent surrounding the nanoparticles, by altering the shape of the nanoparticles, and by employing a core-shell structure.[68] In the case of small (approximately 30 nm) monodisperse gold nanoparticles, the SPR causes an absorption of light in the blue/green region of the spectrum (approximately 520 nm). As a result, the observable color

corresponds to transmitted wavelengths in the spectral region of red color. As the particle size increases, the absorption wavelength is red-shifted, yielding a solution with a blue or purple color. Furthermore, if the particle size continues to increase, the SPR wavelength moves towards the infrared region, and the color of the nanoparticles turns clear or translucent.[76]

Gold nanoparticles have the ability to convert the energy of electrons into kinetic energy. The moving electrons are scattered by the lattice, thus a part of the kinetic energy is transformed into vibration energy, which can be expressed in the form of heat. This phenomenon is known as the photothermal effect.[75]

1.4.2.2 Gold Nanoshell on a Silica Core

A gold nanoshell consists of a spherical layer of gold around a filled or hollow core. The plasmon resonance of a gold nanoshell can be easily tuned from visible to NIR range of the electromagnetic spectrum, by varying the aspect ratio of the shell thickness to the core diameter.[65]

Several strategies have been employed to synthesize core-shell silica-gold nanoparticles, the most common being the surfactant assisted seeding method.[65] In a typical approach, silica nanoparticles are first synthesized, and their surface is functionalized with 3-aminopropyl triethoxysilane (APTES). The surface functionalization step is crucial, since it is important to saturate the surface of the silica nanoparticles with APTES, in order to provide enough NH_2 groups that could link to gold nanoparticle seeds.[33] Figure 9 shows the synthetic procedure of core-shell silica-gold nanoparticles. The growth of the gold shell on the seeded surface can be done by different methods:

- Using an aged mixture of chloroauric acid and potassium carbonate, and reducing gold on nucleation sites by formaldehyde;[77–79]
- Using a mixture of chloroauric acid and trisodium citrate, and reducing gold with ascorbic acid;[78]
- Using an aged mixture of chloroauric acid and potassium carbonate, and reducing chloroauric acid with sodium borohydride.[80]

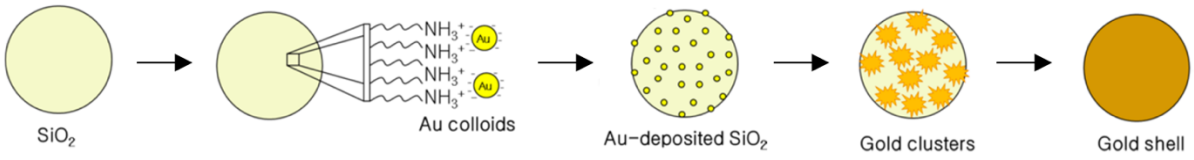

Figure 9: Schematic representation of the synthesis of core-shell silica-gold nanoparticles. Adapted from [78]

The bonding between gold nanoparticle seeds and silica nanoparticles is limited by interparticle coulombic repulsions.[80] To reduce this effect, several capping agents have been used, such as tetrakis(hydroxymethyl)phosphonium chloride (THPC) and mercaptoundecanoic acid (MUA). THPC is used to achieve higher coverage, since it is capable of reducing repulsive forces between carboxylic

acid groups on gold nanoparticle seeds.[79] On the other hand, MUA promotes covalent linking of the seeds via an amidation reaction between carboxylic acid groups on the gold seeds and NH_2 groups on the silica nanoparticles.[81] An alternative to capping agents is to add sodium chloride (NaCl) when mixing APTES functionalized silica nanoparticles and gold nanoparticle seeds, since it enables a higher seed deposition density due to electrostatic screening.[77]

The most remarkable characteristic of gold nanoshells is their tunability. The position of the plasmon resonance (extinction) peak and the contributions to absorption and scattering are determined by the shell thickness and core diameter. The LSPR of gold nanoshells can be tuned from 600 nm to greater than 1000 nm, which includes the NIR tissue window from 700 to 900 nm where tissue is transparent to light. The tunability of the LSPR of gold nanoshells over this wide range of wavelengths is due to the dielectric function of gold at optical wavelengths and their nanoscale dimensions.[82]

The Mie scattering theory provides analytical solutions of Maxwell's equations for scattering of electromagnetic radiation by symmetric spherical particles, and can be employed to calculate and understand the optical phenomena of gold nanoshells.[82] Extended Mie theory calculations show that while moving from a gold nanosphere to a gold nanoshell with decreasing its thickness, there is a red-shift in the plasmon resonance wavelength. Thinner gold nanoshells induce a more pronounced red-shift in comparison to thicker gold nanoshells.[83]

Using the extended Mie theory, Jain et al. calculated the extinction efficiency (Q_{ext}) spectrum of core-shell silica-gold nanoparticles.[83] Figure 10 displays the calculated Q_{ext} spectrum for 80 nm diameter silica nanoparticles with a gold nanoshell with different thicknesses. A decrease of 10 times in the thickness translates into a red-shift greater than 300 nm. Additionally, at the smallest thickness, which is 4 nm, a peak around 690 nm is observed, corresponding to the quadrupolar/higher-order resonance mode. Figure 11 compares the trend of the maximum plasmon resonance wavelength for four nanoshell diameters as a function of the thicknesses. As the nanoshell diameter increases and its thickness decreases, higher plasmon resonance wavelengths are reached.

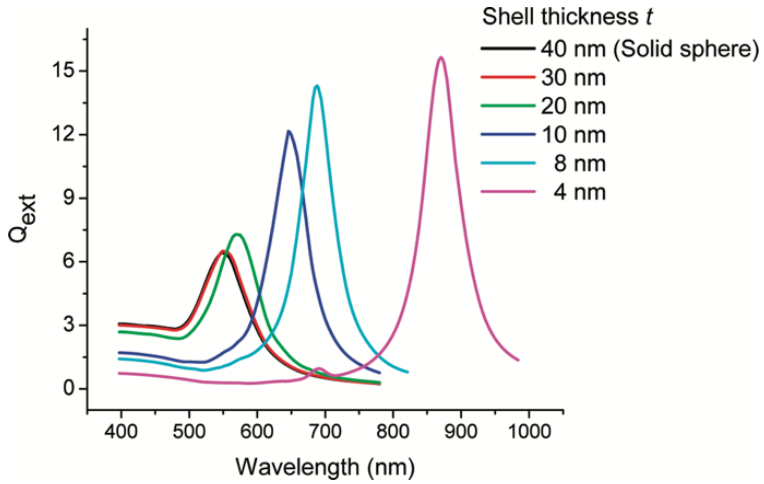

Figure 10: Calculated extinction efficiency spectrum of 80 nm diameter silica nanoparticles with a gold nanoshell with different thicknesses (t).[83]

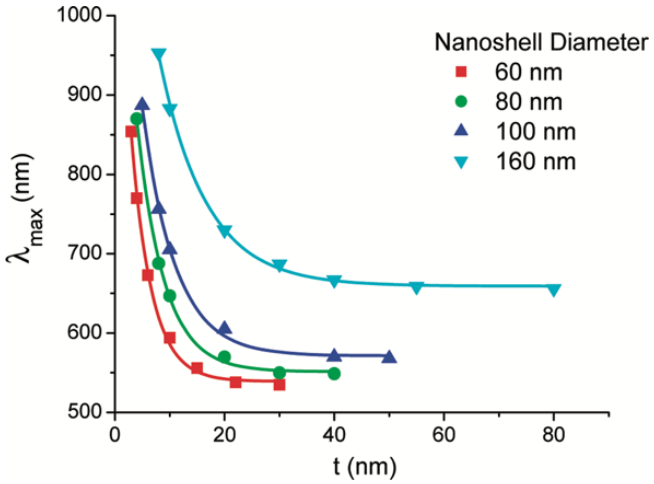

Figure 11: Calculated maximum plasmon resonance wavelength of silica nanoparticles with a gold nanoshell in water as a function of thicknesses (*t*).[83]

The maximum plasmon resonance wavelength (λ_{max}) for core-shell silica-gold nanoparticles, can be estimated by equation 7, where t is the gold shell thickness, R is the silica core radius, λ_0 is the maximum plasmon resonance wavelength of a solid sphere of the same size as the nanoshell, and $\Delta\lambda = \lambda_{max} - \lambda_0$ corresponds to the plasmon resonance shift.[83]

$$\frac{\Delta\lambda}{\lambda_0} = 0.97\ exp\left(\frac{-t/R}{0.18}\right) \tag{7}$$

Lee et al. prepared core-shell silica-gold nanoparticles, by growing the gold nanoshell using either formaldehyde or ascorbic acid as reducing agents.[78] Ascorbic acid is a mild reducing agent, which adsorbs on the seeded surface and does not create new nucleation sites, reducing the gold salt on the gold seeds already linked to the silica surface. This reducing mechanism occurs by the loss of one electron of ascorbic acid to form a radical cation, then by the loss of a second electron to form dehydroascorbic acid. In comparison to formaldehyde-derived silica-gold nanoparticles, ascorbic acid-derived silica-gold nanoparticles present stronger optical resonance and a smoother surface morphology with higher coverage of the gold shell (figures 12a-c). Figure 12d shows that the intensity and peak position of the plasmon resonance for ascorbic acid-derived silica-gold nanoparticles are stronger and red-shifted, respectively, which may be due to a smoother surface morphology resultant from the coalescence of small gold clusters.[78]

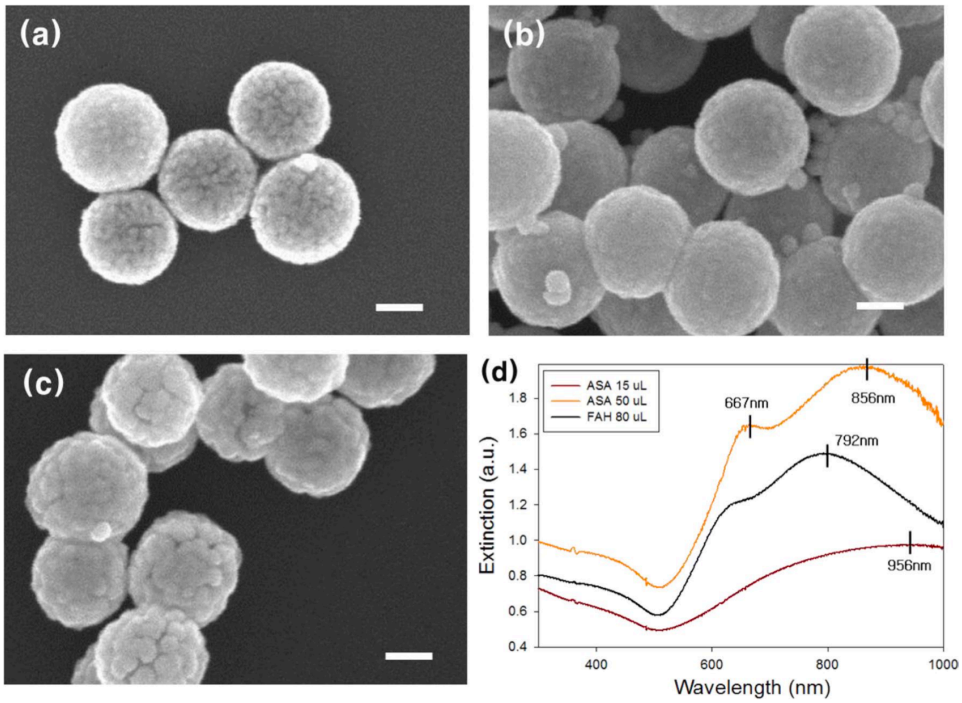

Figure 12: SEM images of silica-gold nanoparticles prepared by different reducing agents: (a) ascorbic acid = 15 µL, (b) ascorbic acid = 50 µL, (c) Formaldehyde = 80 µL. (d) Extinction spectra of silica-gold nanoparticles corresponding to the SEM images of a, b and c. The scale bar is 50 nm.[78]

1.4.3 Evaluation of Nanovehicle Propulsion

Anisotropic particles, such as, Janus nanoparticles, undergo two types of motion: translational diffusion and rotational (Brownian) diffusion.[84] The Brownian motion process consists in the movement of colloidal particles in the suspension medium in a random walk fashion.[84] The motion of light-propelled Janus nanoparticles can be investigated by dynamic light scattering (DLS). Scattering of coherent monochromatic radiation by a group of particles originates interference of scattered light which leads to intensity fluctuations in time. The characteristic time of scattered intensity fluctuations depends on the diffusion coefficient of the particles.[84] The particle mobility can be determined by correlating the intensity fluctuations of the scattered radiation at a constant angle. For anisotropic particles, the autocorrelation function ($g^{(1)}$) is given by equation 8, where A and B are scattering amplitudes, τ is the correlation time, $\Gamma_D = q^2 D_{eff}$ is the decay constant for translational diffusion in which $q = \frac{4\pi n}{\lambda} sin\left(\frac{\theta}{2}\right)$ is the scattering vector, and $\Gamma_R = \frac{1}{6\tau_R}$ is the decay constant for rotational diffusion:[85]

$$g^{(1)}(\tau) = Ae^{-\Gamma_D \tau} + Be^{-\Gamma_R \tau} \quad (8)$$

The autocorrelation function is related to the mean square displacement (ΔL^2) by equation 9.[85]

$$g^{(1)}(\tau) = Ae^{-\frac{q^2}{6}(\Delta L^2)} \quad (9)$$

Figure 13 displays the autocorrelation and ΔL^2 plots for anisotropic particles, i.e., Janus motors, versus the decay time. The step in the autocorrelation curve and the constant ΔL^2 at long decay times are an indicator of rotational diffusion of the anisotropic particles. While at short decay times, ΔL^2 exhibits a power-law slope, which is characteristic of translational diffusion.[85] Isotropic particles are characterized by only translational diffusion, therefore the autocorrelation curve tends to zero (figure 14), not having that step at long decay times.

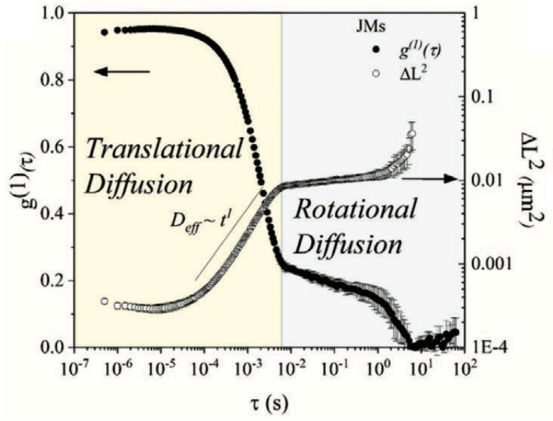

Figure 13: Autocorrelation and ΔL^2 of anisotropic particles versus decay times.[85]

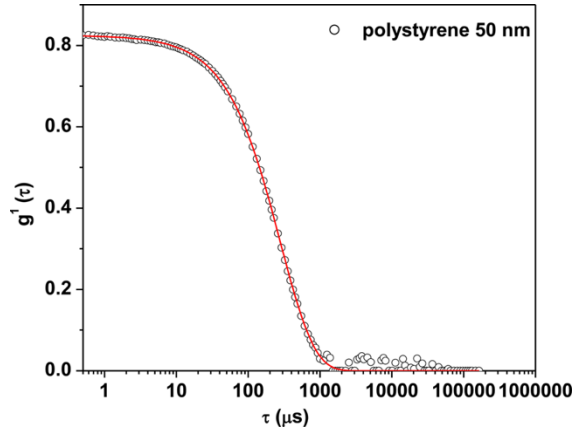

Figure 14: Autocorrelation of isotropic polystyrene particles versus decay times.[84]

The average directional speed (v) of anisotropic particles can be calculated from equation 10, where D_{eff} is the apparent translation diffusion coefficient under irradiation, D_0 is the translation diffusion coefficient without irradiation (corresponding to Brownian motion), and τ_R is the rotation relaxation time.[12]

$$D_{eff} = D_0 + \frac{v^2 \tau_R}{4} \quad (10)$$

The difference between the apparent translation diffusion coefficient under irradiation (D_{eff}) and the translation diffusion coefficient correspondent to Brownian motion (D_0) are related to the rotation relaxation time (τ_R) and to the average directional speed of the anisotropic particles. Therefore, larger differences between the diffusion coefficients indicate a higher directional speed of the particles.

Xuan et al. performed DLS studies on mesoporous silica nanoparticles half-coated with a gold layer.[12] They observed a decrease in rotational and translational relaxation times of the particles under NIR irradiation at 3 W/cm^2 (figure 15A). Additionally, they found that smaller particles exhibited a larger increase in both diffusion coefficients for increasing laser power (figures 15B and 15C). Regarding the average speed, since the rotation relaxation time decreases and the translation diffusion coefficient increases under NIR, the speed of the particles increases (figure 15D), which is in agreement with equation 10.

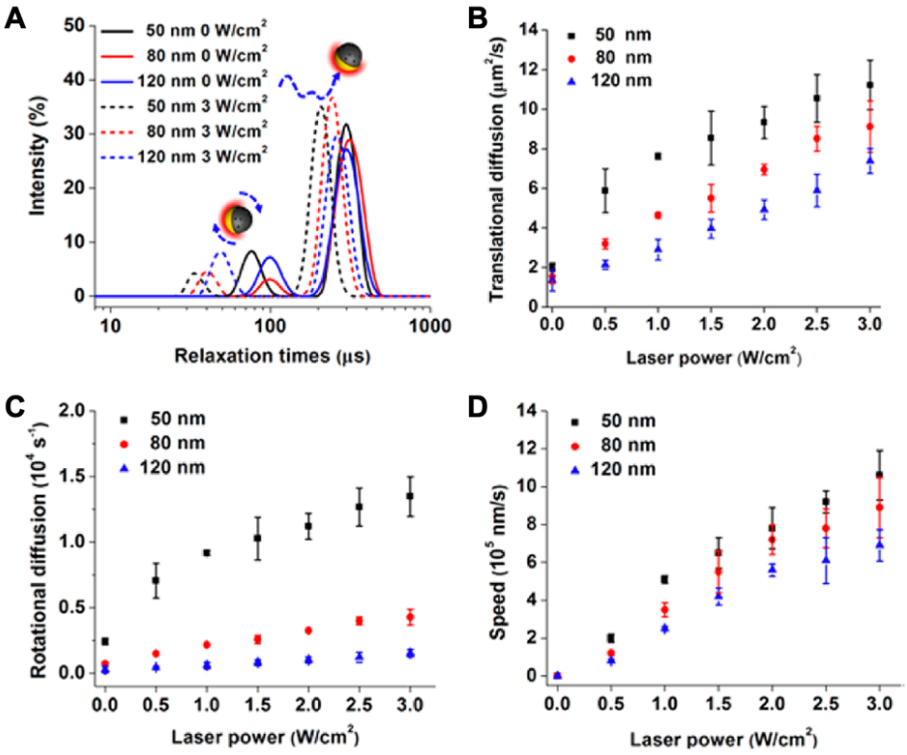

Figure 15: DLS characterization of NIR-driven mesoporous silica nanoparticles half-coated with a gold layer in water. (A) Translational and rotational relaxation plots of the 50, 80, and 120 nm particles without and with NIR irradiation at 3 W/cm^2. Translational (B) and rotational (C) diffusion coefficients at different levels of NIR irradiation power. (D) Average speed at different levels of NIR irradiation power.[12]

1.5 Objectives and Strategy

The aim of this work is to add self-propulsion capabilities to nanovehicles, transforming them in versatile nanorobotic tools for drug delivery applications. To achieve this, the work was focused on:

- Prepare Janus nanoparticles, composed by a silica core and a gold halfshell, via a Pickering emulsion route;
- Study the optical properties of the Janus nanoparticles by UV/Vis spectroscopy;
- Study the movement of the Janus nanoparticles under irradiation by Dynamic Light Scattering.

Regarding the preparation of the Janus nanoparticles, silica nanoparticles were used to stabilize Pickering emulsions, i.e., paraffin-in-water emulsions. The exposed surface of the silica nanoparticles was then functionalized with APTES, in order to saturate the surface, providing enough NH_2 groups to link gold nanoparticle seeds into a halfshell.

Due to the presence of the gold halfshell, the absorption spectrum of the Janus nanoparticles exhibits a plasmon resonance wavelength, which can be tuned to the NIR region of the spectra by varying the thickness of the shell.

Under NIR irradiation, the system is expected to produce a temperature gradient on the gold halfshell side due to the photothermal effect, acquiring self-propulsion.

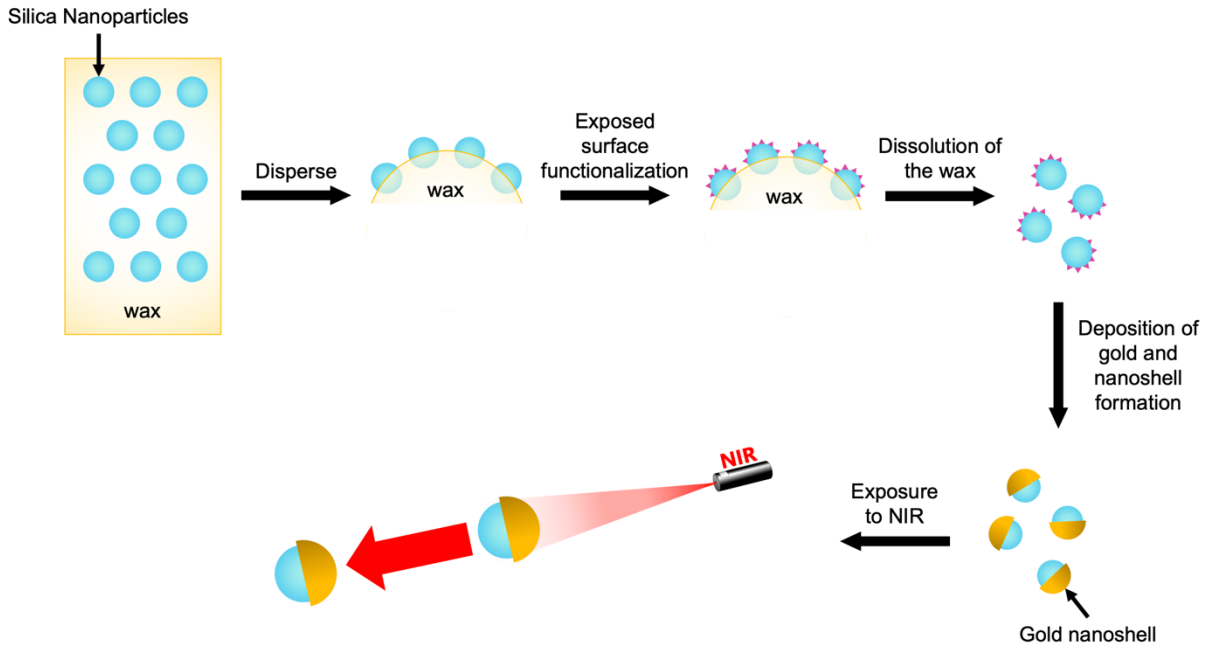

Figure 16: Schematic representation of the work developed.

2 Experimental Part

2.1 Materials

For the synthesis of Stöber silica nanoparticles, the following materials were used: absolute ethanol (Honeywell), ammonium hydroxide solution (NH_4OH basis, 28.0-30.0%, Aldrich), tetraethyl orthosilicate (TEOS, ≥ 99.0%, Aldrich) and deionized (DI) water, generated using a Millipore Milli-Q system ≥ 18 MΩcm (with a Millipak membrane filter 0.22 μm).

Pickering emulsions were produced using Stöber silica nanoparticles, distilled water, hexadecetyltrimethylammonium bromide (CTAB, ≥99%, Sigma) and paraffin wax (melting point 53-58 °C, Sigma-Aldrich). To dissolve paraffin wax, chloroform (> 99.8%, Sigma-Aldrich) was used.

Silica nanoparticles were surface modified with 3-aminopropyl triethoxysilane (APTES, 99%, Aldrich) in methanol (CIL) and in a mixture of absolute ethanol (Honeywell) and ammonium hydroxide solution (NH_4OH basis, 28.0-30.0%, Aldrich). Argon (Ar) (≥ 99.9999%) used was from Alphagaz Air Liquide.

To prepare the NMR analysis samples, 1,3,5-trioxane (≥ 99%, Fluka), deuterium oxide (D_2O, 99.9% atom, CIL) and sodium hydroxide (pure NaOH, EKA pellet) were used.

For the synthesis of gold nanoparticles, the following materials were used: deionized (DI) water, gold (III) chloride trihydrate (≥ 99%, Aldrich), sodium citrate dihydrate (≥ 99%, Aldrich) and sodium borohydride (> 98.5%, Aldrich).

To attach gold nanoparticles to the surface of silica nanoparticles, absolute ethanol (Honeywell) and sodium chloride (Merck) were used.

To promote the growth of the gold nanoshell, the following materials were used: potassium carbonate (> 99%, Aldrich), deionized (DI) water, gold (III) chloride trihydrate (≥ 99%, Aldrich), formaldehyde solution (36.5-38% in H_2O, Sigma-Aldrich), sodium citrate dihydrate, ascorbic acid (99%, Sigma-Aldrich) and sodium borohydride (> 98.5%, Aldrich).

2.2 Equipment

2.2.1 Centrifuge

The centrifugations were carried out in three different centrifuges depending mainly on the volume of the dispersion of particles. For higher volumes, Avanti J-30 I (Beckman Coulter, USA) with a 30.50 rotor was used. For the washing of particles in water or ethanol, the tubes used were made of polypropylene with a volume capacity of 40 mL. While the washing of particles in chloroform was performed in stainless steel tubes with a volume capacity of 40 mL. For intermediate volumes, Sigma 2K15 with a 12141 rotor was used. The tubes used were made of polypropylene with a volume capacity of 10 mL. For smaller volumes, the centrifugations were carried out on a Hitachi Himac CT 15RE in eppendorfs with volume of 2 mL.

2.2.2 Proton Nuclear Magnetic Resonance

^{1}H NMR spectra was obtained by a Bruker Avance III 400 spectrometer (Bruker BioSpin GmbH, Rheinstetten, Germany) operating at 400 MHz. Two solutions were prepared, a NaOH solution where 1 pellet was added to 4/5 mL of D_2O and a trioxane solution where 20.4 mg of trioxane were added to 5 mL of D_2O. Silica nanoparticles (5-10 mg) are added to the NaOH solution (400 µL), and sonicated until a clear solution is obtained. Afterwards the trioxane solution (50 µL) is added. And the final solution is inserted in a NMR tube.

2.2.3 Dynamic Light Scattering

Zetasizer Nano ZS (Malvern, model ZEN3600), with a 632.8 nm laser, was used to determine the hydrodynamic diameter.

The size of the particle is determined by the Stokes-Einstein equation (equation 11), where D is translational diffusion coefficient, k is Boltzmann's constant, T is absolute temperature and η is viscosity. The diameter measured is the hydrodynamic diameter, D_H, which refers to how the particle diffuses within a fluid.

$$D_H = \frac{kT}{3\pi\eta D} \tag{11}$$

All the measurements were carried out in a disposable polystyrene cuvette. The autocorrelation functions were analyzed by CONTIN method.

To obtain the particle size, 5 measurements with 12 runs of 10 seconds each were executed.

To perform the propulsion studies, the preparation of the sample involved its filtration with a 0.45 µm cellulose acetate filter for aqueous solutions, obtaining an almost transparent solution. Each sample

was slightly agitated during 2 minutes before executing the measurement. To measure the autocorrelation function, 8 sets with 15 runs of 15 seconds each were performed.

2.2.4 Ultra-Turrax

T18 digital Ultra-Turrax (IKA) and T25 easy clean digital Ultra-Turrax (IKA) were used to produce Pickering emulsions (figure 17). T18 is suitable for volumes from 1 to 1 500 ml (H_2O) and offers a wide speed range from 3 000 to 25 000 rpm. While T25 is suitable from 1 to 2 000 ml (H_2O) and offer a speed range from 3 000 to 25 000 rpm. The dispersing tool used for T25 was the S25N-18G dispersing tool (IKA).

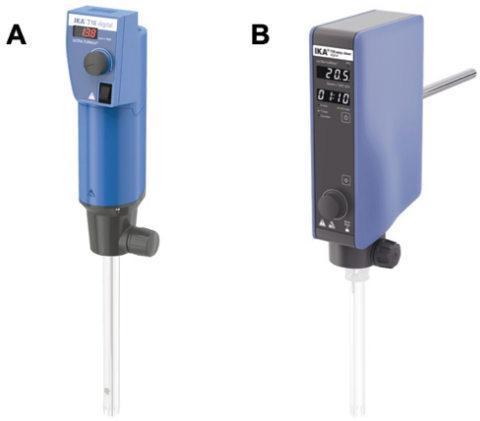

Figure 17: (A) T18 digital Ultra-Turrax and (B) T25 easy clean digital Ultra-Turrax.

2.2.5 Optical Microscopy

Optical Microscopy images were captured with a Kern Optics Optical Microscope (Kern & Sohn, Balingen, Germany), model OKM173. An incorporated camera Kern Optics Microscope Camera was used to acquire the images. The samples are prepared by dispersing the particles in water and drying them on a cover slip.

2.2.6 UV/Vis Spectroscopy

A Jasco V-660 UV/VIS Spectrophotometer (Oklahoma City, OK, USA) with a double monochromator and photomultiplier tube detector for higher resolution was used to obtain the absorbance spectra. The measurements were carried out in disposable cells at room temperature.

2.2.7 Transmission Electron Microscopy

Transmission Electron Microscopy (TEM) images of nanoparticles were captured with a Hitachi transmission electron microscope (Hitachi High Technologies, Tokyo, Japan), model H-8100, with a LaB6 filament (Hitachi) complemented with an accelerator voltage of 200kV. An incorporated camera

KeenView (Soft Imaging System, Münster, Germany) was used to acquire TEM images. The samples are prepared by dispersing the nanoparticles in ethanol and drying them on a carbon grid.

The software Image J was used to estimate the size of the particles, by measuring the diameter of at least 50 nanoparticles present in the images.

2.3 Methods

In this work, two types of nanoparticles were prepared. The first consist of a silica nanoparticle core with an isotropic gold nanoshell. The other are composed of a silica nanoparticle core with a half gold nanoshell.

2.3.1 Synthesis of Stöber Silica Nanoparticles

In a polypropylene flask, absolute ethanol (866.56 g), Milli-Q water (90.21 g) and NH_4OH (15.1 mL) were added and stirred at 40°C. After, TEOS (44.6 mL) was added to the mixture, and left overnight.

After cooling, the dispersion was centrifuged (90 000G, 20 minutes) and washed three times with absolute ethanol. The nanoparticles were dried at 60°C in a ventilated oven overnight.

2.3.2 Production of Pickering Emulsions

To produce a Pickering emulsion, 200 mg of SNPs were dispersed in 15 mL of distilled water. Then, CTAB was introduced at a concentration below the critical micellar concentration (~CMC/5, the critical micellar concentration of CTAB in water at room temperature is 0.92 mM).

The mixture is heated at 75°C, and 400 mg of molten paraffin are added drop by drop while maintaining vigorous stirring by means of an Ultra-Turrax homogenizer. A final stirring is accomplished by applying strong shear induced with an Ultra-Turrax in order to homogenize the as-synthesized emulsions. It is important to guarantee that the flask in which the emulsion is being produced is completely immersed in water to ensure that the temperature is homogenous in all the mixture and above the melting point of the paraffin wax. Figure 18 illustrates the assembly to produce Pickering emulsions.

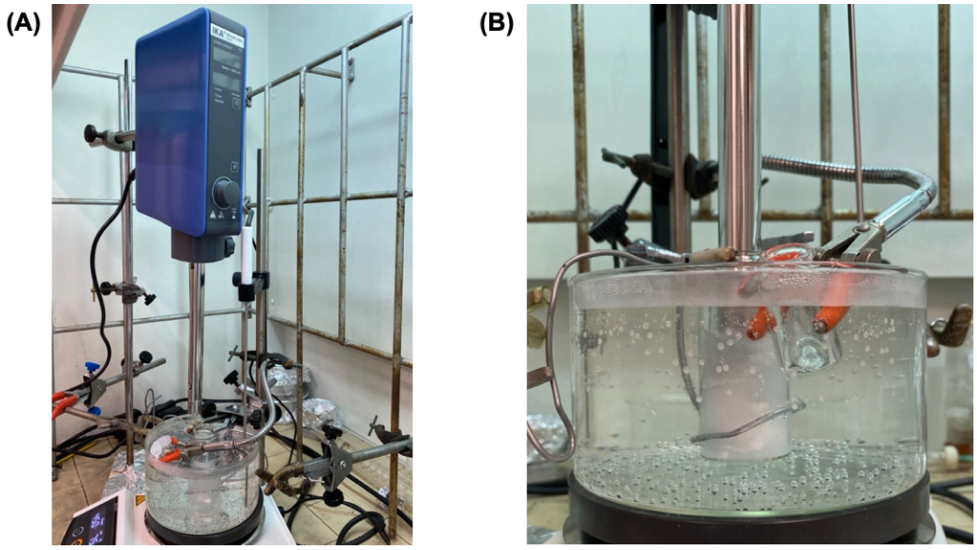

Figure 18: (A) Assembly to produce Pickering emulsions. (B) Flask in which the emulsion is produced is completely immersed.

The emulsions are cooled down to a temperature below the melting point of paraffin, CTAB is added to reach its critical micellar concentration, further stabilizing the paraffin dispersion.

The final dispersion was let to settle, and the supernatant was removed. After, the paraffin droplets stabilized by SNPs were recovered by centrifugation (80 000G, 15 minutes) and washed two times with water, they were dried at room temperature.

A summary of the conditions used to produce Pickering emulsions is presented in table 1.

Table 1: Conditions of Pickering emulsions.

Sample	**Silica Nanoparticles (mg)**	**Paraffin Wax (mg)**	**Distilled Water (mL)**	**Ultra-Turrax Conditions**	**T (°C)**
jSNP1	200	400	15	T18: 9 000 rpm	75
jSNP2	150	400	15	T18: 9 000 rpm	75
jSNP3	100	400	15	T18: 9 000 rpm	75
jSNP4	200	400	15	T18: 10 600 rpm	75
jSNP5	200	400	15	T25: 10 600 rpm	75
jSNP6	200	400	15	T25: 12 000 rpm	75

2.3.3 Surface Functionalization of Silica Nanoparticles

For the surface functionalization of SNPs, 3-aminopropyl triethoxysilane (APTES) was used. Initially, the quantity of APTES was tailored to obtain 2 molecules per nm^2 on the surface of the SNPs. Later, it was tailored to obtain 15 molecules per nm^2.

Homogeneous surface modification

To achieve a complete surface modification of SNPs with APTES, 250 mg of SNPs were dispersed in methanol (7 g) at room temperature. In another experiment, the same quantity of SNPs was dispersed in 15 mL of ethanol/aqueous ammonia mixture (7%, v/v) at room temperature. Then, APTES was added to the mixture and it was maintained at room temperature and under argon atmosphere during 48 hours. The nanoparticles were recovered by centrifugation and washed four times with absolute ethanol (70 000G, 10 minutes). They were dried at 60°C in a ventilated oven overnight.

The quantity of APTES to reach 2 and 15 molecules of APTES per nm^2 is 10.6 and 79.53 mg of APTES, respectively. These values are calculated using equation 12, where m_{APTES} is the mass of APTES and M_{APTES} is the molar mass of APTES.

$$m_{APTES} = \frac{total\ area\ of\ SNPs \times desired\ APTES\ molecules/nm^2}{Avogadro\ constant} \times M_{APTES} \quad (12)$$

Half surface modification

To accomplish a half surface modification of SNPs with APTES, the total amount of paraffin droplets stabilized by SNPs were dispersed in methanol (7 g) at room temperature. Then, APTES was added and the mixture was maintained at room temperature and under argon atmosphere during 48 hours. Assuming that SNPs are immersed in paraffin droplets and only half of their surface is exposed, the quantity of APTES required in the functionalization, in order to obtain 2 molecules of APTES per nm^2, was 4.24 mg.

In another experiment, the total amount of paraffin droplets stabilized by SNPs were dispersed in 15 mL of ethanol/aqueous ammonia mixture (7%, v/v) at room temperature. Then, excess APTES (79.53 mg) was added, the mixture was maintained at room temperature and under argon atmosphere during 48 hours. In this case, the quantity of APTES was not determined based on the previous assumptions.

The resultant particles were washed three times with absolute ethanol (70 000G, 10 minutes). The paraffin was then dissolved with chloroform, the mixture was centrifuged (5 000 rpm, 20 minutes) and the SNPs were recovered by centrifugation and submitted to a final washing with absolute ethanol (70 000G, 10 minutes). The particles were dried at 60°C in a ventilated oven overnight.

A summary of each experiment is presented in table 2.

Table 2: Conditions of surface functionalization of silica nanoparticles.

Sample	Methanol	Ethanol/Aqueous Ammonia Mixture (7%, v/v)	APTES (mg)	Targeted number of APTES molecules per nm^2
SNP1_f	✓		10.6	2
SNP2_f	✓		79.53	15
SNP3_f		✓	79.53	15
jSNP1_f	✓		4.24	2
jSNP4_f	✓		4.24	2
jSNP5_f		✓	79.53	15
jSNP6_f		✓	79.53	15

2.3.4 Synthesis of Gold Nanoparticles

Gold nanoparticles (AuNPs) were synthesized by reduction of $HAuCl_4$ with sodium borohydride in the presence of sodium citrate. 645 µl of 1% (w/v) sodium citrate were added to 100 mL of 0.01% (w/v) $HAuCl_4$ under vigorous stirring at room temperature. After 3 minutes, 3 mL of 0.1 M $NaBH_4$, prepared in ice-cold water, was added to the mixture. The color of the solution changes immediately from colorless to red (figure 19). After 30 minutes of stirring, the colloidal solution was left for 2 hours without stirring at room temperature. The gold nanoparticles were stored in a polypropylene flask at 4°C for further use.

Figure 19: Solution of gold nanoparticles (AuNPs).

2.3.5 Deposition of Gold Nanoparticles onto Silica Nanoparticles

Gold nanoparticles (AuNPs) were deposited onto the SNPs in the absence and presence of NaCl.

For the deposition without NaCl, 43 mg of surface modified SNPs were dispersed in 0.5 mL of absolute ethanol with sonication and introduced in a centrifuge tube with 16 mL of the gold nanoparticles solution. The dispersion was gently stirred overnight, centrifuged (15 300 rpm, 5 minutes), and washed four times with water. The resultant nanoparticles were dried at 60°C in a ventilated oven overnight.

For the deposition in the presence of NaCl, 29.25 mg of surface modified SNPs were dispersed in 1.5 mL of ethanol with sonication and introduced in a flask with the gold nanoparticles solution and a 1 M NaCl solution. The dispersion was gently stirred overnight, centrifuged (15 300 rpm, 5 minutes), and washed four times with water. The particles were redispersed in 3 mL of water.

The conditions for the deposition of gold nanoparticles onto SNPs are presented in table 3.

Table 3: Conditions of the deposition of gold nanoparticle seeds onto silica nanoparticles.

Sample	Silica Nanoparticles (mg)	Absolute Ethanol (mL)	Gold Nanoparticles Solution (mL)	1 M NaCl Solution (mL)
SNP3_Au1	29.25	1.5	38.5	3.478
SNP3_Au2	29.25	1.5	68.5	6.188
jSNP1_Au1	43	0.5	16	—
jSNP4_Au1	43	0.5	16	—
jSNP5_Au1	29.25	1.5	80	7.227
jSNP6_Au1	29.25	1.5	80	7.227

2.3.6 Growth of the Gold Nanoshell

The growth of the gold nanoshell on gold nanoparticle seeded SNPs was attempted by three different approaches. A summary of the three approaches to grow a gold nanoshell is presented in table 4.

Table 4: Approaches used to grow a gold nanoshell in each sample.

Sample	Reduction with formaldehyde		Reduction with sodium borohydride	Reduction with ascorbic acid
	Room Temperature	55°C		
jSNP1_Au2	✓			
jSNP4_Au2	✓			
SNP3_Au3				✓
SNP3_Au4				✓
jSNP5_Au2	✓	✓	✓	✓

Reduction with formaldehyde

Initially, two solutions containing potassium carbonate (K_2CO_3) and chloroauric acid were prepared. The preparation of the first solution, called as K-gold1, involved the dissolution of 25 mg of potassium carbonate in 100 mL of deionized water by stirring during 10 minutes. Then, 1.5 mL of a solution of 1% $HAuCl_4$ in water was added and it was left to stir overnight. While for the second solution, called as K-gold2, 60 mg of potassium carbonate and 1.5 mL of 25 mM of $HAuCl_4$ were dissolved in 100 mL of deionized water. This solution was left to stir during 1 day. During both aging periods, the color of the solutions changed from yellow to transparent.

The gold nanoshell of jSNP1_Au2 and jSNP4_Au2 was grown by dispersing 18 mg of gold nanoparticle seeded SNPs in 0.5 mL of milli-Q water, and adding it to 20 mL of K-gold1 solution while stirring. Then, 10 µL of a formaldehyde solution was added, and the solution become purple in less than 2 minutes. It was left stirring for 30 minutes. The solution was centrifuged (15 300 rpm, 5 minutes) and washed three times with water. The resultant nanoparticles were dried at 60°C in a ventilated oven overnight.

The growth of a gold nanoshell on jSNP5_Au2 was attempted at 55°C and room temperature. In the first method, 10 mL of K-gold2 solution and 200 µL of jSNP5_Au1 dispersion were mixed at 55°C during 10 minutes. Then, 25 µL of a formaldehyde solution was added and the solution was mixed for 15 minutes. The second method was performed at room temperature, in which 800 µL of K-gold2 solution and 9.2 mL of milli-Q water were mixed. Then, 250 µL of jSNP5_Au1 dispersion were added, and the solution was mixed for 10 minutes. 40 µL of formaldehyde solution was added at the end and the solution was mixed for 15 minutes. Both final solutions were centrifuged (15 300 rpm, 5 minutes) and washed three times with water, and redispersed in 10 mL of milli-Q water.

Reduction with sodium borohydride

This approach was employed to grow a gold nanoshell on jSNP5_Au2. Briefly, 50 mL of K-gold2 solution was heated to 50°C, and left to stir during 5 minutes. 100 µL of jSNP5_Au1 dispersion were added and the solution was mixed vigorously during 10 minutes. Then, 2.5 mL of 10 mM sodium citrate solution was added. And after 1 minute, 5 mL of 6.6 mM sodium borohydride solution (250 µL in 1-minute intervals) was added. Upon each addition of the sodium borohydride solution, the solution changed to a more pronounced purple color. The solution was mixed during 15 minutes, centrifuged (15 300 rpm, 5 minutes) and washed three times with water, and redispersed in 10 mL of milli-Q water.

Reduction with ascorbic acid

This approach was used to grow a gold nanoshell on SNP3_Au3, SNP3_Au4 and jSNP5_Au2. A 0.75 wt% sodium citrate solution was added to a 1.92 mM $HAuCl_4$ aqueous solution. Then, a specific volume of each dispersion of gold seeded SNPs was added. And finally, a 4 mM ascorbic acid aqueous solution was added. The volumes of each solution used to grow the three samples are presented in table 5.

Table 5: Conditions of the gold nanoshell growth by the reduction of chloroauric acid with ascorbic acid.

Sample	Sodium Citrate Solution (mL)	$HAuCl_4$ Aqueous Solution (µL)	Sample Volume (mL)	Ascorbic Acid Solution (mL)
SNP3_Au3	0.65	40	1.5	0.5
SNP3_Au4	1.30	80	1.5	1.0
jSNP5_Au2	6.5	400	0.120	5

3 Results and Discussion

In this work, Stöber silica nanoparticles (SNPs) were synthesized and further modified with amino groups. The surface modification was performed on half of the surface of the SNPs via a Pickering emulsion route, ensuring that gold nanoparticles (AuNPs) link to the available amino groups. The growth of a half gold nanoshell was accomplished by reduction of chloroauric acid with different reducing agents, such as ascorbic acid, sodium borohydride and formaldehyde. The resultant nanoparticles exhibit a Janus nanostructure, and upon irradiation behave as light-driven nanomotors.

A schematic of the experimental work is represented in figure 20.

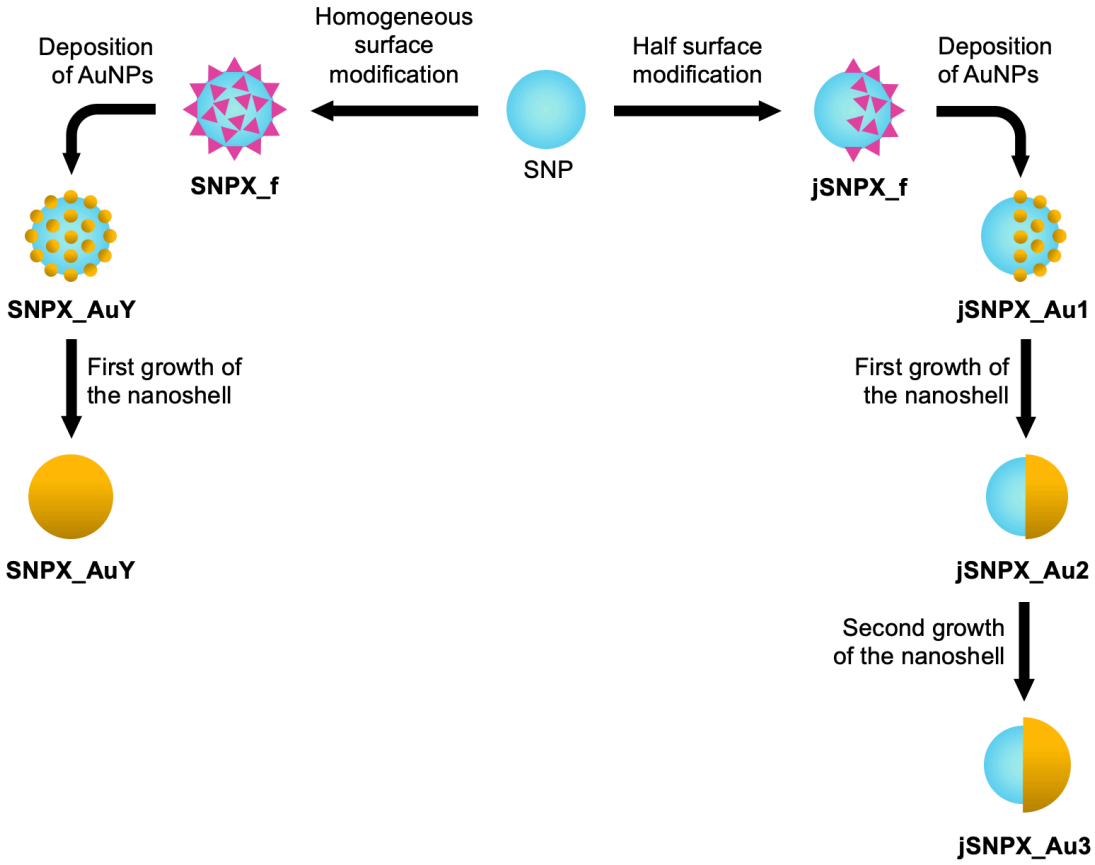

Figure 20: Schematic representation of the experimental work.

The codes attributed to each sample after the steps illustrated in figure 20, as well as the conditions used, are presented in table 6.

Table 6: Codes attributed to each sample after each step of the work.

		Surface modification		Deposition of AuNPs	
Samples	**SNP**	Homogeneous	**SNP3_f**	38.5 mL of AuNP solution with NaCl	**SNP3_Au1**
				68.5 mL of AuNP solution with NaCl	**SNP3_Au2**
	jSNP1	Half	**jSNP1_f**	16 mL of AuNP solution without NaCl	**jSNP1_Au1**
	jSNP4	Half	**jSNP4_f**	16 mL of AuNP solution without NaCl	**jSNP4_Au1**
	jSNP5	Half	**jSNP5_f**	80 mL of AuNP solution with NaCl	**jSNP5_Au1**

		1st growth of nanoshell (reducing agent)		**2nd growth of nanoshell (reducing agent)**	
Samples	**SNP3_Au1**	Ascorbic acid	**SNP3_Au3**		
	SNP3_Au2	Ascorbic acid	**SNP3_Au4**		
	jSNP1_Au1	Formaldehyde at RT	**jSNP1_Au2**	Formaldehyde at RT	**jSNP1_Au3**
	jSNP4_Au1	Formaldehyde at RT	**jSNP4_Au2**		
	jSNP5_Au1	Ascorbic acid	**jSNP5_Au2**		
		Formaldehyde at RT			
		Formaldehyde at 55°C			
		Sodium Borohydride			

RT = Room temperature

3.1 Synthesis and Characterization of Silica Nanoparticles

As previously described, SNPs were synthesized by the Stöber method. After the synthesis, the particle size was evaluated by means of Dynamic Light Scattering (DLS) and Transmission Electron Microscopy (TEM).

DLS measurements were obtained at 25°C and provide the hydrodynamic diameter of the particles. SNPs sizes were also analyzed by TEM to estimate the average diameter of the particles. The average diameters obtained from DLS and TEM are (69 ± 19) nm and (66 ± 8) nm, respectively.

The diameter obtained by DLS is only slightly higher than that obtained by TEM. Since DLS measures the hydrodynamic diameter, it accounts for the nanoparticle diffusion within a fluid; hence the hydrodynamic diameter is expected to be larger than the diameter measured by TEM because of the particle solvation sphere.

From the correlogram (figure 21) acquired from DLS measurements, it is possible to confirm that the SNPs were fully dispersed, with no aggregates observed.

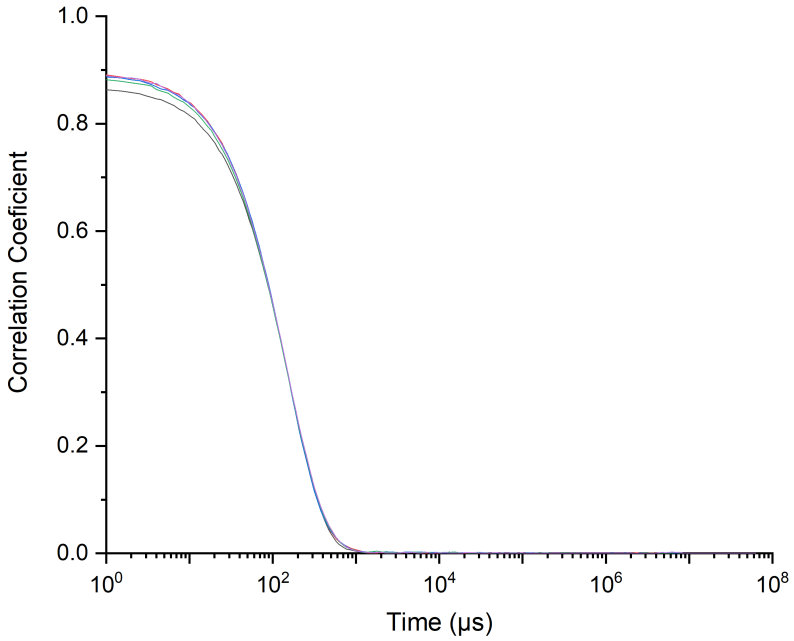

Figure 21: Correlogram obtained by DLS for SNPs.

TEM imaging allows visualization of the particles and analysis of their morphology and dimensions. Figure 22 shows the spherical morphology and uniform size distribution of the SNPs synthesized. Some aggregation is present, which can be justified by the sample preparation.

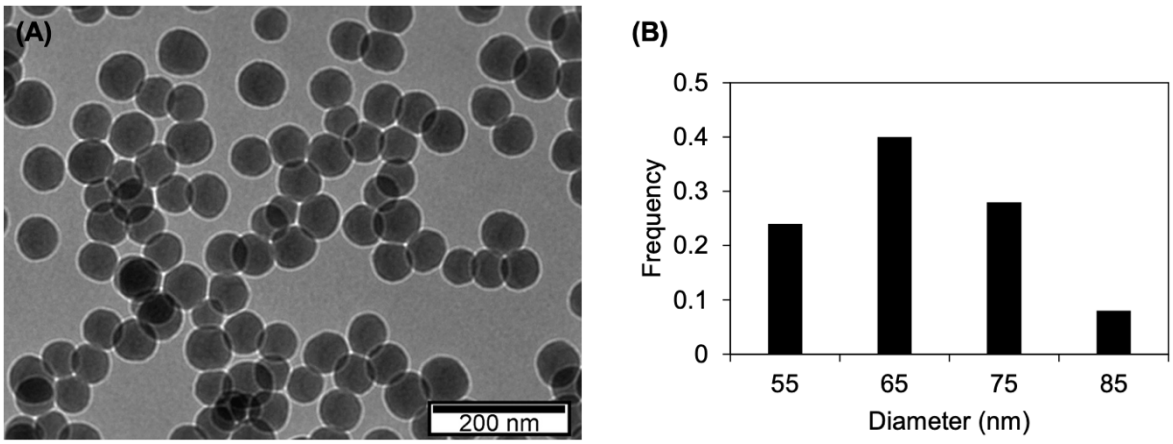

Figure 22: (A) TEM image (scale bar: 200 nm) of SNPs. D = (66 ± 8) nm. (B) Histogram size distribution.

3.2 Production and Characterization of Pickering Emulsions

Emulsions consisting of water and paraffin wax were stabilized by SNPs which were made partially hydrophobic by adsorbing CTAB. The adsorption of CTAB allows tuning the penetration depth of the particles in the paraffin droplets. After the emulsification process, the emulsions produced undergo sedimentation, which is caused by the density differences between water and paraffin droplets stabilized by SNPs. Figure 23 clearly shows this phenomenon.

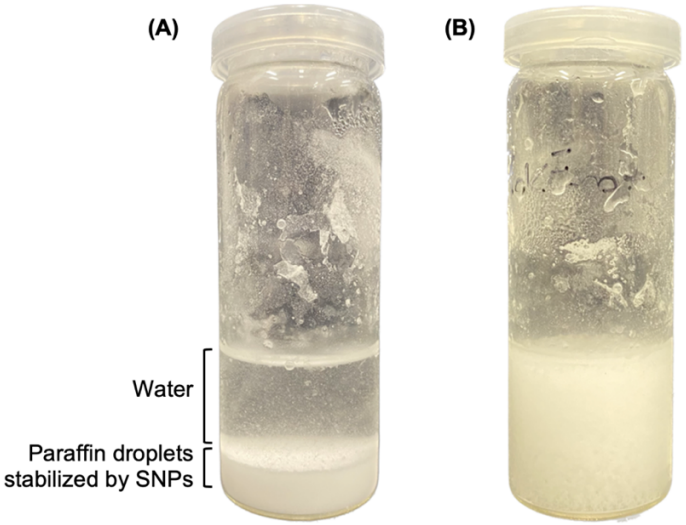

Figure 23: Emulsions obtained for the following conditions: 200 mg SNPs, 400 mg paraffin wax and T18 at 9 000 rpm. (A) Emulsions undergo sedimentation and (B) after slight agitation they are redispersed in water.

The expected droplet diameter is calculated by equation 3, assuming that half of each SNP penetrates the paraffin droplet, that all the SNPs are stabilizing the paraffin droplets and that all paraffin wax was emulsified. From figure 23, it is clear that not all the paraffin wax is emulsified, which can be justified by the formation of a vortex once the Ultra-Turrax is turned on. The expected and obtained droplet diameters are presented in table 7, as well as the conditions used.

Table 7: Conditions of the Pickering emulsions, and expected and obtained droplet diameter.

Sample	**SNPs (mg)**	**Paraffin Wax (mg)**	**Ultra-Turrax Conditions**	**Expected Droplet Diameter (μm)**	**Obtained Droplet Diameter (μm)**
jSNP1	200	400	T18: 9 000 rpm	4.6	10 ± 3
jSNP2	150	400	T18: 9 000 rpm	8.2	*
jSNP3	100	400	T18: 9 000 rpm	18.5	*
jSNP4	200	400	T18: 10 600 rpm	4.6	5 ± 1
jSNP5	200	400	T25: 10 600 rpm	4.6	3.5 ± 0.7
jSNP6	200	400	T25: 12 000 rpm	4.6	8 ± 4
* These values were not calculated because no droplets were formed.					

Pickering emulsions produced with 200 mg of SNPs and 400 mg of paraffin wax are expected to result in droplets with a diameter of 4.6 μm. However, from the first experiment, jSNP1 (figure 24), larger droplets were obtained, which can indicate that a lack of SNPs has been used or that the Ultra-Turrax speed was not enough to induce a strong shear in order to homogenize the emulsions.

As the mass of SNPs used decreases (jSNP2 and jSNP3), larger droplets are expected. However, when visualizing jSNP2 and jSNP3 by means of an optical microscope, no larger droplets were formed. By maintaining the initial conditions of SNPs and paraffin wax, and increasing the speed of the Ultra-Turrax from 9 000 to 10 600 rpm, in order to induce a stronger shear that is expected to create smaller droplets, droplets with a diameter of (5 ± 1) μm were obtained. Hence, the optimal conditions to produce Pickering emulsions were reached for jSNP4 (figure 25).

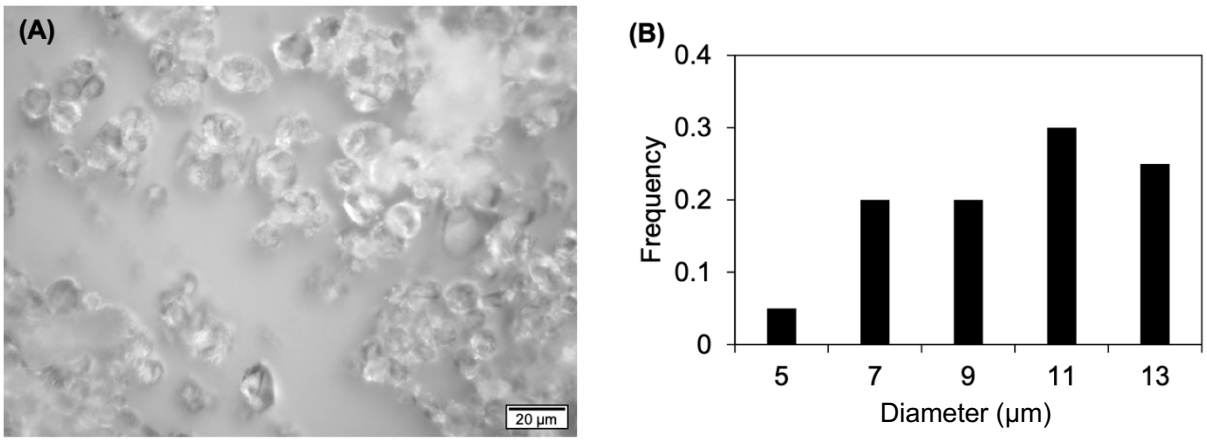

Figure 24: (A) Optical microscopy image (scale bar: 20 µm) of jSNP1. Obtained droplet diameter is (10 ± 3) µm. (B) Histogram size distribution.

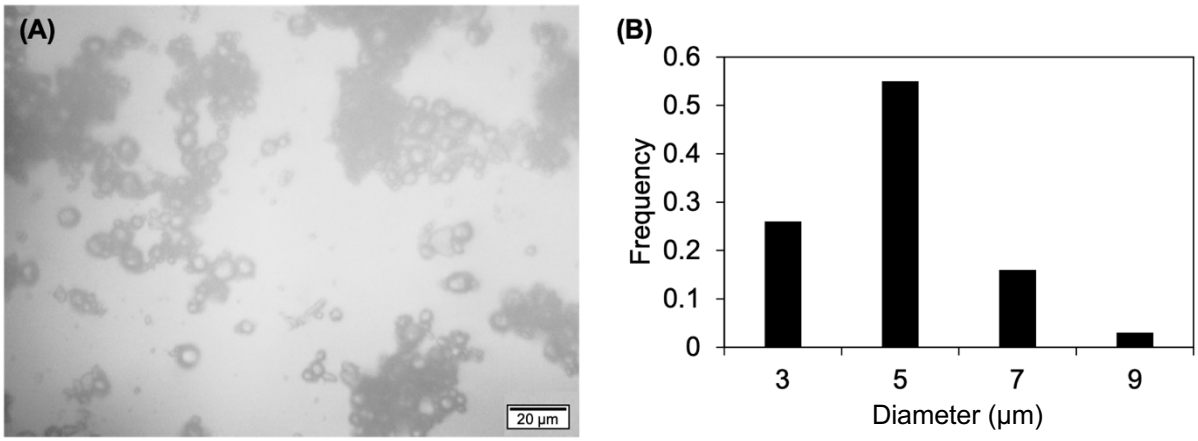

Figure 25: (A) Optical microscopy image (scale bar: 20 µm) of jSNP4. Obtained droplet diameter is (5 ± 1) µm. (B) Histogram size distribution.

jSNP5 were produced using the optimal conditions. However, smaller droplets were obtained (figure 26A), suggesting that not all the paraffin wax was involved in the emulsification process, which is confirmed in figure 26B where paraffin wax is visible in the upper walls of the flask. Also, from figure 26A, it is possible to observe non-uniformity in the droplets formed. Therefore, a decision to increase the speed of the equipment was made in order to induce more shear. Increasing the speed from 10 600 to 12 000 rpm allowed to obtain a more uniform distribution of droplets with larger sizes as shown in figure 27.

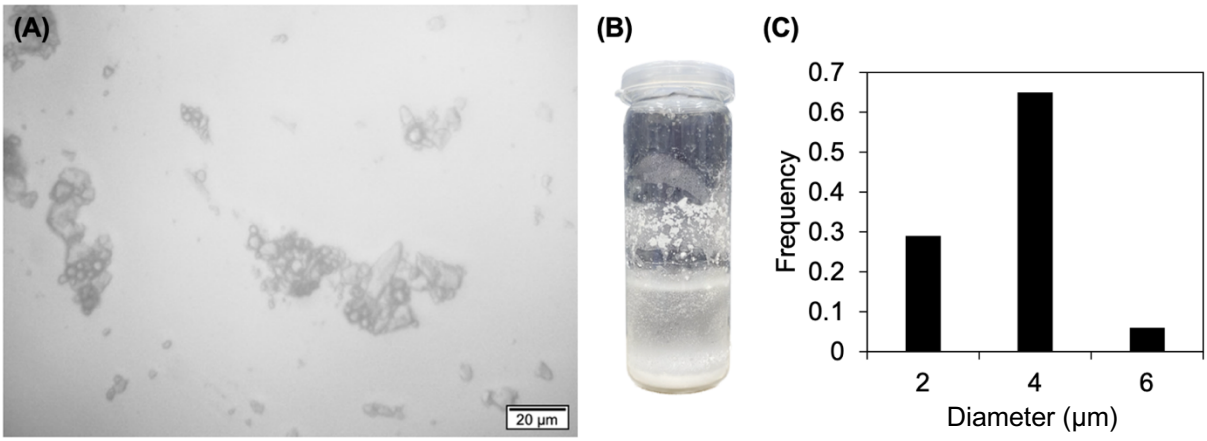

Figure 26: (A) Optical microscopy image (scale bar: 20 µm) of jSNP5. Obtained droplet diameter is (3.5 ± 0.7) µm. (B) Flask in which jSNP5 was produced. (C) Histogram size distribution.

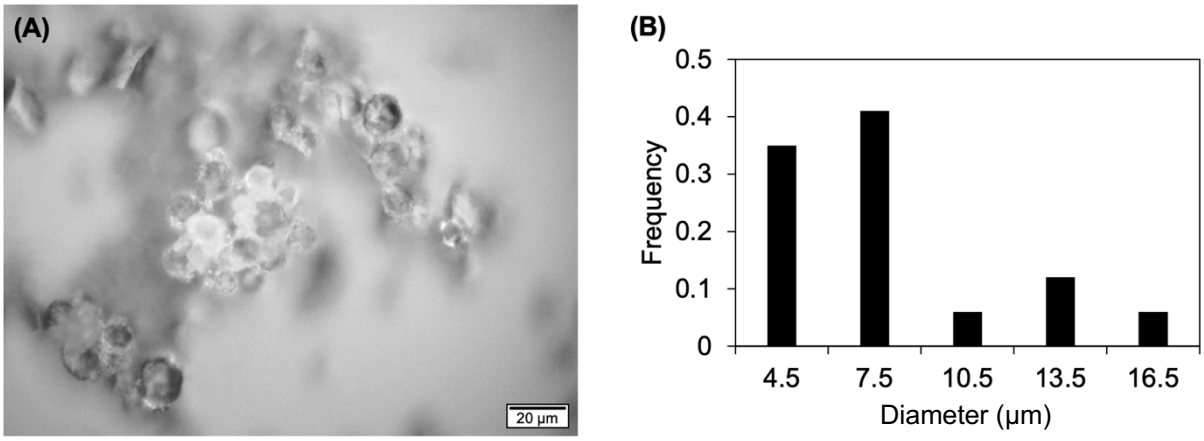

Figure 27: (A) Optical microscopy image (scale bar: 20 µm) of jSNP6. Obtained droplet diameter is (8 ± 4) µm. (B) Histogram size distribution.

3.3 Surface Functionalization of Silica Nanoparticles

To promote the deposition of gold nanoparticle seeds onto the SNPs surface, the particles were surface modified with 3-aminopropyl triethoxysilane (APTES) as represented in figure 28. APTES was added to SNPs or paraffin droplets stabilized with SNPs, dispersed in methanol or ethanol/aqueous ammonia mixture, and were maintained under argon atmosphere for 48 hours. Then, the SNPs submitted to a complete surface modification were recovered by centrifugation and washed with ethanol to remove compound not bonded to the surface. The SNPs stabilizing paraffin droplets were only half surface modified. These particles were first washed with ethanol, afterward paraffin was dissolved with chloroform, and the SNPs were recovered by centrifugation and submitted to a final washing with ethanol.

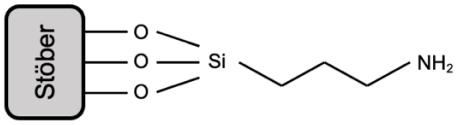

Figure 28: Schematic representation of the functionalization of SNPs with APTES.

The functionalization quantification was carried out via ^{1}H NMR as described by our group.[86] This method consists in the destruction of the nanoparticles with a solution of NaOH in a deuterated solvent, releasing the surface-bound groups into solution. An internal standard (trioxane) is used in the quantification.

The ^{1}H NMR spectra of SNP1_f and jSNP5_f are represented in figures 29 and 30, respectively. Spectra of SNP2_f, SNP3_f and jSNP4_f are in appendix 1.

At 4.79 ppm, it is possible to identify the D_2O peak, which is the reference used to correct spectrum shifts. The trioxane peak is at 5.18 ppm. Peaks at 2.49 ppm, 1.42 ppm and 0.36 ppm correspond to CH_2, CH_2 and CH_3 groups, respectively. The presence of these three peaks confirms that the surface of SNPs was modified with APTES. At 1.11 ppm and 3.58 ppm, the peaks represent the presence of residual ethanol from washing the particles, that remains entrapped in the matrix of the particles. While at 3.28 ppm, the peak corresponds to methanol and it is present in the ^{1}H NMR spectra of the nanoparticles functionalized in this solvent.

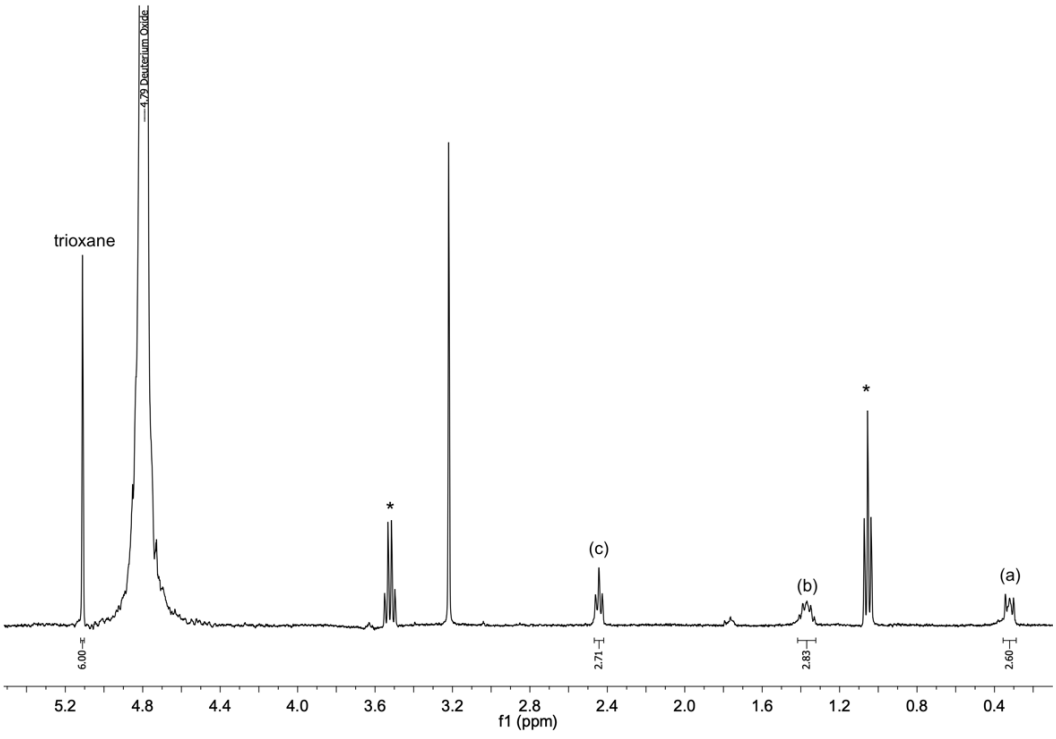

Figure 29: ^{1}H NMR spectrum of SNP1_f in D_2O: (a) corresponds to the CH_3 protons of APTES and (b) and (c) correspond to the CH_2 protons of APTES. Signed with * are the ethanol peaks and at 4.79 ppm is the D_2O peak. At 3.28 ppm is the methanol peak.

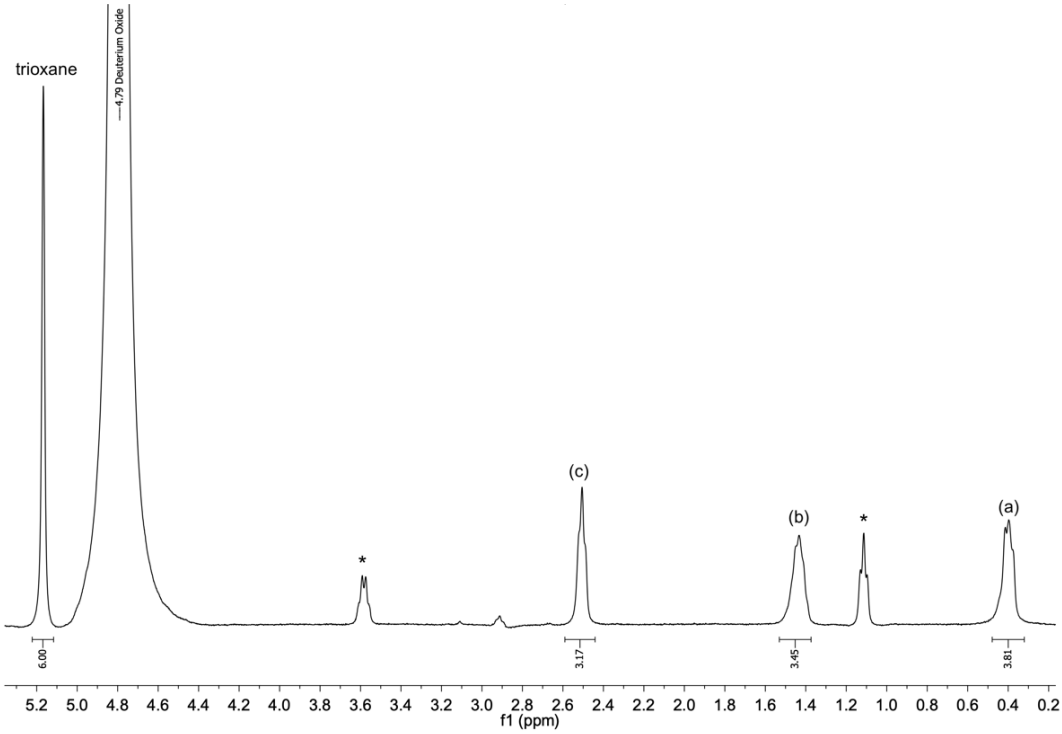

Figure 30: ^{1}H NMR spectrum of jSNP5_f in D_2O: (a) corresponds to the CH_3 protons of APTES and (b) and (c) correspond to the CH_2 protons of APTES. Signed with * are the ethanol peaks and at 4.79 ppm is the D_2O peak.

The peaks represented as (a) in figures 29, 30 and in appendix 1 were selected to estimate the number of APTES molecules grafted per nm^2 in the SNPs, through comparison with the integrated intensity of the trioxane peak. The results of the peak integration are presented in table 8.

Table 8: Functional group quantification by NMR.

Sample	**[APTES] mmol/g_{SNP}**	**Target Surface Coverage (molecules/nm^2)**	**Experimental Surface Coverage (molecules/nm^2)**
SNP1_f	0.49	2	5.1
SNP2_f	0.25	15	2.6
SNP3_f	0.54	15	5.6
jSNP1_f	0.050	2	1.1
jSNP4_f	0.073	2	1.5
jSNP5_f	0.76	15	16
jSNP6_f	0.50	15	10

The target surface coverage was not reached for the majority of the samples, except for jSNP5_f.

When functionalizing the total surface of SNPs, the quantity of APTES was tailored to have a surface coverage of 2 molecules per nm^2, to ensure a good functionalization without overlapping of APTES. However, a surface coverage of only 2 molecules per nm^2 was not enough to guarantee a high AuNP seed deposition density (results in the next sections). Hence, the surface coverage was then tailored to 15 molecules per nm^2. The functionalization in an ethanol/aqueous ammonia mixture (SNP3_f) resulted in a higher surface coverage of APTES than in methanol (SNP1_f and SNP2_f), because ammonia leads to the hydrolysis of APTES and to its efficient condensation on the SNPs surface.

In the case of half surface modification with APTES (jSNP1_f, jSNP2_f, jSNP3_f and jSNP4_f), the quantity of APTES was tailored to deliver 2 molecules per nm^2. Lower surface coverages were obtained, which can be justified by a low penetration depth of the SNPs in the paraffin droplets. If more than half of the SNP surface is exposed and the quantity of APTES is tailored for 2 molecules per nm^2, then it is expected to have less than that value of surface coverage. As mentioned before, the surface coverage was tailored to 15 molecules per nm^2 for the half surface modification, and higher surface coverages (jSNP5_f and jSNP6_f) were obtained because excess of APTES was used.

3.4 Synthesis and Characterization of Gold Nanoparticles

Gold nanoparticles (AuNPs) were synthesized by reduction of $HAuCl_4$ with sodium borohydride ($NaBH_4$) in the presence of sodium citrate. Sodium borohydride acts as the reductor agent and sodium citrate as a stabilizing agent. After the synthesis, the particle size was evaluated by Transmission Electron Microscopy (TEM), and the absorption spectrum was acquired by UV/Vis Spectroscopy.

Figure 31A and 31B show the spherical morphology and uniform size distribution of the AuNPs synthesized. The average diameter of the AuNPs is (4.9 ± 0.6) nm. The absorption spectrum (figure 31C) was obtained, and the SPR wavelength of the AuNPs is at 507 nm.

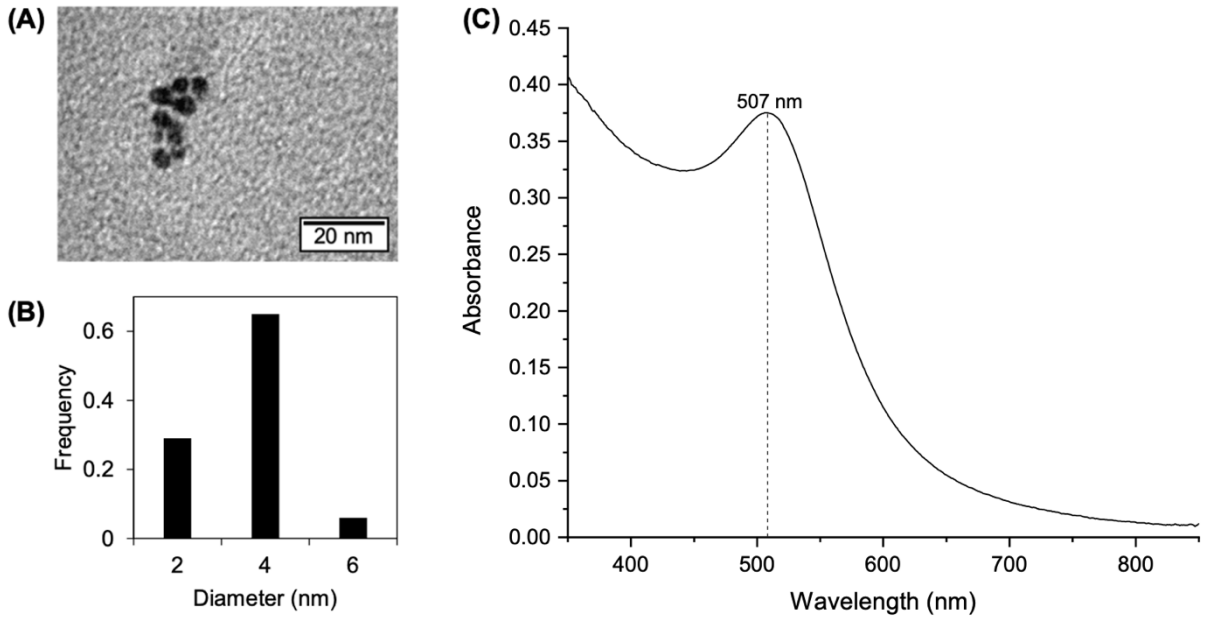

Figure 31: (A) TEM image (scale bar: 20 nm) of AuNPs. D = (4.9 ± 0.6) nm. (B) Histogram size distribution. (C) Absorption spectra of AuNPs.

3.5 Deposition of Gold Nanoparticles on Silica

After the functionalization step, AuNPs were deposited onto the surface of the SNPs in the presence and absence of NaCl. The gold seeded SNPs were then analyzed by UV/Vis Spectroscopy and Transmission Electron Microscopy (TEM). The AuNP seed deposition density is influenced by the surface coverage (APTES molecules/nm^2), volume of AuNPs solution used and presence of NaCl during deposition. Higher surface coverage translates into more NH_2 groups available to link to AuNPs. Also, an excess of AuNPs solution must be used, in order to ensure that all NH_2 groups are linked to AuNPs. With respect to NaCl, it reduces the electrostatic repulsion of the particles, allowing a higher AuNP seed deposition density. The presence of NaCl is responsible for an increased ionic strength; therefore, SNPs covered with amine groups will protonate more, allowing the adsorption of negatively charged AuNPs onto the positively charged surface of SNPs.

SNPs that exhibit high AuNP seed deposition density are expected to exhibit a more pronounced red shift of the absorbance peak. The wavelengths of maximum absorbance are presented in table 9, along with the parameters influencing the deposition.

Table 9: Conditions of the AuNPs deposition and absorbance peaks (nm) obtained.

Sample	Surface Coverage (APTES molecules/nm^2)	Gold Nanoparticles Solution (mL)	Presence of NaCl	Absorbance Peak (nm)
SNP3_Au1	5.61	38.5	✓	534
SNP3_Au2	5.61	68.5	✓	556
jSNP1_Au1	1.05	16	—	523
jSNP4_Au1	1.52	16	—	524
jSNP5_Au1	15.81	80	✓	534
jSNP6_Au1	10.36	80	✓	542

The deposition of a larger volume of the AuNPs solution in the presence of NaCl onto the surface of SNPs with equal surface coverage of APTES per nm^2 resulted in a difference of 22 nm of the absorbance peak (figure 32) between SNP3_Au1 and SNP3_Au2. TEM images (figure 33) confirmed that by using larger volumes of the AuNPs solution, higher coverage of the SNPs with AuNPs is reached. The red shift of the absorbance peak occurs mainly due to the plasmon coupling between neighboring AuNPs. Hence, a higher deposition density is expected to red shift the absorbance peak.

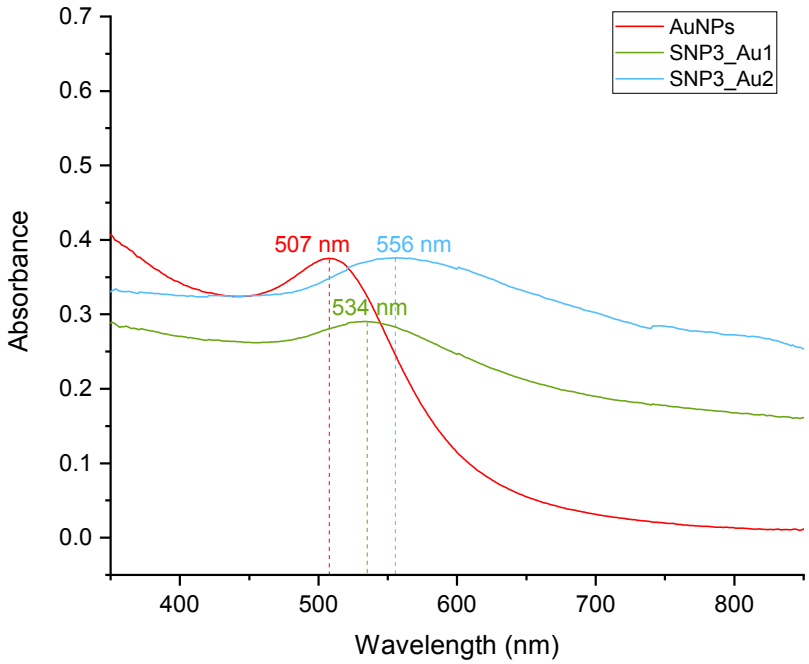

Figure 32: Absorption spectra of gold seeded SNPs.

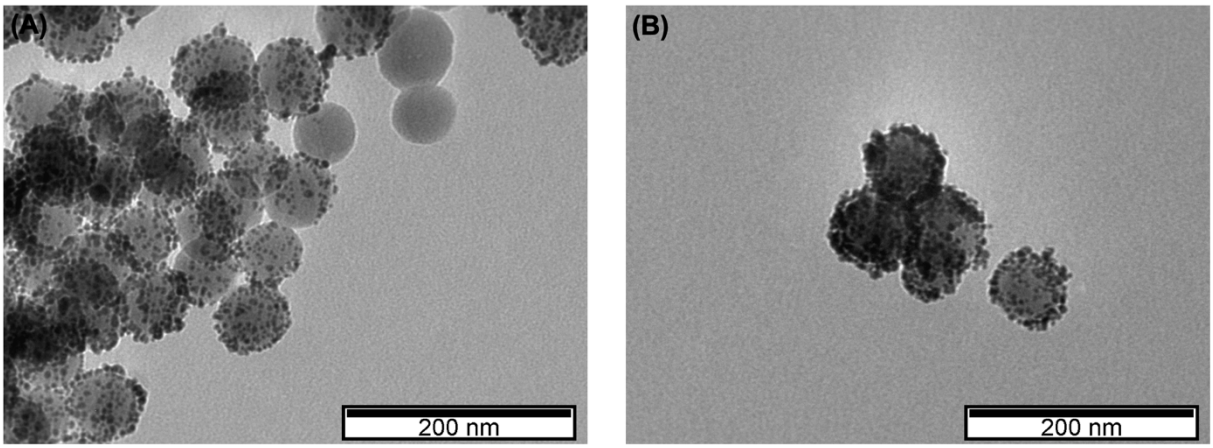

Figure 33: TEM images (scale bar: 200 nm) of (A) SNP3_Au1 and (B) SNP3_Au2.

With respect to the half gold seeded SNPs obtained by Pickering emulsification, the absorption spectra are represented in figure 34. jSNP1_Au1 and jSNP4_Au1 resulted from the deposition of AuNPs without NaCl onto SNPs with similar and low surface coverage of APTES per nm^2, and exhibited absorbance peaks at around the same wavelength with low intensity. While jSNP5_Au1 and jSNP6_Au1 were synthesized from SNPs with high surface coverage of APTES per nm^2, and more AuNPs were deposited in the presence of NaCl. Therefore, the combination of higher surface coverages and deposition with NaCl to reduce the repulsions of the particles allowed a more efficient adsorption of AuNPs to the SNPs surface. And their absorbance peaks red shifted in comparison to jSNP1_Au1 and jSNP4_Au1. However, the shift was not as pronounced as it was for SNP3_Au2 (table 9), because, for jSNP1_Au1 and jSNP4_Au1, only half of the SNPs surface had AuNPs adsorbed. The optical properties of the gold nanoshells vary with the shape factor (δ, $\delta = H/2R$ where H is the height and R is the outer radius). As the shape factor increases, the plasmon resonance is red-shifted.[87,88] The absorbance peak of jSNP6_Au1 is more red shifted than that of jSNP5_Au1, even though jSNP6_Au1 exhibited lower surface coverage of APTES. However, the obtained surface coverage is only an estimative because an assumption that all the SNPs were half penetrated in the paraffin droplets was made. In addition, the number of SNPs that were stabilizing the paraffin droplets is uncertain.

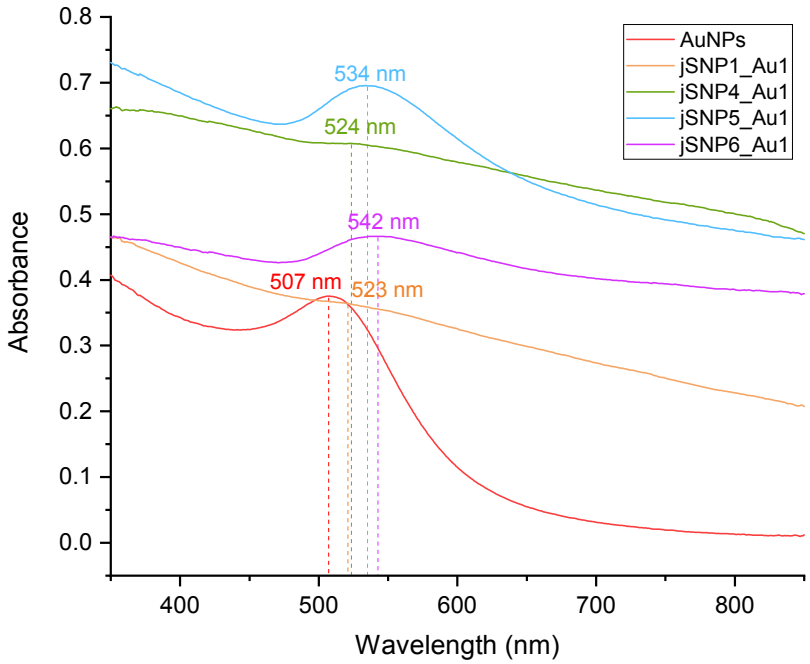

Figure 34: Absorption spectra of half gold seeded SNPs.

TEM images of jSNP5_Au1 and jSNP6_Au1 (figure 35) show evidence of areas of the SNPs surface that were not covered by AuNPs. However, some particles appear to be fully covered with AuNPs, which can be explained by how the particle is positioned on the grid relative to the electron beam. As illustrated in figure 36, depending on the angle at which the particle is visualized, its appearance on a TEM image can change. Other possibility to the appearance of particles fully covered with AuNPs can be that, during the Pickering emulsification, SNPs were not stabilizing paraffin droplets and therefore were completely surface modified with APTES, enabling the deposition of AuNPs onto the total surface of SNPs. On the other hand, in figure 35, SNPs without AuNPs are also visible, which can be justified by a total penetration of some SNPs into the paraffin droplets, impeding the half surface modification of the SNPs.

From figure 35A, it is clear that less than half of the SNPs surface is not covered with AuNPs, which is justified by the production of Pickering emulsions. This is an indicator that SNPs were only partially penetrated in the paraffin droplets.

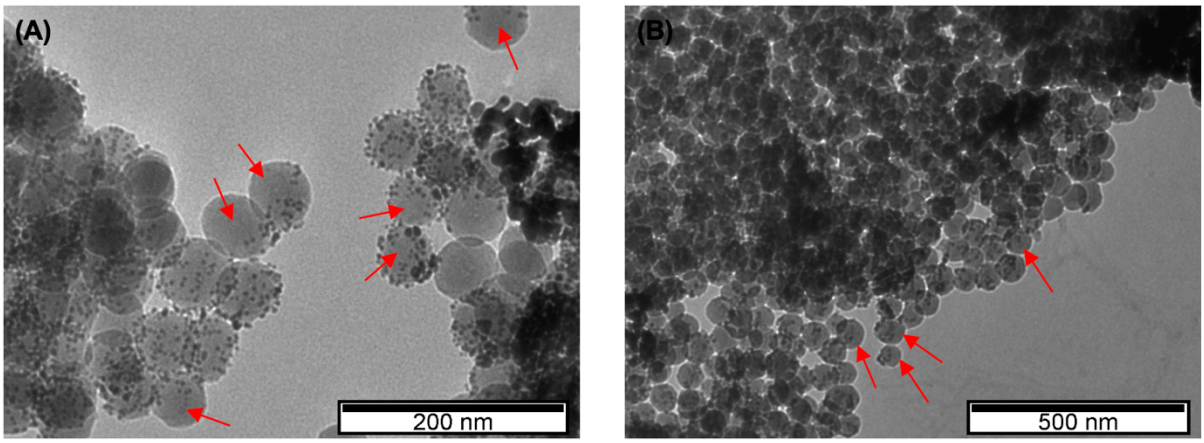

Figure 35: TEM images of (A) jSNP5_Au1 and (B) jSNP6_Au1. Red arrows indicate areas not covered by AuNPs. (scale bar: (A) 200 nm and (B) 500 nm)

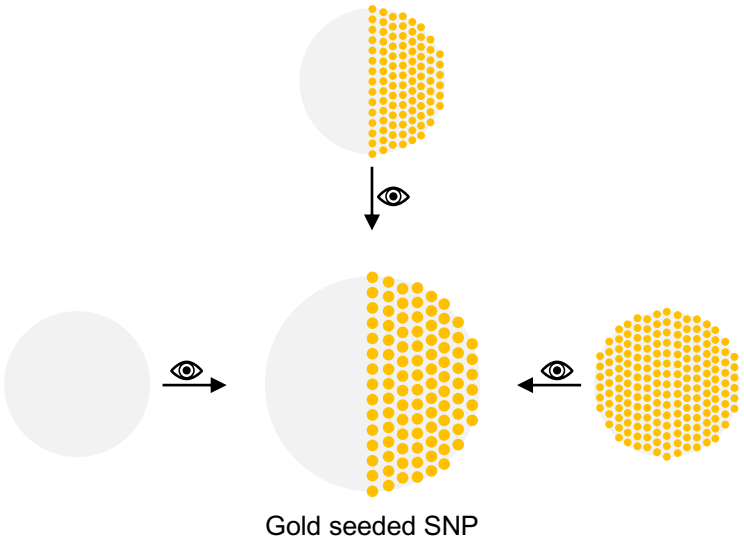

Figure 36: Expected TEM image of gold seeded SNPs depending on the angle at which it is observed.

3.6 Gold Nanoshell Growth

The growth of the gold nanoshell was first attempted on the total surface of the SNPs. Then, it was performed on half of the surface of SNPs to obtain Janus nanoparticles. The gold nanoshell was prepared using different concentrations of a reducible gold salt ($HAuCl_4$) with different reducing agents (ascorbic acid, $NaBH_4$ and formaldehyde).

The silica-gold nanoparticles synthesized were analyzed by UV/Vis Spectroscopy and Transmission Electron Microscopy (TEM).

The gold nanoshell was grown in SNP3_Au1 and SNP3_Au2, originating SNP3_Au3 and SNP3_Au4, respectively. The growth of the gold nanoshell in gold seeded SNPs by reduction with ascorbic acid for SNP3_Au3 and SNP3_Au4 resulted in an 8 nm and 7 nm shift of the absorbance peaks, respectively, in comparison to the absorbance peaks of the gold seeded SNPs. This confirms that the AuNPs adsorbed at the SNPs surface did grow, as revealed by figure 37.

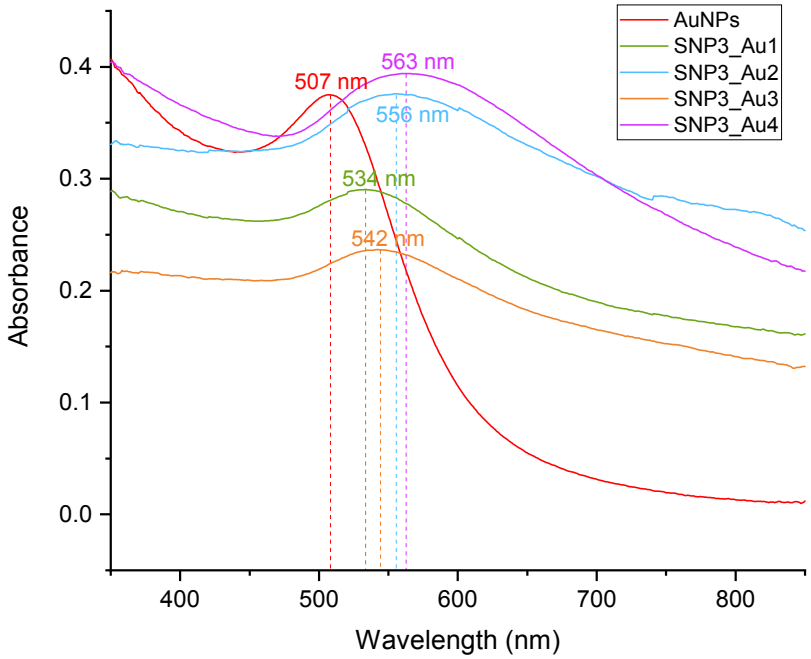

Figure 37: Absorption spectra of core-shell silica-gold NPs.

TEM images of SNP3_Au3 and SNP3_Au4 in figure 38 reveal that AuNPs have grown in comparison to gold seeded SNPs (SNP3_Au1 and SNP3_Au2, respectively), however they did not create a uniform nanoshell, which can be justified by a low concentration of $HAuCl_4$ in solution during growth. From figure 38B, it is clear that some of the AuNPs seeded to the SNP surface have coalesced, originating larger particles and decreasing the number of particles adsorbed at the SNP surface. To achieve a more complete and uniform gold nanoshell, it would have been necessary to increase the surface coverage of APTES per nm^2 of SNPs.

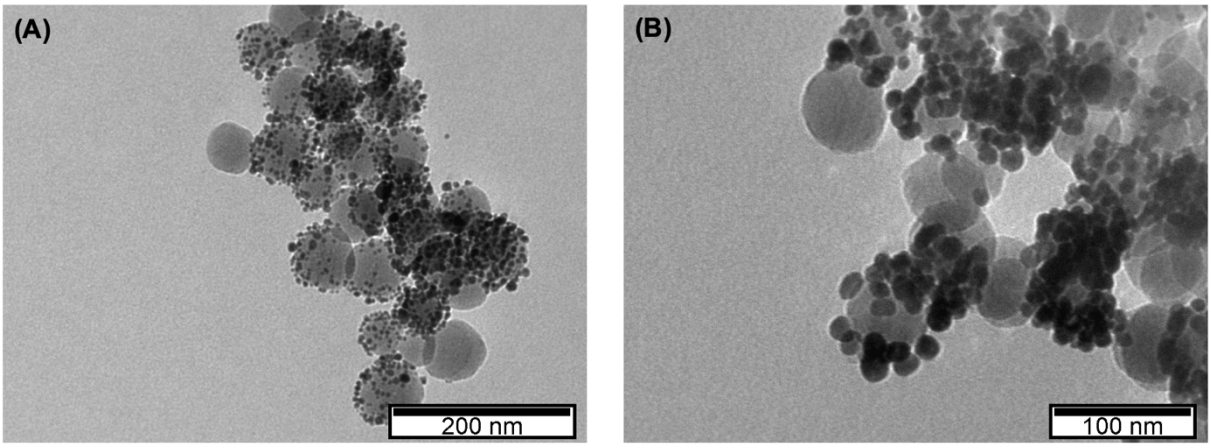

Figure 38: TEM images of (A) SNP3_Au3 and (B) SNP3_Au4. (scale bar: (A) 200 nm and (B) 100 nm)

The reducing agents used to grow an isotropic gold nanoshell and the absorbance peaks obtained by UV/Vis Spectroscopy are presented in table 10.

Table 10: Reducing agents used to grow the gold nanoshell and absorbance peaks (nm) obtained.

Sample	Reducing Agent	Absorbance Peak (nm)
SNP3_Au3	Ascorbic acid	542
SNP3_Au4	Ascorbic acid	563

Half gold seeded SNPs with low surface coverage of APTES (jSNP1_Au2, jSNP1_Au3 and jSNP4_Au2) exhibited a poor growth of the gold nanoshell via reduction with formaldehyde. The low surface coverage resulted in a reduced number of AuNPs adsorbed at the surface, which were not sufficient to act as nucleation sites for reduction of gold and creation of a half nanoshell (figure 39). After a first growth on jSNP1_Au2 and jSNP4_Au2, the absorbance peaks (figure 40 and table 11) were at around the same wavelength despite the fact that jSNP4_Au2 presented large APTES surface coverage (1.52 molecules/nm^2), which was expected to increase the AuNP seed deposition density in comparison to jSNP1_Au2. Due to these results, a second growth of jSNP1_Au3 was performed to evaluate the absorbance peak, which resulted in a red shift of 10 nm in comparison to the first growth, indicating that there was reduction of gold on the AuNPs seeded in the SNPs (figure 40).

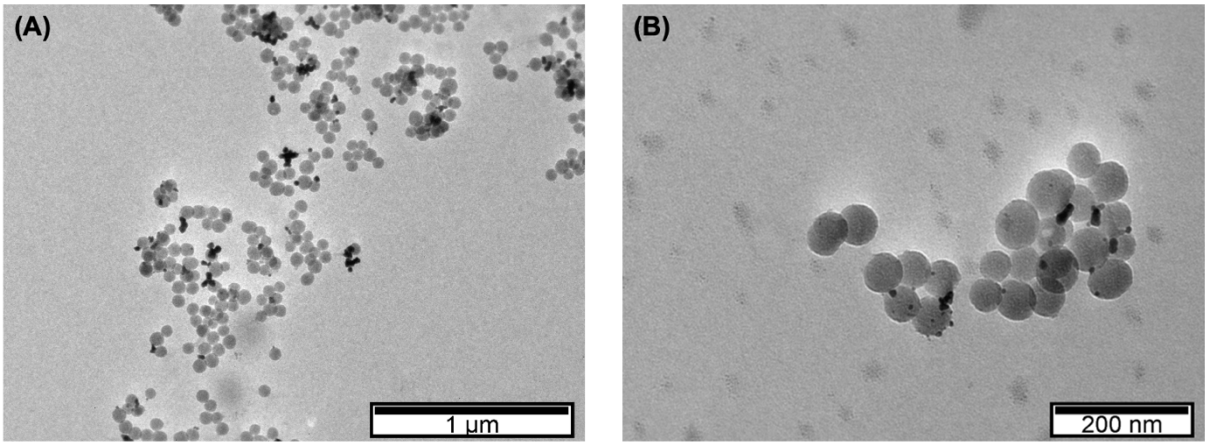

Figure 39: TEM images of (A) jSNP1_Au3 and (B) jSNP4_Au2. (scale bar: (A) 1 µm and (B) 200 nm)

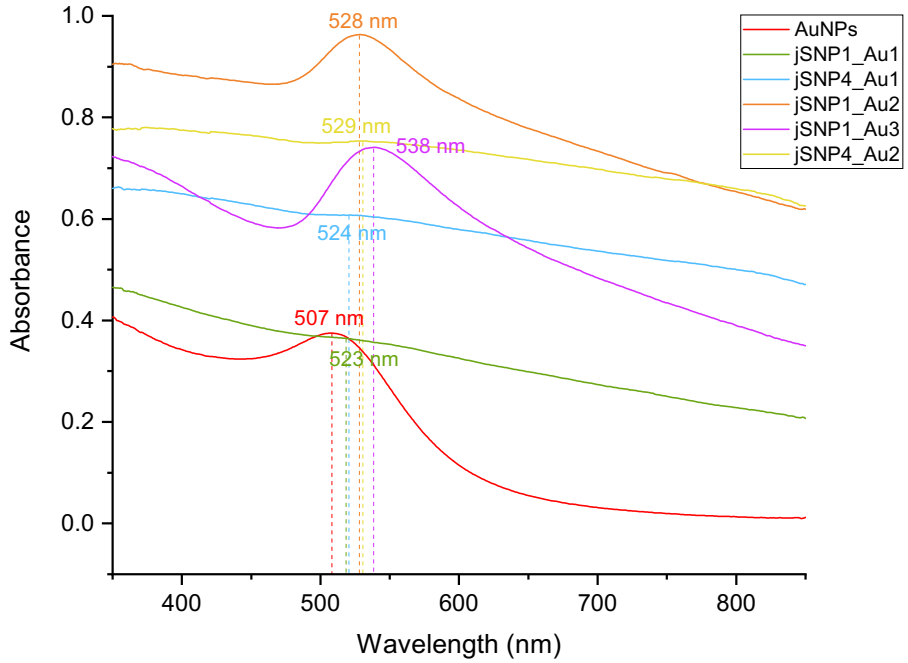

Figure 40: Absorption spectra of core-shell silica-gold NPs.

Half gold seeded SNPs with the highest surface coverage of APTES (15.81 molecules/nm^2) exhibited different behaviors upon the growth of the nanoshell by reduction with different reducing agents, which can be verified by the position of the absorption peaks (figure 41).

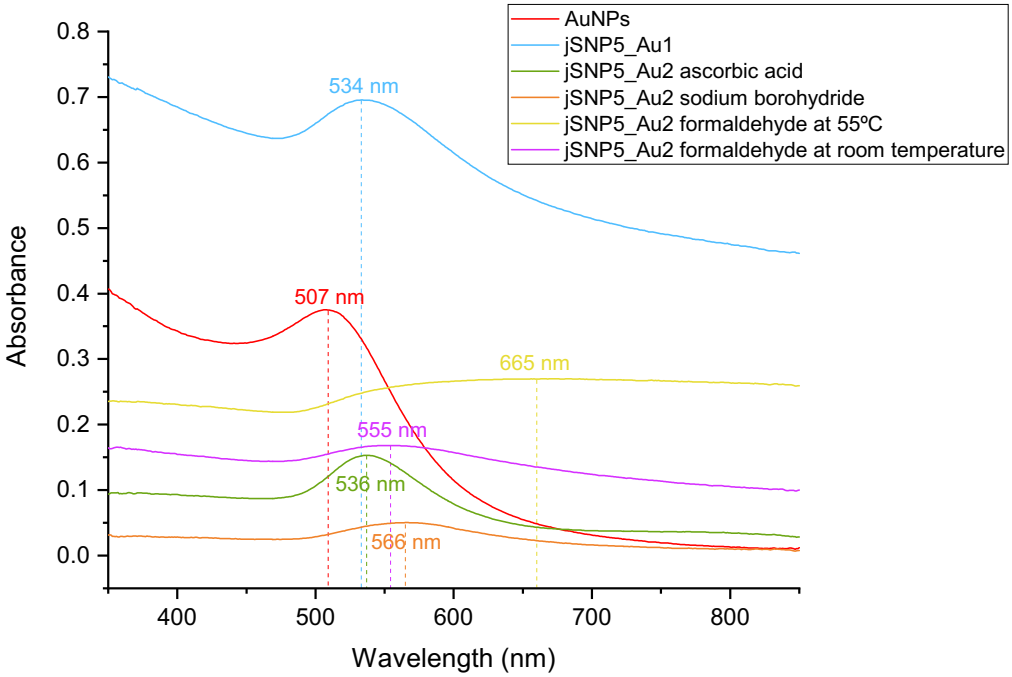

Figure 41: Absorption spectra of half gold nanoshell SNPs, in which the nanoshell was grown using different reduction mechanisms.

The reduction of $HAuCl_4$ with ascorbic acid caused a 2 nm red-shift of the absorbance peak. However, from figure 42, it is visible that larger AuNPs were formed during this process. And it is safe to assume that those are not SNPs with a gold nanoshell, because of the reduced red-shift, confirming that no gold nanoshell was formed.

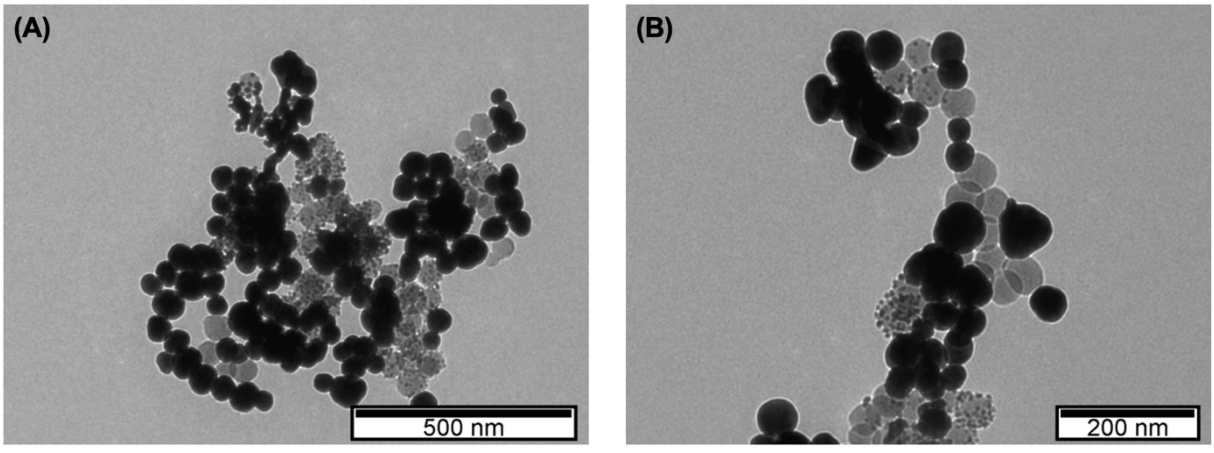

Figure 42: TEM images of jSNP5_Au2 grown by reduction of chloroauric acid with ascorbic acid. (scale bar: (A) 500 nm and (B) 200 nm)

Regarding the formation of a half gold nanoshell by reduction with $NaBH_4$, it is clear that the previously AuNPs seeded to the SNPs surface did act as nucleation sites for reduction of gold (figure 43). However,

a non-uniform nanoshell was created, which can be justified by the addition of excess of $NaBH_4$ solution. Perhaps, a more uniform half gold nanoshell could have been obtained by adding less $NaBH_4$ solution, and its growth could have been controlled upon each addition of the reducing solution. This growth resulted in a 32 nm red shift with respect to the half gold seeded SNPs, indicating that the seeded AuNPs have grown into larger particles and coalesced.

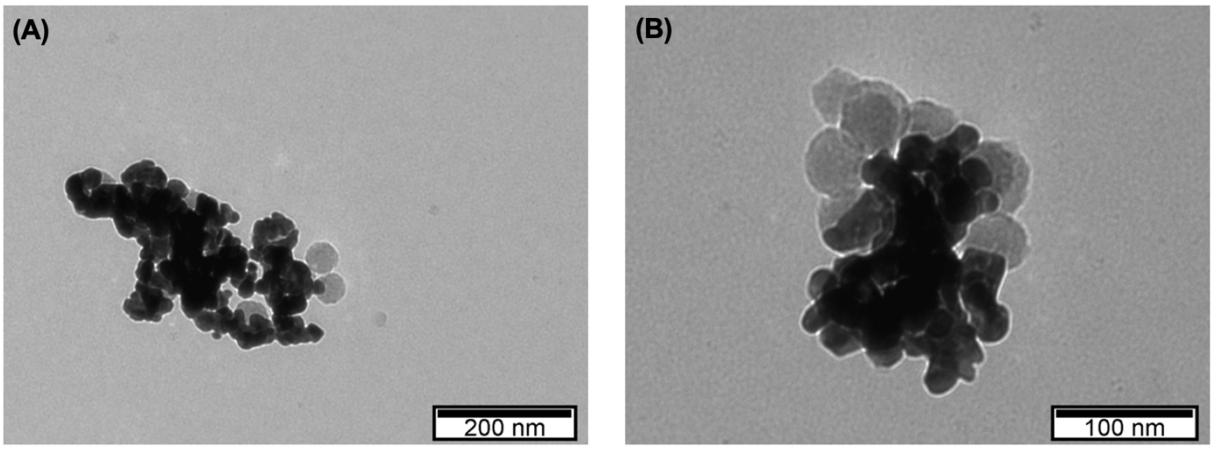

Figure 43: TEM images of jSNP5_Au2 grown by reduction of chloroauric acid with $NaBH_4$. (scale bar: (A) 200 nm and (B) 100 nm)

The growth of a half gold nanoshell was also accomplished by reduction with formaldehyde at 55°C and at room temperature. From figure 44, it is clear that the reduction that took place at 55°C originated a more uniform nanoshell, however it does not have a smooth appearance (figure 44A).

At 55°C, the growth of the half gold nanoshell was successfully accomplished (jSNP5_Au2). Figure 44A shows that an almost uniform nanoshell has grown and that the nanoshell was not created in some areas of the SNP surface. AuNPs seeded to the SNPs surface acted as nucleation sites for reduction of gold, and AuNPs have grown into larger particles, which has decreased the distance between them, leading to the plasmon coupling between neighboring AuNPs. This resulted in a 131 nm red-shift of the absorbance peak, indicating the formation of a nanoshell (figure 41).

At room temperature, the previously AuNPs seeded to the SNPs surface appear to have grown non-uniformly (figure 44B). The seeded AuNPs acted as nucleation sites, but it appears that nucleation only occurred in specific areas, and not in every AuNP seeded to the SNPs surface. Nevertheless, a 21 nm red-shift was verified, indicating that, for jSNP5_Au2, AuNPs have grown but a half gold nanoshell was not created.

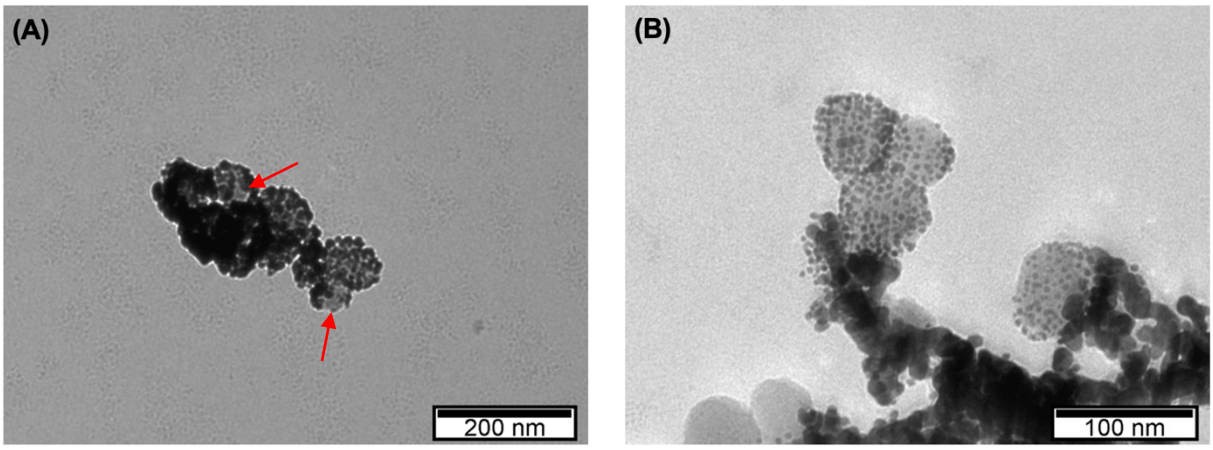

Figure 44: TEM images of jSNP5_Au2 grown by reduction of chloroauric acid with formaldehyde at 55°C (A) and at room temperature (B). Red arrows indicate areas not covered by gold. (scale bar: (A) 200 nm and (B) 100 nm)

With respect to the Janus NPs in which the half gold nanoshell was grown by reduction with formaldehyde at a temperature of 55°C, the thickness of the nanoshell formed was estimated by equation 7. R was determined by measuring the particle size using the software Image J. Therefore, after growing the half gold nanoshell via reduction with formaldehyde at 55°C, the thickness obtained was 9 nm, close to twice the size of the AuNPs synthesized.

The reducing agents used and the absorbance peaks obtained by UV/Vis Spectroscopy for Janus nanoparticles are presented in table 11.

Table 11: Reducing agents used to grow a half gold nanoshell and absorbance peaks (nm) obtained.

Sample	Reducing Agent	Absorbance Peak (nm)
jSNP1_Au2	Formaldehyde at room temperature	528
jSNP1_Au3	Formaldehyde at room temperature	538
jSNP4_Au2	Formaldehyde at room temperature	529
jSNP5_Au2	Ascorbic acid	536
	Formaldehyde at 55°C	665
	Formaldehyde at room temperature	555
	$NaBH_4$ at 50°C	566

From all the approaches used to attempt the growth of half gold nanoshell, the one using formaldehyde as a reducing agent at 55°C resulted in the growth of the more uniform nanoshell. The control over the shell thickness can be made by varying the amount of reducing agent used and the temperature during

growth. The addition of 25 µl of a formaldehyde solution at 55°C allowed the formation of a nanoshell, while the addition of 40 µl of a formaldehyde solution at room temperature only contributed to growth of AuNPs into larger particles. Therefore, from the experiments, it is clear that temperature affects the growth of the gold nanoshell, more than increasing the amount of reducing agent used, in this case formaldehyde.

The preferrable approaches to reduce chloroauric acid would be either using ascorbic acid or $NaBH_4$ as reducing agents, because of the toxicity issues associated with formaldehyde.

3.7 Motion Studies

The motion of the system developed was studied by means of Dynamic Light Scattering (DLS). The DLS measurements were performed at 25°C, using the backscatter mode ($\theta = 173°$), because high angle measurements are more sensitive to the motion of moving colloids and any changes in their diffusive behavior.[85] As previously mentioned, the particle mobility is determined by correlating the intensity fluctuations of the scattered radiation at a constant angle. Knowing that the particle concentration affects results in DLS, McGlasson et al. did an optimization of the particle concentration for which D_{eff} and τ_R would not vary within the concentration range of 0.01-0.30 wt%.[85]

DLS measurements of SNPs, jSNP5_Au1 and jSNP5_Au2 (gold nanoshell grown with formaldehyde at 55°C) were executed, and the autocorrelation curves of jSNP5_Au1 and jSNP5_Au2 are represented in figure 45. Isotropic particles are known for presenting a single decay event in the autocorrelation function while anisotropic particles exhibit two distinct decay events. From the results obtained, jSNP5_Au2 behave as isotropic particles, which is justified by an excessive growth of the nanoshell, that resulted in a decrease of the SNPs surface area not covered with AuNPs. However, jSNP5_Au1 behave as anisotropic particles. Hence, a more detailed analysis about the motion of jSNP5_Au1 is performed.

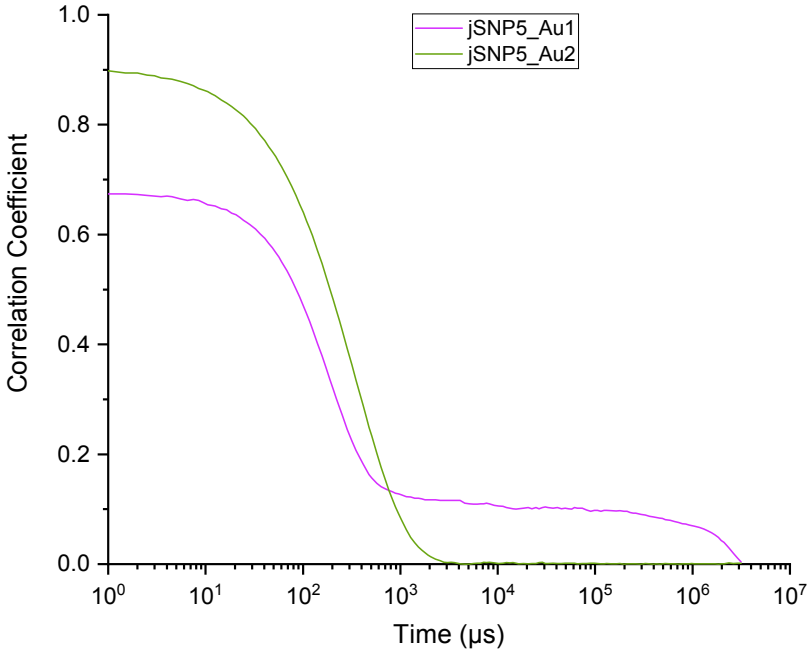

Figure 45: Autocorrelation function of jSNP5_Au1 and jSNP5_Au2.

For anisotropic particles, as jSNP5_Au1, the rotational and translational diffusion is decoupled as two distinct decay events in the autocorrelation function, given by equation 8.

$$g^{(1)}(\tau) = Ae^{-\Gamma_D \tau} + Be^{-\Gamma_R \tau} \tag{8}$$

Before proceeding with further determination of the autocorrelation function, it is important to calculate the theoretical values of the scattering vector (q), Stokes-Einstein diffusion coefficient (D_0) and a coefficient for rotational diffusion (γ_R), given by equations 13, 14 and 15, respectively. Where n is the refractive index of water, λ is the wavelength of the laser, θ is the angle at which the measurement is done, k_b is the Boltzmann's constant, T is the temperature, R is the radius of the particle and η is the dynamic viscosity of water. For jSNP5_Au1, R is determined by adding the radius of a SNP and the diameter of the AuNP.

$$q = \frac{4\pi n}{\lambda} sin\left(\frac{\theta}{2}\right) \tag{13}$$

$$D_0 = \frac{k_b T}{8\pi\eta R} \tag{14}$$

$$\gamma_R = \frac{k_b T}{8\pi\eta R^3} \tag{15}$$

A fitting of equation 8 using the difference of squares method and the Solver feature of Excel was done. The autocorrelation function that describes the behavior of jSNP5_Au1 was determined as:

$$g^{(1)}(\tau) = 0.59e^{-(5.65\times10^{-3})\tau} + 0.11e^{-(4.20\times10^{-7})\tau} \quad (16)$$

From equation 16, 17 and 18, the values for D_{eff} and τ_R are 8.13 μm²/s and 0.40 s, respectively.

$$\Gamma_D = q^2 D_{eff} \quad (17)$$

$$\Gamma_R = \frac{1}{6\tau_R} \quad (18)$$

At short decay times, the first decay in the autocorrelation function of jSNP5_Au1 corresponds to the translational diffusion of the particles (figure 46). While the long decay times are limited to rotational diffusion. To confirm that these decays correspond to the translational and rotational regimes, the mean-squared displacement of the particles was determined. The autocorrelation function is related to the mean-squared displacement by equation 9, which can be rearranged to obtain a plot of ΔL^2 versus decay time (figure 46).

$$g^{(1)}(\tau) = Ae^{-\frac{q^2}{6}(\Delta L^2)} \quad (9)$$

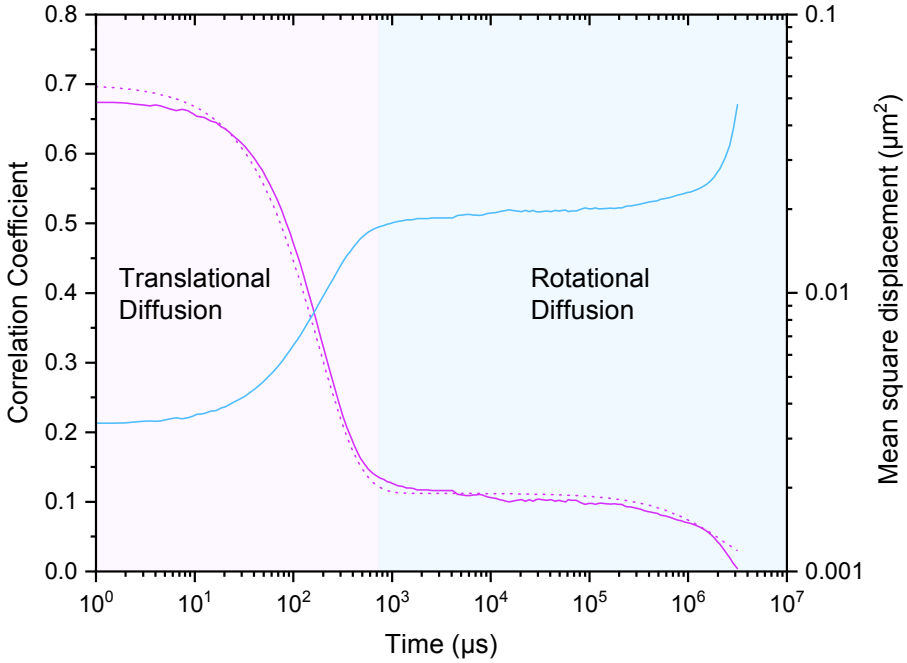

Figure 46: Autocorrelation function (purple line) and mean square displacement (blue line) versus decay time of jSNP5_Au1. Purple dots represent the fitting done for the autocorrelation function. Purple area of the plot corresponds to the translational diffusion regime that occurs at short decay times. Blue area of the plot corresponds to the rotational diffusion regime that occurs at long decay times and is characteristic of anisotropic particles.

At short decay times, ΔL^2 is characterized by a power-law slope, which is characteristic for translational diffusion, while at long decay times, ΔL^2 is constant, which describes the rotational diffusion regime.

A comparison between D_{eff} and D_0 indicates if the particles are indeed being accelerated by irradiation with the 632.8 nm laser. The calculated D_0 is 6.58 μm^2/s and D_{eff} is 8.13 μm^2/s from equation 17, which corresponds to an average 24% increase of the diffusion coefficient. Thus, jSNP5_Au1 are accelerating, even though they are not being excited at their SPR wavelength. The Zetasizer Nano ZS is equipped with a laser of 632.8 nm, while the SPR is around 534 nm. Lastly, the jSNP5_Au1 were moving with an average directional speed of 3.95 μm/s (equations 10 and 20).

$$D_{eff} = D_0 + \frac{v^2 \tau_R}{4} \tag{13}$$

$$v = \sqrt{\frac{\tau_R}{4}\left(D_{eff} - D_0\right)} \tag{20}$$

The average speed for the directional motion is dependent on the rotation relaxation time (τ_R) and on the difference between the apparent translation diffusion coefficient under irradiation (D_{eff}) and the

translation diffusion coefficient correspondent to Brownian motion (D_0). The jSNP5_Au1 developed directional motion upon light irradiation.

The 24% increase of the diffusion coefficient might be due to the gold nanoshell dispersity. From figure 35A, the non-uniformity of the nanoshell is clear. Therefore, the creation of a more uniform gold nanoshell would be expected to lead to a greater increase of the diffusion coefficient.

From these experiments, it is possible to conclude that the presence of a uniform and complete half gold nanoshell is not a requirement to make the particles accelerate. As long as AuNPs are seeded to the SNPs surface with a reduced interparticle distance, they are capable of converting the absorbed laser energy into heat. The resulting temperature gradient was enough to induce directional motion of the particles. If a higher seed deposition density had been obtained for jSNP5_Au1, an intensified temperature gradient would be expected, inducing a higher thermophoretic force to propel the particle, which would result in particles moving with higher speeds.

4 Conclusions

The goal of this work was to prepare Janus nanoparticles, composed by a SNP core and a gold nanostructure in half of their surface. Irradiation of the gold nanoshell generates a thermophoretic force, propelling the Janus nanoparticle in the opposite direction of the gold nanoshell.

The Janus nanoparticles were prepared by a Pickering emulsion route, and the exposed surface of the SNPs was modified with APTES, ensuring that there were enough NH_2 groups to link to AuNPs. Once AuNPs were seeded to the SNP surface, the growth of a gold nanoshell was tested by reducing chloroauric acid with different reducing agents (ascorbic acid, formaldehyde and $NaBH_4$). TEM and DLS analysis confirmed the formation of a nanoshell and the occurrence of two diffusion regimes upon irradiation: translational and rotational diffusion.

The surface coverage of APTES per nm^2 of SNP surface is a crucial parameter since it determines the seed deposition density. Higher surface coverages translate into a high seed deposition density. A surface coverage of 15 APTES molecules/nm^2 was reached and TEM images revealed the deposition of AuNPs in half of the surface of the SNP. A uniform gold nanoshell was accomplished by reduction of chloroauric acid with formaldehyde at 55°C. These Janus nanoparticles were then analyzed by UV/Vis spectroscopy, and exhibited a strong plasmon optical resonance which was red shifted to a longer wavelength (665 nm) than the corresponding wavelength (507 nm) of AuNPs.

Motion studies of the Janus nanoparticles were performed by DLS. The Janus nanoparticles exhibited a translational diffusion regime at short decay times and a rotational diffusion regime at long decay times. Upon irradiation with a 632.8 nm laser, a 24% increase of the translational diffusion coefficient was verified, indicating that Janus nanoparticles showed propulsion by light irradiation, with an average directional velocity of 3.95 μm/s.

In conclusion, the goal of this work was successfully achieved. The novelty comes from the preparation of a nanosystem with self-propulsion capabilities powered by light. Previous reports have described the synthesis of nanomotors powered by the catalytic decomposition of hydrogen peroxide fuel. However, motors which self-propulsion mechanism is based on the thermophoretic effect are normally designed at the microscale.[12] Our system is very promising since it provides a novel nanoscale fuel-free propulsion method, that can be employed for drug delivery applications.

5 Future Work

Having a successful proof-of-concept that our novel Janus nanoparticles move based on the thermophoretic effect, it should be of great interest to tune and improve our nanomotors by trying to achieve a controllable and uniform growth of a half gold nanoshell by reduction of chloroauric acid with a non-toxic reducing agent, such as ascorbic acid or $NaBH_4$, avoiding the problem of toxic agents for possible *in vivo* applications. Studies on how to control the nanoshell thickness would be important, since it would allow the tune of the plasmon resonance of the half gold nanoshell over a wide range of the electromagnetic spectrum, which can open a wider range of applications.

It would have been essential to have available SEM to tune the Pickering emulsion (unavailable during the whole duration of this work), and TEM to optimize the half gold nanoshell (only available in the last month of this work).

In further studies, it would be interesting to test how to use these systems in cells, for example as markers or as a drug delivery system. To use as markers, it would be interesting to incorporate a fluorescent dye into the silica nanoparticle. While to work as nanocarriers for drug delivery systems, it would be necessary to add a component that would hold and release the drug in a controllable way. This could be achieved by adding polymers to the free half surface of the silica nanoparticle or by creating a Janus nanoparticle which core was composed by a mesoporous silica nanoparticle, where the drug could be entrapped in the pores. Also, targeting capabilities could be added by the introduction of folic acid in the silica surface. Once the system is adsorbed to the cellular membrane, the propulsion provided by the thermophoretic effect would force the particles into the cell with high efficiency.

References

(1) Salamanca-Buentello, F.; Persad, D. L.; Court, E. B.; Martin, D. K.; Daar, A. S.; Singer, P. A. Nanotechnology and the Developing World. *PLoS Med* **2005**, *2* (5), 383–386. https://doi.org/10.1371/journal.pmed.0020097.

(2) Casagrande, C.; Fabre, P.; Raphael, E.; Veyssie, M. Janus Beads: Realization and Behaviour at Water/Oil Interfaces. *Europhys Lett* **1989**, *9* (3), 251–255. https://doi.org/10.1209/0295-5075/9/3/011.

(3) de Gennes, P.-G. Soft Matter. *Rev Mod Phys* **1992**, *64*, 645–648. https://doi.org/10.1103/RevModPhys.64.645.

(4) Pawar, A. B.; Kretzschmar, I. Fabrication, Assembly, and Application of Patchy Particles. *Macromol Rapid Commun* **2010**, *31* (2), 150–168. https://doi.org/10.1002/marc.200900614.

(5) Walther, A.; Müller, A. H. E. Janus Particles: Synthesis, Self-Assembly, Physical Properties, and Applications. *Chem Rev* **2013**, *113* (7), 5194–5261. https://doi.org/10.1021/cr300089t.

(6) Xu, C.; Xie, J.; Ho, D.; Wang, C.; Kohler, N.; Walsh, E. G.; Morgan, J. R.; Chin, Y. E.; Sun, S. Au-Fe3O4 Dumbbell Nanoparticles as Dual-Functional. *Angewandte Chemie* **2008**, *47* (1), 173–176. https://doi.org/10.1002/anie.200704392.

(7) Su, H.; Hurd Price, C. A.; Jing, L.; Tian, Q.; Liu, J.; Qian, K. Janus Particles: Design, Preparation, and Biomedical Applications. *Mater Today Bio* **2019**, *4*. https://doi.org/10.1016/j.mtbio.2019.100033.

(8) Zhang, X.; Fu, Q.; Duan, H.; Song, J.; Yang, H. Janus Nanoparticles: From Fabrication to (Bio)Applications. *ACS Nano* **2021**, *15* (4), 6147–6191. https://doi.org/10.1021/acsnano.1c01146.

(9) Han, B.; Xia, W.; Liu, K.; Tian, F.; Chen, Y.; Wang, X.; Liang, F.; Yang, Z. Janus Nanoparticles for Improved Dentin Bonding. *ACS Appl Mater Interfaces* **2018**, *10* (10), 8519–8526. https://doi.org/10.1021/acsami.7b19652.

(10) Zhou, X.; Huang, X.; Wang, B.; Tan, L.; Zhang, Y.; Jiao, Y. Light/Gas Cascade-Propelled Janus Micromotors That Actively Overcome Sequential and Multi-Staged Biological Barriers for Precise Drug Delivery. *Chemical Engineering Journal* **2021**, *408*. https://doi.org/10.1016/j.cej.2020.127897.

(11) Li, X.; Zhou, L.; Wei, Y.; El-Toni, A. M.; Zhang, F.; Zhao, D. Anisotropic Growth-Induced Synthesis of Dual-Compartment Janus Mesoporous Silica Nanoparticles for Bimodal Triggered Drugs Delivery. *J Am Chem Soc* **2014**, *136* (42), 15086–15092. https://doi.org/10.1021/ja508733r.

(12) Xuan, M.; Wu, Z.; Shao, J.; Dai, L.; Si, T.; He, Q. Near Infrared Light-Powered Janus Mesoporous Silica Nanoparticle Motors. *J Am Chem Soc* **2016**, *138* (20), 6492–6497. https://doi.org/10.1021/jacs.6b00902.

(13) Qiang, X.; Steinhaus, A.; Chen, C.; Chakroun, R.; Gröschel, A. H. Template-Free Synthesis and Selective Filling of Janus Nanocups. *Angewandte Chemie* **2019**, *131* (21), 7196–7200. https://doi.org/10.1002/ange.201814014.

(14) Zhang, Y.; Kang, L.; Huang, H.; Deng, J. Optically Active Janus Particles Constructed by Chiral Helical Polymers through Emulsion Polymerization Combined with Solvent Evaporation-Induced Phase Separation. *ACS Appl Mater Interfaces* **2020**, *12* (5), 6319–6327. https://doi.org/10.1021/acsami.9b21222.

(15) Yu, X.; Sun, Y.; Liang, F.; Jiang, B.; Yang, Z. Triblock Janus Particles by Seeded Emulsion Polymerization. *Macromolecules* **2019**, *52* (1), 96–102. https://doi.org/10.1021/acs.macromol.8b02101.

(16) Han, S. W.; Choi, S. E.; Chang, D. H.; Lee, D.; Kim, B.; Yang, H.; Seo, M.; Kim, J. W. Colloidal Pixel-Based Micropatterning Using Uniform Janus Microparticles with Tunable Anisotropic Particle Geometry. *Adv Funct Mater* **2019**, *29* (6). https://doi.org/10.1002/adfm.201805392.

(17) Varandili, S. B.; Stoian, D.; Vavra, J.; Pankhurst, J.; Buonsanti, R. Ligand-Mediated Formation of Cu/Metal Oxide Hybrid Nanocrystals with Tunable Number of Interfaces. *Chem Sci* **2020**, *11* (48), 13094–13101. https://doi.org/10.1039/d0sc04739b.

(18) Maric, T.; Nasir, M. Z. M.; Webster, R. D.; Pumera, M. Tailoring Metal/TiO2 Interface to Influence Motion of Light-Activated Janus Micromotors. *Adv Funct Mater* **2020**. https://doi.org/10.1002/adfm.201908614.

(19) Chen, X.; Xu, J.; Sun, D.; Jiang, B.; Liang, F.; Yang, Z. Emulsion Interfacial Synthesis of Polymer/Inorganic Janus Particles. *Langmuir* **2019**, *35* (18), 6032–6038. https://doi.org/10.1021/acs.langmuir.9b00211.

(20) Wang, Y.; Shang, M.; Wang, Y.; Xu, Z. Droplet-Based Microfluidic Synthesis of (Au Nanorod@Ag)-Polyaniline Janus Nanoparticles and Their Application as a Surface-Enhanced Raman Scattering Nanosensor for Mercury Detection. *Analytical Methods* **2019**, *11* (31), 3966–3973. https://doi.org/10.1039/c9ay01213c.

(21) Gu, H.; Yang, Z.; Gao, J.; Chang, C. K.; Xu, B. Heterodimers of Nanoparticles: Formation at a Liquid-Liquid Interface and Particle-Specific Surface Modification by Functional Molecules. *J Am Chem Soc* **2005**, *127* (1), 34–35. https://doi.org/10.1021/ja045220h.

(22) Yu, H.; Chen, M.; Rice, P. M.; Wang, S. X.; White, R. L.; Sun, S. Dumbbell-like Bifunctional Au-Fe3O4 Nanoparticles. *Nano Lett* **2005**, *5* (2), 379–382. https://doi.org/10.1021/nl047955q.

(23) Zhang, H.; Yang, Z.; Ju, Y.; Chu, X.; Ding, Y.; Huang, X.; Zhu, K.; Tang, T.; Su, X.; Hou, Y. Galvanic Displacement Synthesis of Monodisperse Janus- and Satellite-Like Plasmonic-Magnetic Ag-Fe@Fe3O4 Heterostructures with Reduced Cytotoxicity. *Advanced Science* **2018**, *5* (8). https://doi.org/10.1002/advs.201800271.

(24) Hong, J. W.; Wi, D. H.; Lee, S. U.; Han, S. W. Metal-Semiconductor Heteronanocrystals with Desired Configurations for Plasmonic Photocatalysis. *J Am Chem Soc* **2016**, *138* (48), 15766–15773. https://doi.org/10.1021/jacs.6b10288.

(25) Lattuada, M.; Hatton, T. A. Synthesis, Properties and Applications of Janus Nanoparticles. *Nano Today* **2011**, *6* (3), 286–308. https://doi.org/10.1016/j.nantod.2011.04.008.

(26) Ma, X.; Hahn, K.; Sanchez, S. Catalytic Mesoporous Janus Nanomotors for Active Cargo Delivery. *J Am Chem Soc* **2015**, *137* (15), 4976–4979. https://doi.org/10.1021/jacs.5b02700.

(27) Pourrahimi, A. M.; Villa, K.; Manzanares Palenzuela, C. L.; Ying, Y.; Sofer, Z.; Pumera, M. Catalytic and Light-Driven ZnO/Pt Janus Nano/Micromotors: Switching of Motion Mechanism via Interface Roughness and Defect Tailoring at the Nanoscale. *Adv Funct Mater* **2019**, *29* (22). https://doi.org/10.1002/adfm.201808678.

(28) Tadros, T. F. Emulsion Formation, Stability, and Rheology. In *Emulsion Formation and Stability*; 2013; pp 1–76.

(29) Lopetinsky, R. J. G.; Masliyah, J. H.; Xu, Z. Solids-Stabilized Emulsions: A Review. In *Colloidal Particles at Liquid Interfaces*; 2006; pp 186–224.

(30) Meyers, D. Emulsions. In *Surfaces, Interfaces and Colloids*; John Wiley & Sons, 1999; pp 253–294.

(31) Gao, J.; Bu, X.; Zhou, S.; Wang, X.; Bilal, M.; Hassan, F. U.; Hassanzadeh, A.; Xie, G.; Chelgani, S. C. Pickering Emulsion Prepared by Nano-Silica Particles - A Comparative Study for Exploring the Effect of Various Mechanical Methods. *Ultrason Sonochem* **2022**, *83*. https://doi.org/10.1016/j.ultsonch.2022.105928.

(32) Gonzalez Ortiz, D.; Pochat-Bohatier, C.; Cambedouzou, J.; Bechelany, M.; Miele, P. Current Trends in Pickering Emulsions: Particle Morphology and Applications. *Engineering*. Elsevier Ltd April 1, 2020, pp 468–482. https://doi.org/10.1016/j.eng.2019.08.017.

(33) Perro, A.; Meunier, F.; Schmitt, V.; Ravaine, S. Production of Large Quantities of “Janus” Nanoparticles Using Wax-in-Water Emulsions. *Colloids Surf A Physicochem Eng Asp* **2009**, *332* (1), 57–62. https://doi.org/10.1016/j.colsurfa.2008.08.027.

(34) Xia, T.; Xue, C.; Wei, Z. Physicochemical Characteristics, Applications and Research Trends of Edible Pickering Emulsions. *Trends Food Sci Technol* **2021**, *107*, 1–15. https://doi.org/10.1016/j.tifs.2020.11.019.

(35) Giermanska-Kahn, J.; Laine, V.; Arditty, S.; Schmitt, V.; Leal-Calderon, F. Particle-Stabilized Emulsions Comprised of Solid Droplets. *Langmuir* **2005**, *21* (10), 4316–4323. https://doi.org/10.1021/la0501177.

(36) Sharifzadeh, E.; Salami-Kalajahi, M.; Hosseini, M. S.; Aghjeh, M. K. R. A Temperature-Controlled Method to Produce Janus Nanoparticles Using High Internal Interface Systems: Experimental and Theoretical Approaches. *Colloids Surf A Physicochem Eng Asp* **2016**, *506*, 56–62. https://doi.org/10.1016/j.colsurfa.2016.06.006.

(37) Yuan, K.; Pacheco, M.; Jurado-Sánchez, B.; Escarpa, A. Design and Control of the Micromotor Swarm Toward Smart Applications. *Advanced Intelligent Systems* **2021**, *3* (6), 2100002. https://doi.org/10.1002/aisy.202100002.

(38) Bailey, M. R.; Grillo, F.; Spencer, N. D.; Isa, L. Microswimmers from Toposelective Nanoparticle Attachment. *Adv Funct Mater* **2022**, *32* (7). https://doi.org/10.1002/adfm.202109175.

(39) You, M.; Chen, C.; Xu, L.; Mou, F.; Guan, J. Intelligent Micro/Nanomotors with Taxis. *Acc Chem Res* **2018**, *51* (12), 3006–3014. https://doi.org/10.1021/acs.accounts.8b00291.

(40) Wang, Z.; Tu, Y.; Chen, Y.; Peng, F. Emerging Micro/Nanomotor-Based Platforms for Biomedical Therapy. *Advanced Intelligent Systems* **2020**, *2* (5), 1900081. https://doi.org/10.1002/aisy.201900081.

(41) Zhang, Q.; Dong, R.; Chang, X.; Ren, B.; Tong, Z. Spiropyran-Decorated SiO2-Pt Janus Micromotor: Preparation and Light-Induced Dynamic Self-Assembly and Disassembly. *ACS Appl Mater Interfaces* **2015**, *7* (44), 24585–24591. https://doi.org/10.1021/acsami.5b06448.

(42) Guix, M.; Meyer, A. K.; Koch, B.; Schmidt, O. G. Carbonate-Based Janus Micromotors Moving in Ultra-Light Acidic Environment Generated by HeLa Cells in Situ. *Sci Rep* **2016**, *6*. https://doi.org/10.1038/srep21701.

(43) Liu, K.; Ou, J.; Wang, S.; Gao, J.; Liu, L.; Ye, Y.; Wilson, D. A.; Hu, Y.; Peng, F.; Tu, Y. Magnesium-Based Micromotors for Enhanced Active and Synergistic Hydrogen Chemotherapy. *Appl Mater Today* **2020**, *20*. https://doi.org/10.1016/j.apmt.2020.100694.

(44) Xu, T.; Xu, L. P.; Zhang, X. Ultrasound Propulsion of Micro-/Nanomotors. *Applied Materials Today*. Elsevier Ltd December 1, 2017, pp 493–503. https://doi.org/10.1016/j.apmt.2017.07.011.

(45) Xu, T.; Luo, Y.; Liu, C.; Liu, C.; Zhang, X.; Wang, S. Integrated Ultrasonic Aggregation-Induced Enrichment with Raman Enhancement for Ultrasensitive and Rapid Biosensing. *Anal Chem* **2020**, *92* (11), 7816–7821. https://doi.org/10.1021/acs.analchem.0c01011.

(46) Wang, W.; Castro, L. A.; Hoyos, M.; Mallouk, T. E. Autonomous Motion of Metallic Microrods Propelled by Ultrasound. *ACS Nano* **2012**, *6* (7), 6122–6132. https://doi.org/10.1021/nn301312z.

(47) Ahmed, S.; Gentekos, D. T.; Fink, C. A.; Mallouk, T. E. Self-Assembly of Nanorod Motors into Geometrically Regular Multimers and Their Propulsion by Ultrasound. *ACS Nano* **2014**, *8* (11), 11053–11060. https://doi.org/10.1021/nn5039614.

(48) Ge, L.; Cheng, J.; Sun, X.; Liu, J.; Wei, D.; Guo, R. Controlled Group Motion of Anisotropic Janus Droplets Prepared by One-Step Vortex Mixing. *ACS Appl Mater Interfaces* **2020**, *12* (12), 14588–14598. https://doi.org/10.1021/acsami.0c00368.

(49) Zhan, Z.; Wei, F.; Zheng, J.; Yang, W.; Luo, J.; Yao, L. Recent Advances of Light-Driven Micro/Nanomotors: Toward Powerful Thrust and Precise Control. *Nanotechnol Rev* **2018**, *7* (6), 555–581. https://doi.org/10.1515/ntrev-2018-0106.

(50) Wang, L.; Kaeppler, A.; Fischer, D.; Simmchen, J. Photocatalytic TiO2 Micromotors for Removal of Microplastics and Suspended Matter. *ACS Appl Mater Interfaces* **2019**, *11* (36), 32937–32944. https://doi.org/10.1021/acsami.9b06128.

(51) Zhou, D.; Li, Y. C.; Xu, P.; Ren, L.; Zhang, G.; Mallouk, T. E.; Li, L. Visible-Light Driven Si-Au Micromotors in Water and Organic Solvents. *Nanoscale* **2017**, *9* (32), 11434–11438. https://doi.org/10.1039/c7nr04161f.

(52) Zhou, D.; Li, Y. C.; Xu, P.; McCool, N. S.; Li, L.; Wang, W.; Mallouk, T. E. Visible-Light Controlled Catalytic Cu2O-Au Micromotors. *Nanoscale* **2017**, *9* (1), 75–78. https://doi.org/10.1039/c6nr08088j.

(53) Zhang, Q.; Dong, R.; Wu, Y.; Gao, W.; He, Z.; Ren, B. Light-Driven Au-WO3@C Janus Micromotors for Rapid Photodegradation of Dye Pollutants. *ACS Appl Mater Interfaces* **2017**, *9* (5), 4674–4683. https://doi.org/10.1021/acsami.6b12081.

(54) Eskandarloo, H.; Kierulf, A.; Abbaspourrad, A. Light-Harvesting Synthetic Nano- and Micromotors: A Review. *Nanoscale*. Royal Society of Chemistry September 14, 2017, pp 12218–12230. https://doi.org/10.1039/c7nr05166b.

(55) Li, Y.; Mou, F.; Chen, C.; You, M.; Yin, Y.; Xu, L.; Guan, J. Light-Controlled Bubble Propulsion of Amorphous TiO2-Au Janus Micromotors. *RSC Adv* **2016**, *6* (13), 10697–10703. https://doi.org/10.1039/c5ra26798f.

(56) Pasciak, A.; Marin, R.; Abiven, L.; Pilch-Wróbel, A.; Misiak, M.; Xu, W.; Prorok, K.; Bezkrovnyi, O.; Marciniak, L.; Chanéac, C.; Gazeau, F.; Bazzi, R.; Roux, S.; Viana, B.; Lehto, V. P.; Jaque, D.; Bednarkiewicz, A. Quantitative Comparison of the Light-to-Heat Conversion Efficiency in Nanomaterials Suitable for Photothermal Therapy. *ACS Appl Mater Interfaces* **2022**. https://doi.org/10.1021/acsami.2c08013.

(57) Wang, Z.; Cheng, P. Enhancements of Absorption and Photothermal Conversion of Solar Energy Enabled by Surface Plasmon Resonances in Nanoparticles and Metamaterials. *Int J Heat Mass Transf* **2019**, *140*, 453–482. https://doi.org/10.1016/j.ijheatmasstransfer.2019.05.085.

(58) Gonçalves, A. S. C.; Rodrigues, C. F.; Moreira, A. F.; Correia, I. J. Strategies to Improve the Photothermal Capacity of Gold-Based Nanomedicines. *Acta Biomater* **2020**, *116*, 105–137. https://doi.org/10.1016/j.actbio.2020.09.008.

(59) Chen, Y.; Chen, H.; Shi, J. In Vivo Bio-Safety Evaluations and Diagnostic/Therapeutic Applications of Chemically Designed Mesoporous Silica Nanoparticles. *Advanced Materials* **2013**, *25*, 3144–3176. https://doi.org/10.1002/adma.201205292.

(60) Ribeiro, T.; Baleizão, C.; Farinha, J. P. S. Synthesis and Characterization of Perylenediimide Labeled Core-Shell Hybrid Silica-Polymer Nanoparticles. *Journal of Physical Chemistry C* **2009**, *113* (42), 18082–18090. https://doi.org/10.1021/jp906748r.

(61) Santiago, A. M.; Ribeiro, T.; Rodrigues, A. S.; Ribeiro, B.; Frade, R. F. M.; Baleizão, C.; Farinha, J. P. S. Multifunctional Hybrid Silica Nanoparticles with a Fluorescent Core and Active Targeting Shell for Fluorescence Imaging Biodiagnostic Applications. *Eur J Inorg Chem* **2015**, *2015* (27), 4579–4587. https://doi.org/10.1002/ejic.201500580.

(62) Singh, L. P.; Bhattacharyya, S. K.; Kumar, R.; Mishra, G.; Sharma, U.; Singh, G.; Ahalawat, S. Sol-Gel Processing of Silica Nanoparticles and Their Applications. *Adv Colloid Interface Sci* **2014**, *214*, 17–37. https://doi.org/10.1016/j.cis.2014.10.007.

(63) Stöber, W.; Fink, A.; Ernst Bohn, D. Controlled Growth of Monodisperse Silica Spheres in the Micron Size Range. *J Colloid Interface Sci* **1968**, *26*, 62–69. https://doi.org/10.1016/0021-9797(68)90272-5.

(64) Ghimire, P. P.; Jaroniec, M. Renaissance of Stöber Method for Synthesis of Colloidal Particles: New Developments and Opportunities. *J Colloid Interface Sci* **2021**, *584*, 838–865. https://doi.org/10.1016/j.jcis.2020.10.014.

(65) Wang, Y. C.; Rhéaume, É.; Lesage, F.; Kakkar, A. Synthetic Methodologies to Gold Nanoshells: An Overview. *Molecules* **2018**, *23* (11). https://doi.org/10.3390/molecules23112851.

(66) Yeh, Y. C.; Creran, B.; Rotello, V. M. Gold Nanoparticles: Preparation, Properties, and Applications in Bionanotechnology. *Nanoscale* **2012**, *4* (6), 1871–1880. https://doi.org/10.1039/c1nr11188d.

(67) Narain, R. *Polymers and Nanomaterials for Gene Therapy*; Woodhead Publishing, 2016.

(68) Ielo, I.; Rando, G.; Giacobello, F.; Sfameni, S.; Castellano, A.; Galletta, M.; Drommi, D.; Rosace, G.; Plutino, M. R. Synthesis, Chemical-Physical Characterization, and Biomedical Applications of Functional Gold Nanoparticles: A Review. *Molecules* **2021**, *26* (19). https://doi.org/10.3390/molecules26195823.

(69) Turkevich, J.; Cooper Stevenson, P.; Hillier, J. A Study of the Nucleation and Growth Processes in the Synthesis of Colloidal Gold. *Discuss Faraday Soc* **1951**, 55–75. https://doi.org/10.1039/DF9511100055.

(70) Zhao, P.; Li, N.; Astruc, D. State of the Art in Gold Nanoparticle Synthesis. *Coord Chem Rev* **2013**, *257* (3–4), 638–665. https://doi.org/10.1016/j.ccr.2012.09.002.

(71) Frens, G. Controlled Nucleation for the Regulation of the Particle Size in Monodisperse Gold Suspensions. *Nature Physical Science* **1973**, *241*, 20–22.

(72) Kimling, J.; Maier, M.; Okenve, B.; Kotaidis, V.; Ballot, H.; Plech, A. Turkevich Method for Gold Nanoparticle Synthesis Revisited. *Journal of Physical Chemistry B* **2006**, *110* (32), 15700–15707. https://doi.org/10.1021/jp061667w.

(73) Brown, K. R.; Fox, A. P.; Natan, M. J. Morphology-Dependent Electrochemistry of Cytochrome c at Au Colloid-Modified SnO2 Electrodes. *J Am Chem Soc* **1996**, *118*, 1154. https://doi.org/10.1021/ja952951w.

(74) Brust, M.; Walker, M.; Bethell, D.; Schiffrin, D. J.; Whyman, R. Synthesis of Thiol-Derivatised Gold Nanoparticles in a Two-Phase Liquid-Liquid System. *J Chem Soc Chem Commun* **1994**, No. 7, 801–802. https://doi.org/10.1039/C39940000801.

(75) Kim, J. M.; Lee, C.; Lee, Y.; Lee, J.; Park, S. J.; Park, S.; Nam, J. M. Synthesis, Assembly, Optical Properties, and Sensing Applications of Plasmonic Gap Nanostructures. *Advanced Materials* **2021**, *33* (46). https://doi.org/10.1002/adma.202006966.

(76) *Gold Nanoparticles: Properties and Applications*. https://www.sigmaaldrich.com/PT/en/technical-documents/technical-article/materials-science-and-engineering/biosensors-and-imaging/gold-nanoparticles (accessed 2022-08-21).

(77) Lermusiaux, L.; Plissonneau, M.; Bertry, L.; Drisko, G. L.; Buissette, V.; le Mercier, T.; Duguet, E.; Tréguer-Delapierre, M. Seeded Growth of Ultrathin Gold Nanoshells Using Polymer Additives and Microwave Radiation. *Sci Rep* **2021**, *11* (1). https://doi.org/10.1038/s41598-021-97171-0.

(78) Lee, S. W.; Nguyen, T. T. T.; van The, V.; Park, S. E. Optical Properties and Surface Morphologies of Silica-Gold Nanoshells Depending on Buffer Solutions and Reducing Agents. *Electronic Materials Letters* **2021**, *17* (5), 444–450. https://doi.org/10.1007/s13391-021-00292-x.

(79) Gordel-Wójcik, M.; Piela, K.; Kołkowski, R. Monitoring the Gold Nanoshell Growth Mechanism: Stabilizing and Destabilizing Effects of PEG-SH Molecules. *Physical Chemistry Chemical Physics* **2022**, *24* (9), 5700–5709. https://doi.org/10.1039/d2cp00239f.

(80) Oldenburg, S. J.; Averitt, R. D.; Westcott, S. L.; Halas, N. J. *Nanoengineering of Optical Resonances*; 1998; Vol. 288.

(81) Qu, Y.; Porter, R.; Shan, F.; Carter, J. D.; Guo, T. Synthesis of Tubular Gold and Silver Nanoshells Using Silica Nanowire Core Templates. *Langmuir* **2006**, *22* (14), 6367–6374. https://doi.org/10.1021/la060359m.

(82) Kumar, C. S. S. R. (Challa S. S. R.). Gold Nanoshells in Biomedical Applications; Wiley-VCH, 2009; p 507.

(83) Jain, P. K.; El-Sayed, M. A. Universal Scaling of Plasmon Coupling in Metal Nanostructures: Extension from Particle Pairs to Nanoshells. *Nano Lett* **2007**, *7* (9), 2854–2858. https://doi.org/10.1021/nl071496m.

(84) Hassan, P. A.; Rana, S.; Verma, G. Making Sense of Brownian Motion: Colloid Characterization by Dynamic Light Scattering. *Langmuir* **2015**, *31* (1), 3–12. https://doi.org/10.1021/la501789z.

(85) McGlasson, A.; Bradley, L. C. Investigating Time-Dependent Active Motion of Janus Micromotors Using Dynamic Light Scattering. *Small* **2021**, *17* (52). https://doi.org/10.1002/smll.202104926.

(86) Crucho, C. I. C.; Baleizão, C.; Farinha, J. P. S. Functional Group Coverage and Conversion Quantification in Nanostructured Silica by 1H NMR. *Anal Chem* **2017**, *89* (1), 681–687. https://doi.org/10.1021/acs.analchem.6b03117.

(87) Cortie, M.; Ford, M. A Plasmon-Induced Current Loop in Gold Semi-Shells. *Nanotechnology* **2007**, *18* (23). https://doi.org/10.1088/0957-4484/18/23/235704.

(88) Jian Ye; Liesbet Lagae; Guido Maes; Gustaaf Borghs; Pol Van Dorpe. Symmetry Breaking Induced Optical Properties of Gold Open Shell Nanostructures. *Nano Lett* **2009**, *9* (12), 4049–4052. https://doi.org/10.1021/nl9022176.

Appendix

Appendix 1: ^{1}H NMR spectra

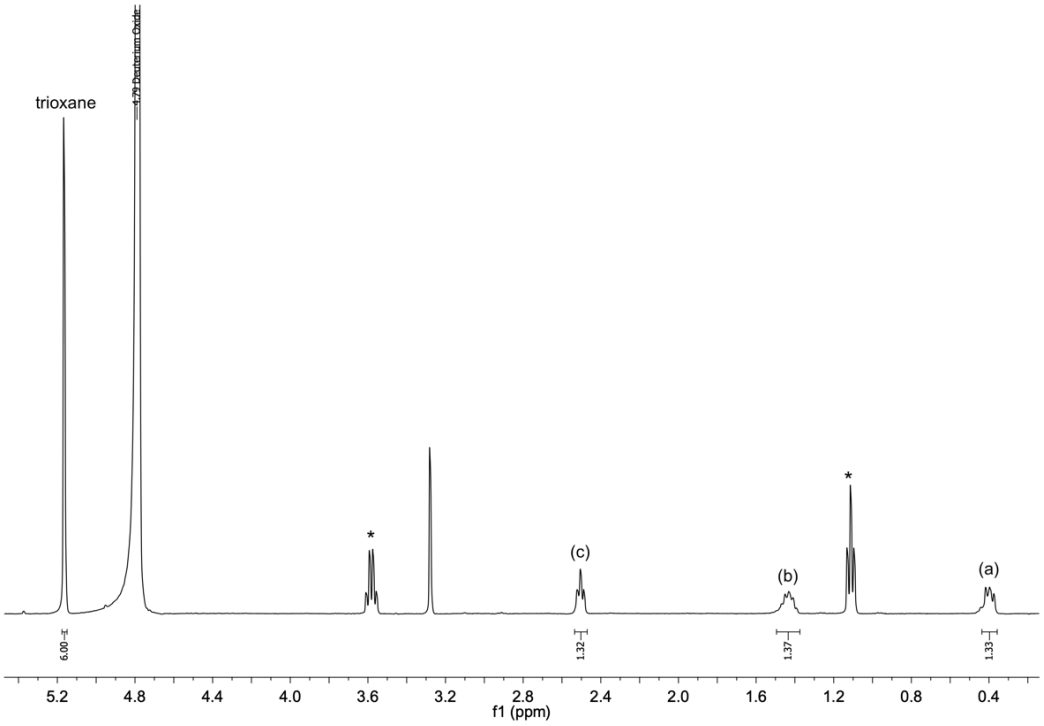

Figure 47: ^{1}H NMR spectrum of SNP6_f in D_2O: (a) corresponds to CH_3 protons of APTES and (b) and (c) correspond to CH_2 protons. Signed with * are the ethanol peaks and at 4.79 ppm is the D_2O peak. At 3.28 ppm is the methanol peak.

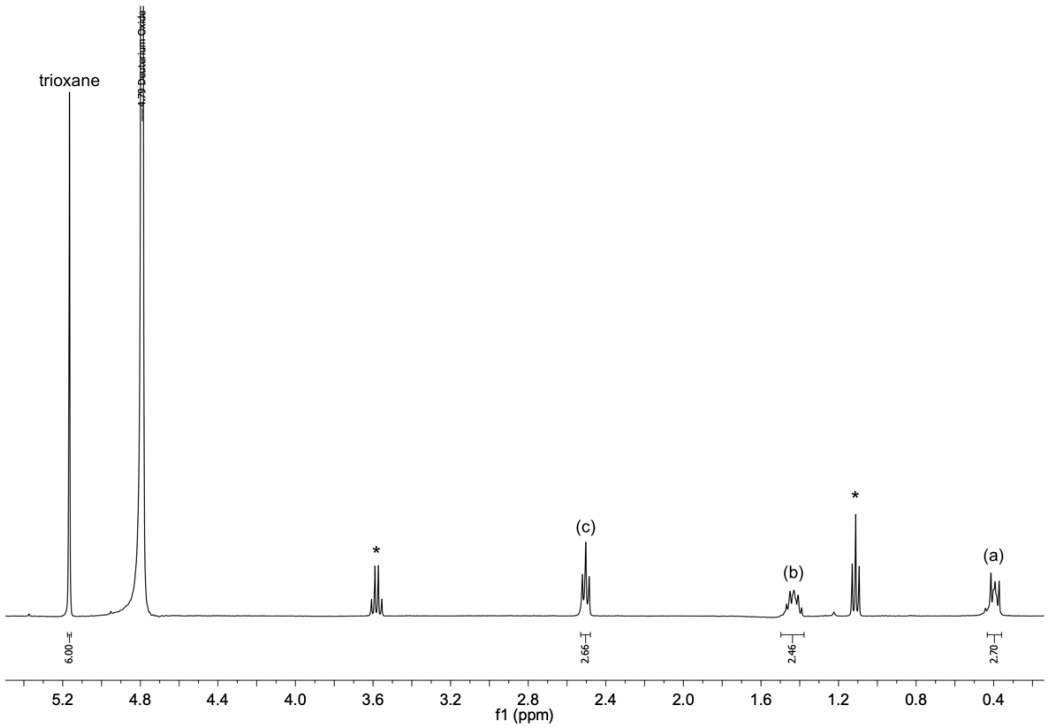

Figure 48: ^{1}H NMR spectrum of SNP3_f in D_2O: (a) corresponds to CH_3 protons of APTES and (b) and (c) correspond to CH_2 protons. Signed with * are the ethanol peaks and at 4.79 ppm is the D_2O peak.

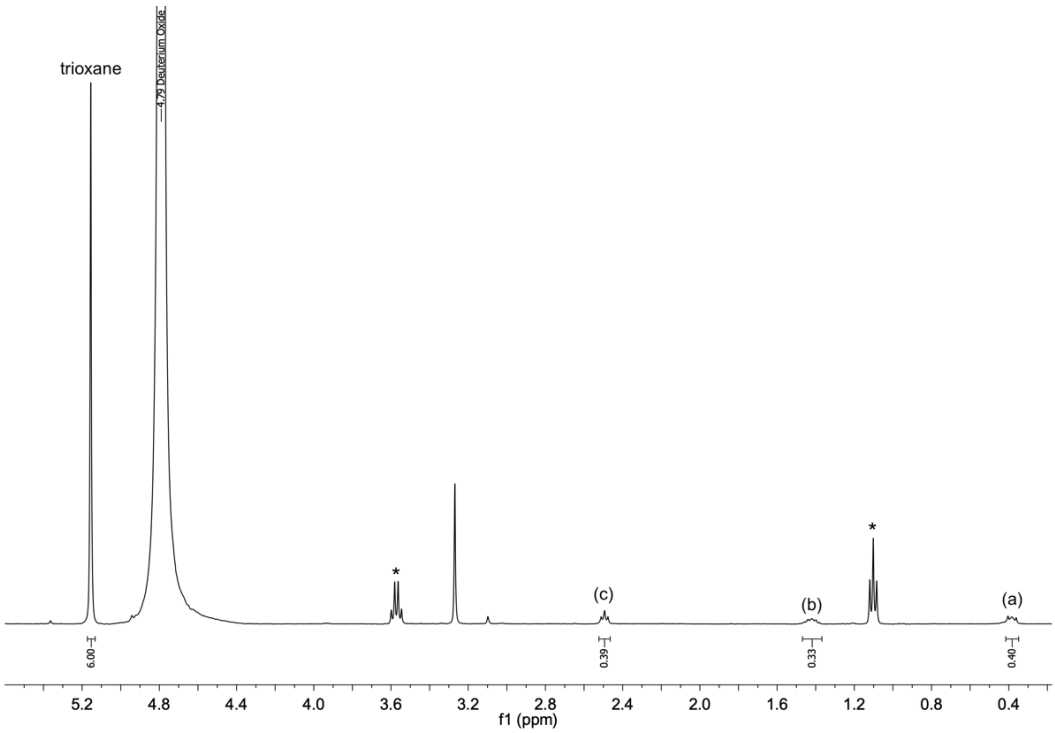

Figure 49: ^{1}H NMR spectrum of jSNP4_f in D_2O: (a) corresponds to CH_3 protons of APTES and (b) and (c) correspond to CH_2 protons. Signed with * are the ethanol peaks and at 4.79 ppm is the D_2O peak. At 3.28 ppm is the methanol peak.